INFORMATION TO USERS

This manuscript has been reproduced from the microfilm master. UMI films the text directly from the original or copy submitted. Thus, some thesis and dissertation copies are in typewriter face, while others may be from any type of computer printer.

The quality of this reproduction is dependent upon the quality of the copy submitted. Broken or indistinct print, colored or poor quality illustrations and photographs, print bleedthrough, substandard margins, and improper alignment can adversely affect reproduction.

In the unlikely event that the author did not send UMI a complete manuscript and there are missing pages, these will be noted. Also, if unauthorized copyright material had to be removed, a note will indicate the deletion.

Oversize materials (e.g., maps, drawings, charts) are reproduced by sectioning the original, beginning at the upper left-hand corner and continuing from left to right in equal sections with small overlaps.

ProQuest Information and Learning
300 North Zeeb Road, Ann Arbor, MI 48106-1346 USA
800-521-0600

Fundamentals of the Optical Design of Multiple Aperture Telescopes with Wide Fields of View

by
Erin Marie Elliott Sabatke

A Dissertation Submitted to the Faculty of the
Committee On Optical Sciences (Graduate)
In Partial Fulfillment of the Requirements
For the Degree of
Doctor of Philosophy
In the Graduate College
The University of Arizona

2002

ProQuest Information and Learning Company
300 North Zeeb Road
P.O. Box 1346
Ann Arbor, MI 48106-1346

THE UNIVERSITY OF ARIZONA ®
GRADUATE COLLEGE

As members of the Final Examination Committee, we certify that we have read the dissertation prepared by Erin Marie Sabatke

entitled Fundamental Principles of the Optical Design of Multiple Aperture Telescopes with Wide Fields of View

and recommend that it be accepted as fulfilling the dissertation requirement for the Degree of Doctor of Philosophy

James H. Burge	Dec. 4, 2002 Date
Jose M. Sasian	12/4/02 Date
Roland V. Shack	12/4/02 Date
	Date
	Date

Final approval and acceptance of this dissertation is contingent upon the candidate's submission of the final copy of the dissertation to the Graduate College.

I hereby certify that I have read this dissertation prepared under my direction and recommend that it be accepted as fulfilling the dissertation requirement.

Dissertation Director, James H. Burge — 12/17/02 Date

STATEMENT BY AUTHOR

This dissertation has been submitted in partial fulfillment of requirements for an advanced degree at The University of Arizona and is deposited in the University Library to be made available to borrowers under rules of the Library.

Brief quotations from this dissertation are allowable without special permission, provided that accurate acknowledgment of source is made. Requests for permission for extended quotation from or reproduction of this manuscript in whole or in part may be granted by the head of the major department or the Dean of the Graduate College when in his or her judgment the proposed use of the material is in the interests of scholarship. In all other instances, however, permission must be obtained from the author.

SIGNED: 

ACKNOWLEDGMENTS

This work was made possible by the support of the Michelson Fellowship Program, funded by NASA as an element of the Space Interferometry Mission. JPL is managed for NASA by the California Institute of Technology.

I would like to thank Alice Palmer at Lockheed-Martin for sharing the raytrace code, Optima, and for her invaluable support in learning to model multiple aperture systems with the program.

Thanks go to my dissertation committee, Professors Shack and Sasian, who provided valuable insights during the work and gave their time to review both the dissertation proposal and this dissertation.

I would also like to thank my advisor, Jim Burge, whose enthusiasm and intelligence combined to revive my research and my spirits more than once. I gained invaluable lessons because he was willing to share his time and experiences with me.

Finally, I would like to thank my family for their support. I would especially like to thank Stephen and Emily for always believing that my abilities were unlimited. Most importantly, I want to thank my husband, Derek, for the laughter, love, and encouragement that he has constantly provided.

TABLE OF CONTENTS

TABLE OF CONTENTS—*Continued*

TABLE OF CONTENTS—*Continued*

LIST OF FIGURES

LIST OF FIGURES—*Continued*

LIST OF FIGURES—*Continued*

LIST OF TABLES

ABSTRACT

Ground-based interferometric telescopes have demonstrated large gains in resolution and sensitivity over single-aperture telescopes. Similar gains are imminent in space telescopes. Two types of interferometers are currently in use: Michelson stellar interferometers and "Fizeau" interferometers. Fizeau, or wide-field interferometers, create a wide-field image of an object convolved with the PSF of the interferometer. This dissertation derives and demonstrates a new approach to the design of wide-field interferometric telescopes.

The first part of this dissertation is a tutorial on multiple aperture systems. Design basics such as PSF and OTF, fill factors, resolution, and temporal coherence are investigated. We show that the perfect image for a multiple aperture system is the sum of an image from each aperture and a set of fringes from each pair of apertures. For this image to remain perfect over a wide field of view, three things must happen: the images from each aperture must stay together as the field angle changes, the images must combine coherently, and the images from each aperture must be unaberrated. Coherence losses are caused by a constant phase offset (piston error) between two apertures in the system. Lateral image separations are caused by tilt errors, and longitudinal image separations are caused by power errors.

Any of the beam combining errors (piston, tilt, and defocus) can occur as any function of field angle. The constant and linear errors have straightforward geometric explanations. Constant piston errors occur when the axial pathlengths in each arm at zero field angle are not equal. Linear piston errors are caused by violating the Abbe sine condition, as applied to the axial rays of the system. Constant tilt errors are pointing errors in the telescope. Linear tilt errors occur when the focal lengths of each arm are not equal. Constant defocus errors occur when an individual image plane is offset from the system's image plane. And linear defocus errors occur when

an individual image plane is rotated with respect to the system's image plane.

Wavefront aberration theory for plane-symmetric systems is used to calculate RMS wavefront errors and explore how the system performance is affected by these errors.

Four example systems are designed by applying the derived design rules. The first system is a rotationally-symmetric Paul system that is then segmented to make a four-aperture system. The low-order design rules in this system are shown to be automatically satisfied.

The second system is an array of four afocal telescopes that share a three-mirror combining telescope. Fold flats are used in the inner two arms to satisfy the requirement that the axial pathlengths should match. Linear piston errors are eliminated by forcing the beam configuration into the combiner to be a scaled version of the afocal array. The angles of the fold flats are chosen to eliminate any constant tilt errors. Because the combining optics are shared, there are no constant defocus, linear defocus, or linear tilt errors in the system.

As a third example, the design of a beam combiner for the Large Binocular telescope is explored. By applying the design rules, coherent imaging with a 1 arcminute field of view is achieved with just three reflections. Linear defocus errors appear, but are minimized by bringing the beams to focus as closely together as possible. The sine condition is satisfied for the axial rays so that the linear piston errors are zero. The constant piston, tilt, and defocus errors are all zero, since the two arms in the system are mirror-images of one another, but this also introduces differential distortion into the system.

As a fourth example, a space telescope design is presented that utilizes a flat gossamer mirror technology. The system would consist of a primary array of flats, a shared secondary mirror, and a tertiary array with one mirror corresponding to each of the primary flats. Each branch of the system consists of a primary flat, the shared secondary, and a tertiary that brings the beam to the correct image point. The position of the tertiary is chosen to eliminate axial pathlength errors. The linear

piston errors are satisfied if the primary flats are all located on a spherical surface of radius L, equal to the total length of the telescope system. Constant defocus errors are eliminated by choosing the tertiary powers so that the focal planes to overlap. The focal lengths of each branch do not match, then, and the linear tilt errors that result dominate the system's performance. Small linear defocus errors are present because the individual focal planes are rotated with respect to the system's image plane.

The RMS wavefront error is calculated as a function of the system parameters. This gives an efficient method for exploring design space for the gossamer systems. The performance of a system of five flats is explored in this way. A few specific five-flat systems are modeled with full interferometric raytraces, and the results show good agreement with the Strehl values predicted by calculation of the RMS wavefront errors.

Chapter 1

INTRODUCTION

Interferometric telescopes are a new breed of telescopes that have already achieved huge gains in resolution and sensitivity over older telescopes. Traditionally, telescopes have used single primary mirrors for collecting images. Gains in resolution and sensitivity for such telescopes is tied to the ability to produce larger and larger primary mirrors. Interferometers, though, use two or more primary mirrors whose images are combined with optics that follow the primary mirrors. The resolution in such systems is limited only by how far apart the primary mirrors can be placed. The sensitivity is limited only by the number of mirrors that can be purchased and integrated into the system. These gains are achieved without further development of single-mirror fabrication techniques.

Figure 1.1 is a photograph of the IOTA interferometer, a three-aperture system with two of the telescopes on moving tracks.[1] Figure 1.2 is a drawing of the Large Binocular Telescope, which is a fixed-position, two-aperture interferometer.[2] These telescopes operate in the near-IR and visible regimes. Because the wavelengths are short, the beam-combining must be done optically, with series of mirrors and flats that bring the beams together in the image plane at exactly the same point in time. For interferometers in the longer radio wavelengths, the beam-combining can be done electronically.

Figure 1.1 and 1.2 show ground-based interferometers, but the next generation of telescopes in space must be multiple aperture systems, as well. For space-based systems, the size of a telescope's primary mirror is limited to about five meters by the size of current rocket shrouds. For space telescopes to get bigger, the primaries must be segmented, or smaller telescopes functioning as interferometers must be used.

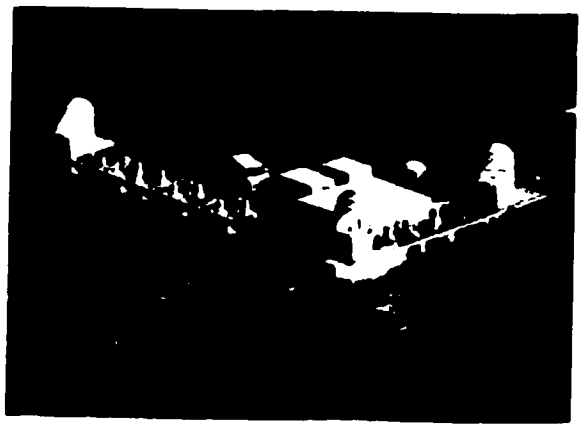

FIGURE 1.1. *The three-aperture IOTA interferometer. Two of the telescopes can move along the pairs of rails visible in the picture.*

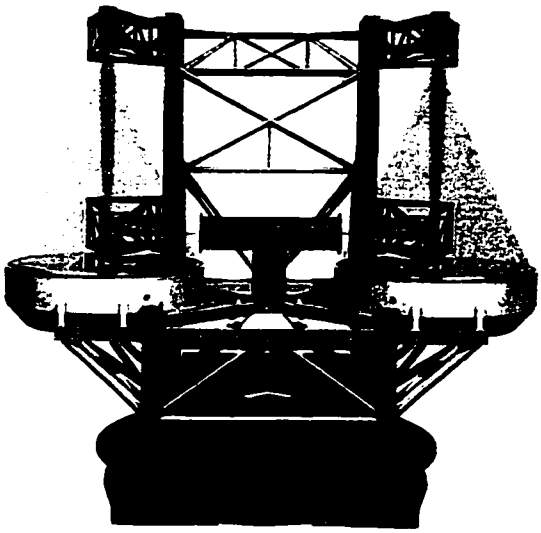

FIGURE 1.2. *A drawing of the Large Binocular Telescope interferometer, which is a two aperture system. The positions of the primaries are fixed.*

NASA has required that the infrared successor to the Hubble Space Telescope, the Webb Space Telescope, will be a segmented system. Missions further in the future will also require interferometry. The Terrestrial Planet Finder mission will need a baseline diameter of 100 meters as well as a large collecting area, which is not possible with current single-mirror telescopes.

1.1 Wide-field interferometry vs. the Michelson stellar interferometer

This dissertation deals with the design of wide-field interferometers, which should not be confused with the more common Michelson stellar interferometers. A wide-field interferometer in operation produces an extended image that is superimposed with fringes. The final image is the convolution of the system's PSF with the real object, provided the PSF is the same everywhere in the field. If the PSF is known, the real object may be recovered by de-convolving the image with the known PSF. (Since the PSF in real telescope changes as a function of field, this is actually not a simple deconvolution, but a more sophisticated reconstruction process.)[3] The first telescope to operate in this way on a regular basis will be the Large Binocular Telescope (LBT), currently under construction on Mt. Graham in Arizona and expecting first light in its interferometric mode in late 2003.[2] The LBT consists of two 8.4 meter primary mirrors. Its baseline is fixed, because the optics for combining the beams coherently would be prohibitively complicated for changing baselines. The high-resolution fringes only occur in one direction, perpendicular to the baseline of the system. To get full spatial information about the object, then, images at several angles in the sky must be gathered. A simulated image for the LBT is shown in Figure 1.3. Fringes are clearly visible in the image in the upper right. The reconstructed image shown on the lower left is comparable to that of a 30 meter single-primary telescope.

Most other current ground-based telescopes are Michelson Stellar Interferometers.

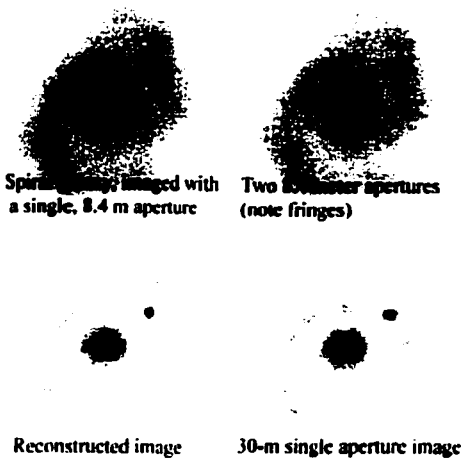

FIGURE 1.3. *The simulated LBT image of a spiral galaxy. Fringes are visible in the single exposure shown in the upper right. The final image is comparable in resolution to that of a 30 meter telescope. The image was created by Keith Hege.*

IOTA, CHARA, NPOI, KECK, and VLTI are some examples. The design of Michelson interferometers is not covered in this dissertation. These telescopes have very narrow fields of view. Looking at an unresolved object, they measure the fringe visibility at the center of the image as a function of a changing baseline. The result is a plot of fringe visibility versus baseline separation, which is related to the spatial coherence of the object. The intensity of the object is proportional to an inverse Fourier transform of the visibility.[4],[5] Some assumption about the object's basic shape is required for this technique to work, so there are difficulties with imaging very complex objects in this way.

The newest generation of optical and near-IR interferometers have 8 to 10 meter apertures. In older interferometers, just as with single-aperture telescopes, larger apertures were not useful because of atmospheric effects. The advent of adaptive optics has corrected this problem, allowing aperture sizes to increase dramatically. This effect is seen in Figure 1.4. The telescopes on the bottom right are generally Michelson interferometers with fairly small apertures, since they do not use adaptive

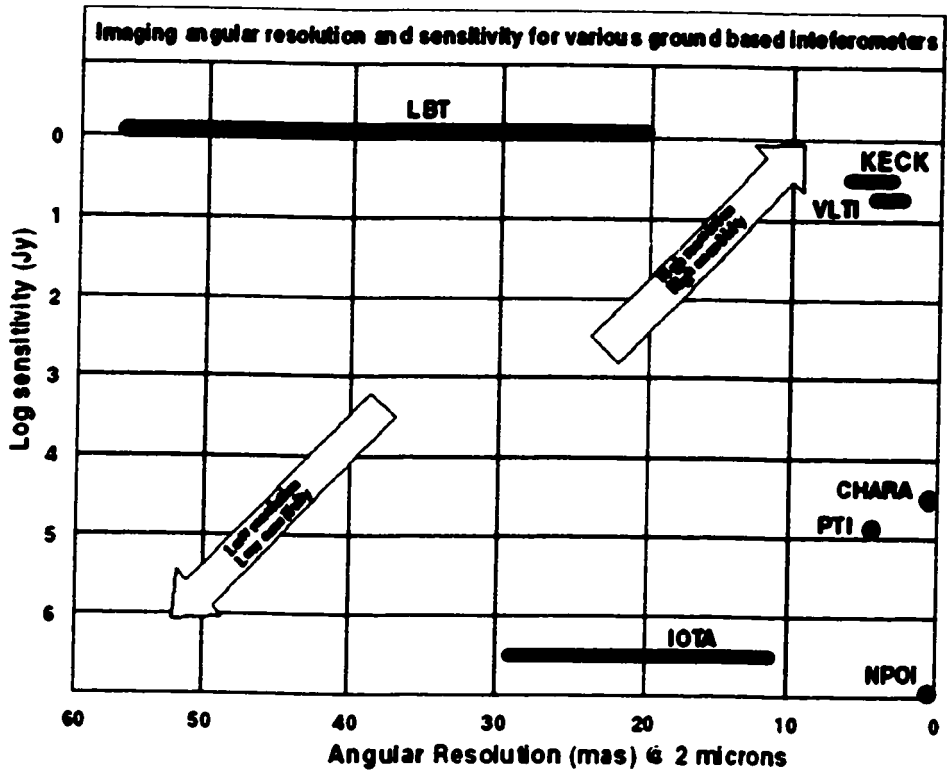

FIGURE 1.4. *A sensitivity versus resolution plot for current, ground-based interferometers. The newest interferometers have made large gains in sensitivity due to the advent of adaptive optics.*

optics. The newest interferometers (Keck, LBT, and VLTI) have between two and four apertures with diameters of 8 to 10 meters, giving high sensitivities. Single-mirror telescopes would appear in the middle left of the plot - they may have apertures of up to 8 meters, giving sensitivities as good as or better than the old Michelsons, but their resolution is very limited compared to any of the interferometers.

1.2 History of wide-field imaging

Wide field interferometric imaging has a fairly long history, though it took adaptive optics to bring it into the mainstream in the optical and near-IR regimes. Diffraction

modeling of multiple aperture systems' point spread functions and transfer functions began in the late 1960's.[6],[7] Some work was done to find the optimal positions for a given number of mirrors.[8],[9] Progress was made on aberrations analysis in multiple aperture systems.[10],[11],[12],[13] A small amount of work has been done on polarization issues in these systems.[14] Several interesting papers on general design issues were also published.[15],[16],[17],[18],[19],[20] Note that the papers cited here do not include papers that deal with the design and implementation of Michelson stellar interferometers.

Meinel was the first to recognize and propose a solution for correcting the linear piston errors in wide-field interferometric systems[21], while Traub contributed important proofs of the requirements.[22] Distortion problems have been investigated in specific systems.[23], [24]

The first telescope to succeed in wide-field imaging was the Multiple Mirror Telescope, located on Mt. Hopkins near Tucson, Arizona.[25] The combining was difficult to accomplish, since the six-mirror telescope had not originally been designed to operate in this mode. A series of fold flats was used to combine the beams, and prisms were used to correct for the linear piston errors in the system. The experiment set the stage for the next generation of wide-field imagers. Its technological successor, the Large Binocular Telescope, will be the first telescope that can operate full-time in the wide-field interferometric mode (see Figure 1.2).[2],[26]

1.3 Dissertation contents

This dissertation is a tutorial on wide-field multiple aperture system design. First, some terminology and basic measures of telescope performance are introduced. The perfect interferometric image is examined in detail. Next, the errors that can degrade the image are identified, and their effects on the system performance are demonstrated. Wavefront aberration theory is used to quantify the errors and predict the

system performance in the presence of the errors. The physical origins of the errors are then discussed, and correction methods become clear when the physical error sources are understood. Finally, several example designs are given that successfully implement the correction methods.

Going into more detail, Chapter 2 covers some basics of multiple aperture systems. The PSF consists of an image from each aperture in the system, and a set of fringes from each pair of apertures in the system. The PSF gets narrower with increasing baseline length, giving better resolution for longer separations of the individual telescopes. For wide-field imaging, side lobes in the PSF are not useful, since an extended object is the convolution of the system's PSF with the collection of point sources in the object. Side lobes in one point's image just act as background noise for the image of an adjacent object point. The number of fringes, and thus side-lobes, in the PSF is inversely proportional to the fill factor of the telescope, and a completely filled aperture will have no side-lobes of significant amplitude.

We show that the broad-band PSF loses visibility at points in the image plane such that the OPD between the apertures is on the order of the coherence length. The visibility envelope of the polychromatic fringes is related to the Fourier transform of the object's spectrum. If the fill factor is high, the diffraction envelope may drive the fringes to zero amplitude before the loss of fringe visibility is observed.

The transfer function of multiple aperture systems is examined. The OTF has a cutoff frequency related to the largest dimension in the entrance pupil of the system. The OTF has peaks related to each different baseline length in the system. The number of peaks will always be $(2n+1)$, where n is the number of different baselines in the system. Redundant baseline lengths increase the transmission at the associated frequency.

In Chapter 3, we establish that only four kinds of errors can affect the image of a multiple aperture system. These errors are: lateral separation of the images from each arm, longitudinal separation of the images from each arm, loss of coherence, and

aberrations that affect the quality of the image from each arm. The two-aperture PSF as a function of each of these errors is examined. We find that piston errors in the wavefront lead to coherence losses in the combined images. Tilt errors in an aperture cause lateral image separation, and a defocus error in an aperture causes longitudinal image separation. Aberrations in the individual apertures that cause degradation of that aperture's image will always cause the combined image to deteriorate, and putting equal amounts of such aberration into each arm of the system is not useful.

Chapter 4 discusses the physical origins of these errors. Each error can occur as any power of field angle. This chapter deals with constant and linear piston (coherence), tilt (lateral image separation), and defocus (longitudinal image separation) errors. Constant piston errors are caused by a mismatch in the axial pathlengths of the system. This effect can be eliminated by selecting the positions of the optics so that the axial pathlengths in all branches are equal. Linear piston errors are caused by the additional distance an axial ray in one arm of the system needs to travel in order to reach the image plane, when the field angle is nonzero so that the phase wavefront is tilted when it enters the system. These can be corrected by satisfying the Abbe sine condition for the axial rays of the system. Constant tilt errors are just "pointing" errors in the telescope arms. The individual optics can be tilted to correct this error. Linear tilt errors are caused by unequal focal lengths in the arms of the system. These can be corrected by adjusting the power in each arm of the system to be equal. Constant defocus errors are caused when the image from one arm comes to focus before or after the system image plane. The power of the branch can be adjusted to correct this. Finally, linear defocus errors appear when the image planes for each branch are tilted with respect to one another. Image plane tilts can be calculated using the Scheimpflug condition. Such image tilt does not occur in systems that share combining optics, but in a more general system, a single off-axis mirror will correct the image plane tilt for that branch of the system.

Each error can be quantified as a departure from the perfect wavefront, using

geometry to calculate the magnitude of the departure. This requires plane-symmetric aberration theory, since branches of multiple aperture systems generally only have one plane of symmetry, if any. The RMS wavefront error for any combination of these low-order errors can be calculated, and then the Strehl of the system can be predicted for small wavefront errors. This technique is useful, since modelling the entire system interferometrically can be time-consuming. The RMS wavefront error for a two-aperture system is calculated and discussed. There are two situations when the RMS wavefront error is not an accurate predictor of system performance. These are the cases of the sparse two-aperture system and the sparse three-aperture system that is not in a linear configuration. For these systems, the polychromatic PSF must be calculated directly in order to estimate system performance, or the piston errors must be known to be much less than a coherence length of the system.

Chapter 5 covers the origins of tilt errors that are quadratic and cubic as a function of field angle. Quadratic distortions appear only in plane-symmetric systems, and cannot occur in rotationally-symmetric systems. Cubic distortions appear in both types of systems. Defocus errors that are quadratic as a function of field angle are caused when the field curvatures of the individual arms don't match.

Chapter 5 also shows a more rigorous way to derive the correction methods discussed in Chapter 4. If a general, plane-symmetric wavefront is compared to a perfect wavefront, constraints on the plane-symmetric aberration coefficients appear. These constraints lead to the correction methods discussed above: focal length must match, image planes shouldn't have relative tilts, etc. These relationships also show that in certain cases, equal amounts in each aperture of quadratic pistons, cubic pistons, quadratic and cubic distortions, and field curvatures may be tolerable.

Chapter 6 shows the application of the design rules in Chapter 4 to two designs with 100 meter baselines. The first system is a rotationally-symmetric, three-mirror Paul system. It has been segmented so that it behaves like a multiple aperture system. We show that the system satisfies the first-order design rules discussed in

Chapter 4. A second system uses an array of four afocal telescopes that then share a combining system. It achieves a smaller FOV than the previous system, because the low-order design rules in Chapter 4 must be satisfied with some of the available degrees of freedom. We discuss how the rules are satisfied for the system. A comparison of the two systems shows that the afocal array has some distinct advantages over the first system: it is more compact, the tolerances are not as tight, and the mirrors are easier to fabricate, among other things. It has the disadvantage of using more reflections per arm than the Paul system does.

Chapter 7 covers the design of a first-light beam combiner for the Large Binocular Telescope. The requirements for the beam combiner are discussed, and the design process is covered. The final design achieves a 1 arcminute field of view and uses two fold flats and an off-axis ellipse in each arm. The performance of the beam combiner is examined in terms of the low-order design rules. A first-order tolerance analysis shows that one of the beam combiner's mirrors will have to be actively controlled.

Chapter 8 explores a space telescope design that uses flat membrane mirrors in a large array. A single branch of the system is studied in detail, and the methods used to satisfy the low-order design rules are discussed. Each branch in the system has only three mirrors, and some of the design rules cannot be satisfied. An interesting trade-off must be made, since the focal lengths of the system cannot be forced to match without introducing a constant defocus error. Calculation of the RMS wavefront errors showed that the constant defocus error should be corrected before the linear tilt error. In addition, the RMS wavefront error is calculated analytically for a general branch, and can then be calculated for any system of branches. This allows an easy exploration of parameter space for these systems. The RMS calculations for several systems are compared to full raytrace models and found to be accurate.

Finally, Appendix A discusses the software used for this work. Diffraction analysis was done in Mathematica, while raytracing was done in Zemax and Optima. A brief tutorial in each software package is given using a two-aperture example system.

Chapter 2

MULTIPLE APERTURE SYSTEM BASICS

In this chapter, the basic concepts underlying multiple aperture systems are discussed. The point spread function of an optical system is defined, and demonstrated for single and multiple mirror telescopes. The optical transfer functions are also defined and demonstrated. The differences between monochromatic and polychromatic PSFs are examined. Resolution, sensitivity, and fill factors are discussed, and the factors that influence these performance measures are given. Finally, a few terms that are used routinely in optical design are redefined for use in multiple aperture systems.

2.1 The monochromatic point spread function and transfer function

The point spread function (PSF) of an optical system gives the intensity in the image plane when the object is a single point source. The PSF shows how much a point source is "spread" by travelling through the optical system. For telescope design, the object is taken to be an infinite distance from the optical system. Diffraction theory asserts that the image of an optical system is related to the Fourier transform of the amplitude in the entrance pupil, properly scaled and squared.[27] Then the PSF is generally given by:

$$\begin{aligned} I(x,y) &= \|F\left[A(x,y)\right]\|^2 |_{\zeta=y/\lambda f,\eta=x/\lambda f} \\ &= \left\| \int_0^\infty \int_0^\infty A(x,y) e^{i2\pi(\zeta y+\eta x)} \delta\zeta\delta\eta \right\|^2 |_{\zeta=y/\lambda f,\eta=x/\lambda f} \end{aligned} \tag{2.1}$$

where $A(x,y)$ is the amplitude in the entrance pupil of the optical system, λ is the wavelength of light, f is the focal length of the optical system, and F indicates the Fourier transform operation.

The optical transfer function (OTF) of an optical system gives percent transmission versus spatial frequency.[27] It describes how well a given spatial frequency is transmitted by the optical system. In the case of incoherent imaging (the phase at one point of the object is unrelated to the phase at another point), the OTF can be calculated as the autocorrelation of the function that describes the shape of the entrance pupil, normalized to a height of 1.[28] If K represents a scaling factor, then the optical transfer function is:

$$B(x,y) = K \int_0^\infty \int_0^\infty A(x,y)A(\alpha - x, \beta - y)\delta\alpha\delta\beta. \tag{2.2}$$

2.1.1 Single aperture

For a telescope with a circular aperture and an incident plane wave, the amplitude in the entrance pupil is constant and real. The amplitude in the entrance pupil and the PSF for a circular aperture of diameter D is then:

$$\begin{aligned} A(r) &= \sqrt{a} \text{ if } r < \frac{D}{2}, 0 \text{ if } r > \frac{D}{2} \\ I(r) &= \left\| \sqrt{a} D^2 \frac{4\lambda f}{\pi D} J_1\left(\frac{\pi D}{4\lambda f} r\right) \cdot \frac{1}{r} \right\|^2 \end{aligned} \tag{2.3}$$

where a is the intensity of the incident plane wave. This calculation assumes that the light is monochromatic, and has been carried out in a cylindrical coordinate system so that r equals $\sqrt{x^2 + y^2}$. The parameter J_1 refers to the first-order Bessel function of the first kind. The PSF is plotted in Figure 2.1. The first zero in the function $J_1(x)/x$ occurs at $x = 1.22$, so the width of this PSF can be estimated as $2.44\lambda f/D$.

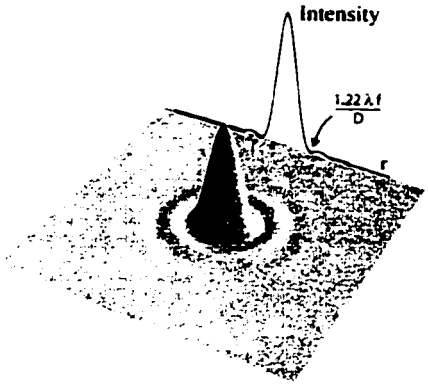

FIGURE 2.1. *The point spread function for a circular aperture with a diameter D.*

The OTF of a circular aperture is plotted in Figure 2.2. Notice that the system transmits no spatial frequencies above $\frac{D}{\lambda f}$, which is the cutoff frequency for this system. It is proportional to the diameter of the telescope, so increasing the size of the telescope will cause higher spatial frequencies to be transmitted by the system.

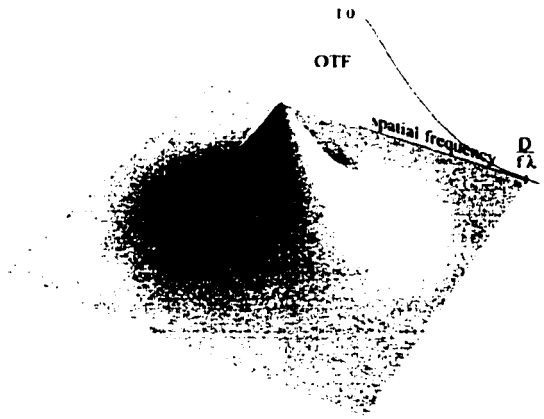

FIGURE 2.2. *The transfer function for a circular aperture of diameter D.*

2.1.2 Two apertures

If two circular apertures of diameters D_1 and D_2 are used as part of a system of two apertures, the pupil can be described by:

$$A(x,y) = Cyl\left(\frac{1}{D_1}\sqrt{(x-x_1)^2+(y-y_1)^2}\right) + Cyl\left(\frac{1}{D_2}\sqrt{(x-x_2)^2+(y-y_2)^2}\right) \quad (2.4)$$

assuming that the incident plane wave has an amplitude of one, and that the centers of the apertures are located at (x_1, y_1) and (x_2, y_2). The function $Cyl(r) = 1$ if $r < 1$ but equals 0 if $r > 1$. The corresponding image irradiance is then given by:

$$\begin{aligned} I(x,y) &= \left(\frac{\pi D_1^2}{4}\right)^2 Somb^2\left(\frac{D_1}{\lambda f}r\right) + \left(\frac{\pi D_2^2}{4}\right)^2 Somb^2\left(\frac{D_2}{\lambda f}r\right) \quad (2.5)\\ &\quad +2\left(\frac{\pi D_1^2 D_2^2}{4}\right)^2 Somb\left(\frac{D_1}{\lambda f}r\right) Somb\left(\frac{D_2}{\lambda f}r\right)\cos\left[\frac{2\pi}{\lambda f}(x_1-x_2)x + \frac{2\pi}{\lambda f}(y_1-y_2)y\right] \end{aligned}$$

This image is the sum of three parts: an image from the first aperture, an image from the second aperture, and a set of cosine fringes under an envelope. The frequency of the cosine fringes clearly depends on the baseline separations. The *Somb* functions act as an envelope over the cosine fringes, controlling the amplitude of the fringes.

If both apertures have the same diameter of D and the x-axis is chosen to lie on the line joining their centers, then the corresponding PSF irradiance simplifies to the following:

$$I(x,y) = \left(\frac{\pi D^2}{2}\right)^2 Somb^2\left(\frac{D}{\lambda f}\sqrt{x^2+y^2}\right)\cos^2\left(\frac{2\pi}{\lambda f}\frac{\Delta}{2}y\right) \quad (2.6)$$

where Δ is the distance between the apertures, as shown in Figure 2.3.

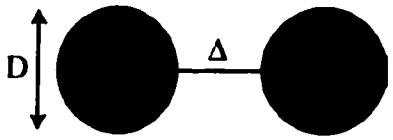

FIGURE 2.3. *The entrance pupil of a two-aperture system, with mirror diameters D and a baseline length* Δ.

The PSF in equation 2.6 is plotted in Figure 2.4. Perpendicular to the baseline Δ, the PSF cross-section is identical to that of the single circular aperture's, because

the diameter of the system is unchanged in that direction. Parallel to the baseline, though, the width of the PSF is reduced by the interference of the two apertures to $2\lambda f/\Delta$, which is roughly the same as the width of the circular PSF but with the new system "diameter" of Δ substituted for the aperture diameter D. The PSF can be made narrower by increasing the baseline length, then. The height of the fringes is governed by an envelope equal to the single mirror's image.

Decreasing the aperture diameters causes the envelope over the fringes to broaden. This has the effect of letting more of the fringes appear in the PSF, rather than just the three large fringes shown in the figure. The figure's PSF was calculated for relatively large apertures on a short baseline. The number of fringes for a two-aperture system is just the envelope width divided by the fringe width, or $1.22\Delta/D$. In general, fewer fringes give a better imaging system. The side lobes in the PSF are not useful; they just act as noise in other parts of the image, so the ideal PSF is a single peak with no side lobes.

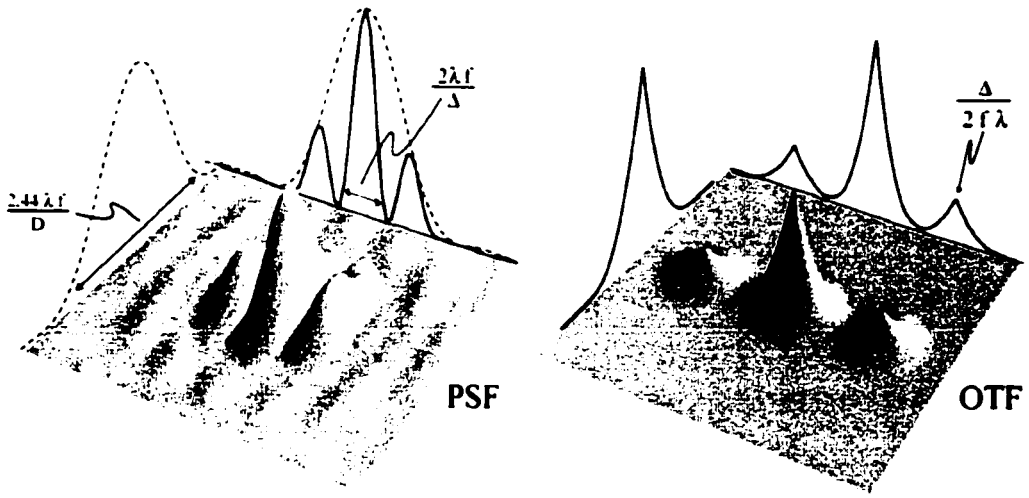

FIGURE 2.4. *The PSF and OTF for a two-aperture system.*

The OTF of the two-aperture system is also shown in Figure 2.4. The maximum spatial frequency transmitted by the system is now $(D + \Delta)/(f\lambda)$. The width of

the OTF's center lobe is the same as the width of the single aperture's OTF. The side lobes appear because the spatial frequency corresponding to the baseline Δ is transmitted by the system very well, giving secondary peaks at $\pm\Delta/(2f\lambda)$.

2.1.3 Three or more apertures

Every multiple aperture system can be treated as a collection of two-aperture telescopes. The PSF for any number of apertures is just an extension of equation 2.5. Each aperture will produce an image, and each pair of apertures will produce a set of cosine fringes under an envelope. For example, the PSF from a system of three apertures will be:

$$\begin{aligned} I(x,y) \;=\; & \left(\tfrac{\pi D_1^2}{4}\right)^2 Somb^2\left(\tfrac{D_1}{\lambda f}r\right) + \left(\tfrac{\pi D_2^2}{4}\right)^2 Somb^2\left(\tfrac{D_2}{\lambda f}r\right) + \left(\tfrac{\pi D_3^2}{4}\right)^2 Somb^2\left(\tfrac{D_3}{\lambda f}r\right) \\ & +2\left(\tfrac{\pi D_1^2 D_2^2}{4}\right)^2 Somb\left(\tfrac{D_1}{\lambda f}r\right) Somb\left(\tfrac{D_2}{\lambda f}r\right) \cos\left[\tfrac{2\pi}{\lambda f}(x_1-x_2)x + \tfrac{2\pi}{\lambda f}(y_1-y_2)y\right] \\ & +2\left(\tfrac{\pi D_1^2 D_3^2}{4}\right)^2 Somb\left(\tfrac{D_1}{\lambda f}r\right) Somb\left(\tfrac{D_3}{\lambda f}r\right) \cos\left[\tfrac{2\pi}{\lambda f}(x_1-x_3)x + \tfrac{2\pi}{\lambda f}(y_1-y_3)y\right] \\ & +2\left(\tfrac{\pi D_2^2 D_3^2}{4}\right)^2 Somb\left(\tfrac{D_2}{\lambda f}r\right) Somb\left(\tfrac{D_3}{\lambda f}r\right) \cos\left[\tfrac{2\pi}{\lambda f}(x_2-x_3)x + \tfrac{2\pi}{\lambda f}(y_2-y_3)y\right] \end{aligned} \tag{2.7}$$

The pupil and PSF of a three aperture system are shown in Figure 2.5. Each of the fringe patterns is perpendicular to the baseline of the pair of apertures that produced it.

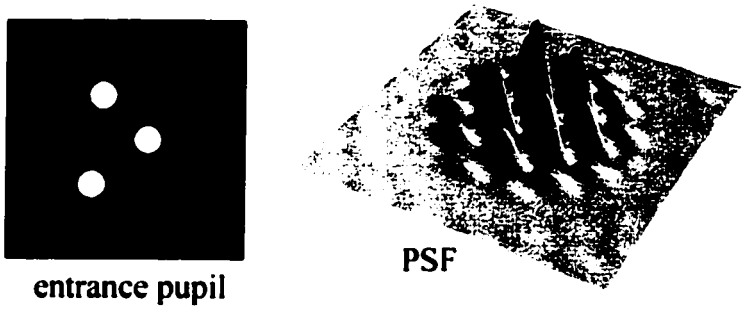

FIGURE 2.5. *The entrance pupil configuration and PSF of a three-aperture system.*

The MTF is also a logical extension of the two-aperture MTF. The two-aperture system had three peaks in the MTF: a central peak and peaks at $\pm\Delta/(2\lambda f)$. In fact, the number of peaks in the MTF will always be $2n + 1$, where n is the number of different baselines in the system. A system of three apertures can be positioned at unequal distances, and three different baselines will result. The three-dimensional MTF will then have seven peaks, as shown in Figure 2.6. If the three apertures are placed in a row at equal distances, though, there are only two distinct baselines, since two of the baselines possible have the same length. The MTF will have 5 peaks, as shown in Figure 2.7. The pair of peaks corresponding to the redundant baseline will be higher than the peaks corresponding to the single, longest baseline. Given n apertures, one can choose to maximize the number of peaks in the system, or one can choose to sample one frequency with a higher transmission using redundant baselines, depending on the application. Work has been done on the ideal configurations for primary telescopes in an array.[8]

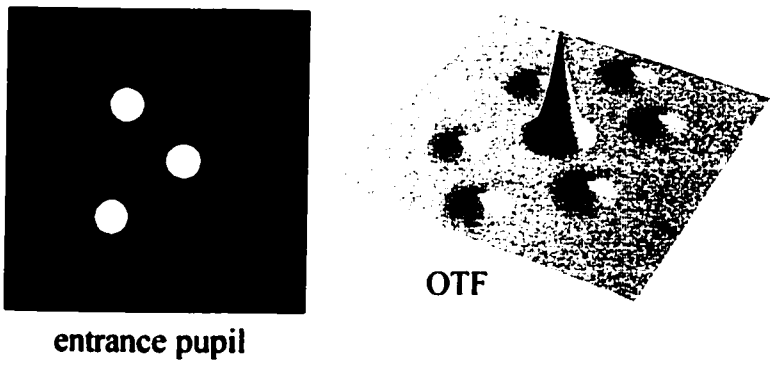

FIGURE 2.6. *The OTF of a three-aperture system with baselines of three different lengths has seven peaks.*

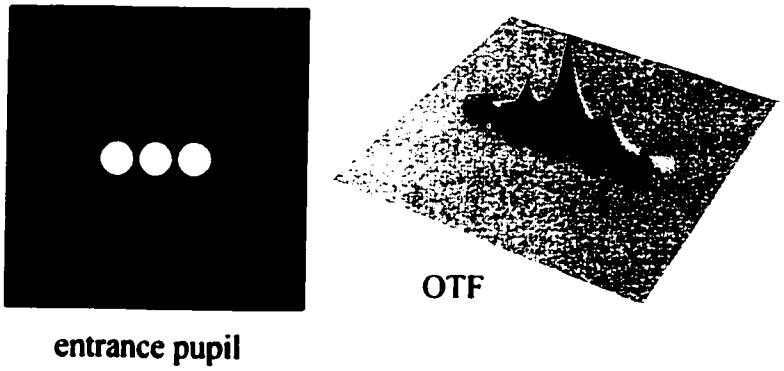

FIGURE 2.7. *The OTF of a three-aperture system with two baselines of equal length has only five peaks. The frequency corresponding to the redundant baselines has a higher transmission.*

For any number of apertures, as the diameters of the apertures decrease the OTF will retain its peak frequencies but will become narrower about those peaks. Intermediate frequencies are not transmitted as well through the smaller apertures, since the number of "baselines" available has been reduced.[6],[7] For example, in the three-aperture system shown in Figure 2.8, let each aperture have diameter D and both baselines have the length δ. The baselines inside a single aperture have every baseline from 0 to D, producing the center peak and its width. The baselines available between one mirror and its neighbor are $(\delta + D)$ at maximum and $(\delta - D)$ at minimum, producing the second set of peaks. The two separated apertures have available baselines between $(2\delta + D)$ and $(2\delta - D)$, producing the outer peaks.

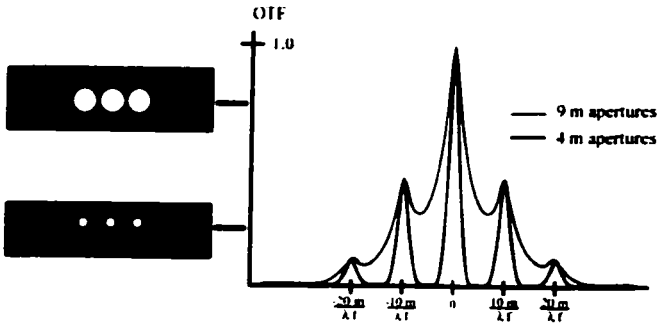

FIGURE 2.8. *The transfer function in a multiple aperture system gets narrower about its peaks as the aperture size is reduced.*

2.2 Polychromatic PSF and temporal coherence

The polychromatic PSF is just the integral over the object's spectrum of the monochromatic PSF. In general, the width of the PSF depends on wavelength, as shown for the two aperture case in equation 2.5. Adding many monochromatic images together, each of a different width, causes the visibility of the polychromatic fringes to be reduced.

This effect is shown in Figure 2.9, for the situation where the apertures are small (0.1 meters) compared to the system's baseline (10.01 meters). The focal length of the system was set to 100 meters. The source spectrum was considered to be rectangular, centered around 1 μm, with a bandwidth of 0.2 μm. The monochromatic fringes shown on the left sum to form the polychromatic PSF, which shows a reduction in fringe visibility as a function of position in the image plane.

The visibility of the fringes is given by the Fourier transform of the object's spectrum.[29],[30] Figure 2.9 shows that the contrast of the polychromatic fringes falls to zero, recovers a little, then falls again. This is the visibility envelope with the form $\sin(x)/x$, which is the Fourier transform of the rectangular object spectrum used in the calculation.[28]

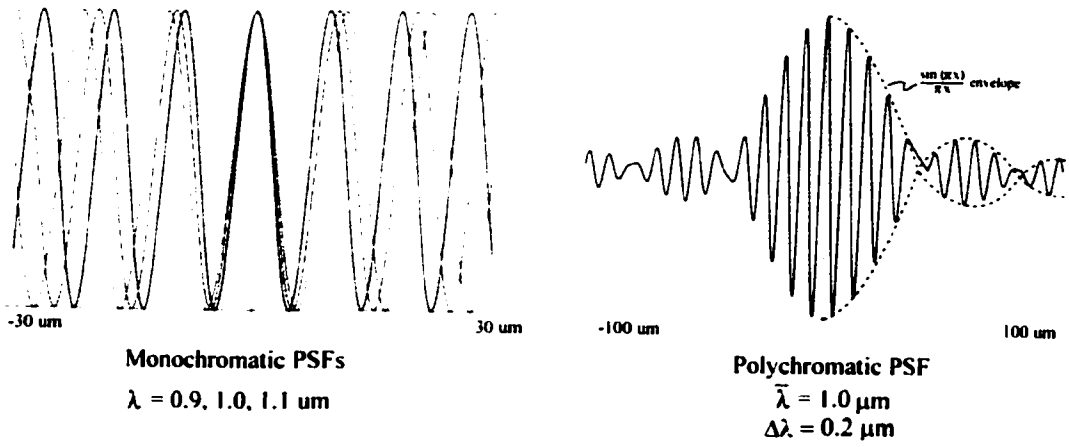

FIGURE 2.9. *A broad bandwidth drives the fringe visibility to zero. For a rectangular spectrum, the visibility envelope is a sin(x)/x function, the Fourier transform of a rectangular function.*

The first zero in the fringe visibility occurs when the pathlength difference between the two apertures is equal to the coherence length, as shown in Figure 2.10. The coherence length can be understood physically as the distance which light with a finite bandwidth can travel before the phases at each wavelength are random with respect to one another; thus no interference occurs between those wavelengths.

The coherence length leads to a coherence time, which is the time it takes the light to travel the coherence length: $l_c = c \cdot t_c$. The coherence time, in turn, may be estimated as the inverse of the spectral width of the object: $t_c = 1/\delta v$.

For a multiple aperture system, two beams that are separated in time from one another by more than the coherence time will not interfere constructively, but will have some degree of partial coherence.

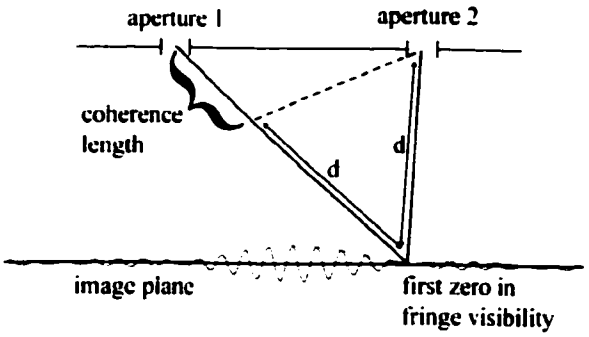

FIGURE 2.10. *The coherence length is the pathlength difference between two apertures and the point in the image where the fringe visibility first goes to zero.*

In certain cases, any reduction in fringe visibility will not be observed. If the aperture diameters are on the order of the baseline length in the system, then the diffraction envelope over the fringes is narrow. The diffraction envelope may go to zero amplitude before the fringe visibility goes to zero. This situation is shown in Figure 2.11, with apertures of 3 meters in diameter separated by a baseline of 10 meters, a focal length of 100 meters, an average wavelength of 1 micron, and a bandwidth of 0.2 microns. The loss of fringe visibility is just visible at the edges of the PSF.

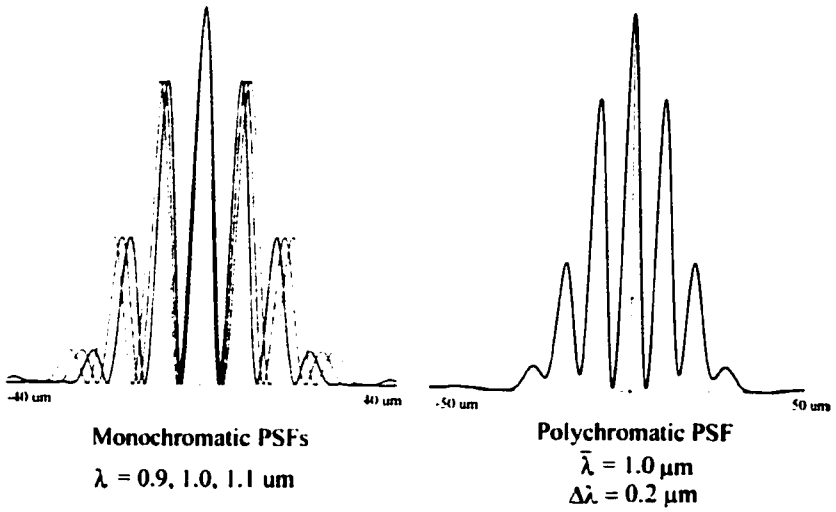

FIGURE 2.11. *If the aperture diameters are on the same order as the baseline length, the diffraction envelope is narrow, and any reduction in fringe visibility will not be observed.*

If the point source is moved off-axis, the visibility of the broadband fringes is not changed. The set of fringes just moves off center by $\alpha \cdot f$, where α is the field angle and f is the focal length of the optical system. The visibility of the fringes goes to zero the same distance away from this new center point.

In the case of this two-aperture system, the coherently combined image is 4 times higher than one of the individual images. The peak of the intensity pattern in the case of perfect beam combining will always be n^2 larger than the peak intensity in the image from an individual aperture, where n is the number of apertures in the system. This assumes equal sizes and incident intensities for each aperture. Partial coherence will cause a reduction in the peak image intensity.

2.3 Resolution

The point spread function is a useful quantity because an extended object can be considered to be a collection of point sources. The intensity in the image is then just

a convolution of the system's PSF with the collection of point sources.

The resolution of a system describes the minimum distance at which two points can be distinguished in the image. Figure 2.12 shows the convolution of two points with an interferometric PSF. It is clear that the resolution defined in this way must be equal to the width of the PSF. For the two-aperture example system, this width is $(2\lambda f/\Delta)$. Note that the term "high resolution" corresponds to a small number, since the width of the PSF must get narrower as the resolution gets higher.

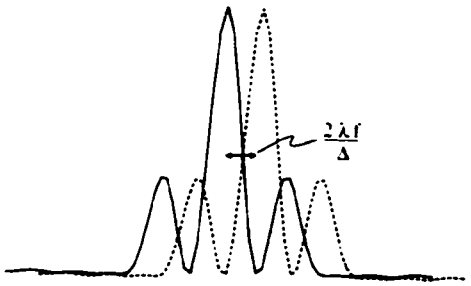

FIGURE 2.12. *An image formed by two point objects will be the convolution of the points with the system PSF. Resolution is defined as the minimum distance at which those two points can be distinguished by the telescope.*

A multiple aperture system may have many different resolutions, depending on the orientation of the field angle. In a two-aperture system with circular apertures, the highest resolution will be $(2\lambda f/\Delta)$, for field angles that move the image along the baseline. The lowest resolution will be $(2.44\lambda f/D)$, for field angles that move the image away from the baseline. At other field angles, any resolution between those two limits can occur.

Incidentally, this figure also demonstrates why side-lobes in a PSF are undesirable. The side lobes from one PSF will clearly add to the background noise at the location of the image of the second point source.

2.4 Sensitivity

Sensitivity is a measure of the faintest object that can be detected with a telescope system. It is generally proportional to the collecting area of the telescope, since larger apertures correspond to a stronger signal. A complete calculation of sensitivity also includes noise sources from the signal itself, the optical system, and the instrument and detector in use. This means that the sensitivity will not be strictly proportional to the collecting area.

2.5 Fill factor

A multiple aperture system whose baseline is large compared to its apertures is referred to as a "sparse" system. A system with large apertures on a relatively short baseline is a "filled" system. A telescope with a single, circular aperture is perfectly filled. The "fill factor" can be calculated as the ratio of the total collecting area to the collecting area of a single aperture with diameter equal to the longest baseline in the system. For the simple pupil shown in Figure 2.3, the fill factor would be: $(2\frac{\pi D^2}{4})/(\frac{\pi(D+\Delta)^2}{4}) = 2D^2/(D+\Delta)^2$.

This is inversely proportional to the number of fringes that appear in the PSF, so a higher fill factor has fewer fringes in the PSF, which is desirable. The fill factor also gives information about the OTF. A higher fill factor has an OTF that is "plump" – that is, the frequencies between the peaks of the OTF are transmitted well, as discussed above.

2.6 Performance summary

For a system of two aperture with diameters D and baseline Δ, the table below shows the various performance factors discussed. Increasing the baseline length leads to a higher resolution, increases the peak frequencies in the OTF, and produces a higher

cutoff frequency. Increasing the aperture diameter improves the sensitivity of the telescope, and also gives a higher cutoff frequency. Increasing the aperture diameter while holding the baseline constant leads to a higher fill factor, and thus a plumper OTF and a PSF with fewer fringes.

aperture diameters:	D
baseline length:	Δ
fill factor ("plumpness" of OTF):	$2D^2/(D+\Delta)^2$
sensitivity, proportional to:	$\pi D^2/2$
resolution:	$2\lambda f/\Delta$
number of fringes in PSF:	$1.22\Delta/D$
OTF frequency peaks:	$0, \pm\Delta/(2\lambda f)$
cutoff frequency:	$(D+\Delta)/(f\lambda)$

TABLE 2.1. *Performance parameters for a two-aperture system.*

2.7 A few definitions

Some standard system parameters need to be carefully defined for multiple aperture systems. For example, "chief ray" usually refers to a ray that passes through the center of the entrance pupil. In the case of multiple aperture systems, it may not be possible to trace a ray through the center of the entrance pupil. This is true for the system shown in Figure 2.13. Instead, "chief ray" will be used to refer to a ray traced through the center of any of the individual apertures at a non-zero field angle. An "axial ray" will refer to a ray traced through the center of any of the apertures at a field angle of zero. There is a chief ray and an axial ray for every aperture in a multiple aperture system.

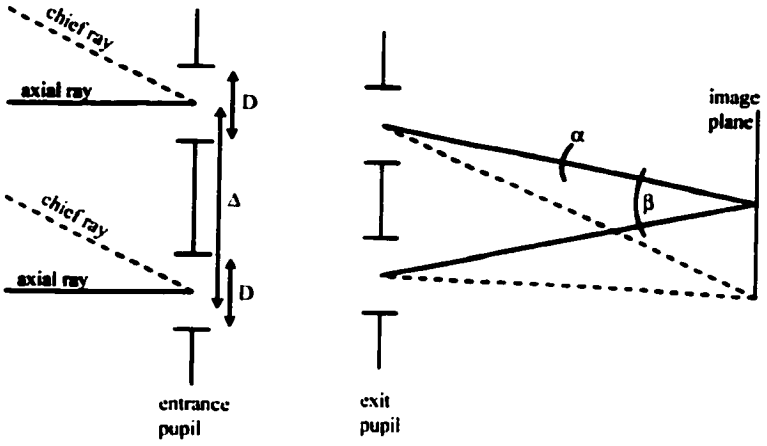

FIGURE 2.13. *Sketch showing some of the definitions used in multiple aperture systems.*

Each branch of a multiple aperture system has its own entrance and exit pupil. One of these sets must be selected as the entrance and exit pupil of the system, and their diameters adjusted to include all the apertures. The phases in the other apertures will be referenced to the wavefront in the selected system exit pupil.

Similarly, each branch of the multiple aperture system may have its own image plane. Again, one of the image planes must be chosen as the system image plane. All calculations must be referenced to the chosen image plane.

The f/# of a multiple aperture system also needs to be carefully defined. The f/# of an individual branch in a system will be the focal length of the branch divided by the diameter of the individual branch's entrance pupil. For a telescope, that is usually the diameter of the primary aperture. In Figure 2.13, the f/# of either of the branches will be f/D. The focal lengths of an individual branch and the entire system are equal, so the f/# of the system will be the focal length divided by the full diameter of the system entrance pupil. In Figure 2.13, the system f/# is $f/(\Delta + D)$.

2.8 Conclusions

In conclusion, the PSF of an optical system is the image of a perfect point source. The PSF of a multiple aperture system gets narrower with increasing baseline length, leading to higher resolution for the system. In the broadband PSF, a loss of fringe visibility occurs away from the center of the image. If the fill factor is high, though, the loss of visibility may not be observed. Side lobes in a PSF used for wide field imaging are not useful, and only add to the background noise in the image. The number of side lobes is inversely proportional to the fill factor of the system. A completely filled system will have no significant side lobes.

The optical transfer function is a plot of transmission efficiency versus spatial frequency. The cutoff frequency is proportional to the longest dimension in the entrance pupil of the multiple aperture system. The OTF shows good transmission for zero frequency and frequencies related to the baseline lengths in the system. Redundant baselines increase the transmission efficiency at the associated frequency. Reducing the aperture diameters in a multiple aperture system causes a narrowing of the OTF about its peaks.

Sensitivity in a multiple aperture system is proportional to total collecting area in the system, but must also account for noise sources in the particular instrument and detector used.

Some standard optical terms need to be clarified for the case of multiple aperture systems. Each aperture in a multiple aperture system has its own diameter, chief ray, axial ray, and f/#, exit pupil, and image plane. A single exit pupil and image plane must be chosen for the system. The system f/# is the focal length divided by the longest dimension of the system.

Chapter 3

BEAM COMBINING ERRORS

This chapter discusses the perfect image and the effects of low-order beam combining errors on that image. Investigating the two-aperture case is useful, since a system of any number of apertures can be treated as a collection of two-aperture systems.

3.1 The perfect image

As discussed in chapter one, the monochromatic image from a general two-aperture system is given by:

$$\begin{aligned} I(x,y) &= \left(\tfrac{\pi D_1^2}{4}\right)^2 Somb^2\left(\tfrac{D_1}{\lambda f}r\right) + \left(\tfrac{\pi D_2^2}{4}\right)^2 Somb^2\left(\tfrac{D_2}{\lambda f}r\right) \\ &\quad +2\left(\tfrac{\pi D_1^2 D_2^2}{4}\right)^2 Somb\left(\tfrac{D_1}{\lambda f}r\right) Somb\left(\tfrac{D_2}{\lambda f}r\right)\cos\left[\tfrac{2\pi}{\lambda f}(x_1-x_2)x + \tfrac{2\pi}{\lambda f}(y_1-y_2)y\right] \end{aligned} \tag{3.1}$$

where D_1 and D_2 are the aperture diameters, λ is the wavelength, f is the focal length of the system, and the coordinates (x_1, y_1) and (x_2, y_2) are the positions of the aperture centers.

This image is the sum of three parts: an image from the first aperture, an image from the second aperture, and a set of cosine fringes under an envelope.

There are really only four kinds of errors that can make this image imperfect, then:

- the images from each aperture can separate laterally
- the images from each aperture can separate longitudinally
- the images from each aperture can cease to combine coherently

- the images from each aperture can be aberrated

The effect of each of these errors on the PSF is demonstrated below.

3.2 Reduction in coherence (piston errors)

If two beams arrive in an image plane simultaneously, they will be perfectly coherent and will interfere constructively. If the arrival time of one beam is delayed, however, the beams may interfere with only partial coherence, or may even interfere destructively. Coherence is lost if the time delay is greater than the coherence time, $t_c = 1/\Delta v$, where Δv is the width of the object's spectrum.

Such a time delay can be represented mathematically by a constant phase error in one of the interfering beams. The constant phase error is often referred to as a piston error. For a two-aperture system with aperture diameters D, baseline length Δ, and an incident plane wave of amplitude 1, the entrance pupil amplitude can be represented by:

$$A(x,y) = Cyl\left(\tfrac{1}{D}\sqrt{(x-\tfrac{\Delta}{2})^2+y^2}\right) + Cyl\left(\tfrac{1}{D}\sqrt{(x+\tfrac{\Delta}{2})^2+y^2}\right)\cdot e^{i2\pi\delta} \qquad (3.2)$$

where δ is the constant phase error between the apertures, in waves. The amplitude and phase are plotted in Figure 3.1.

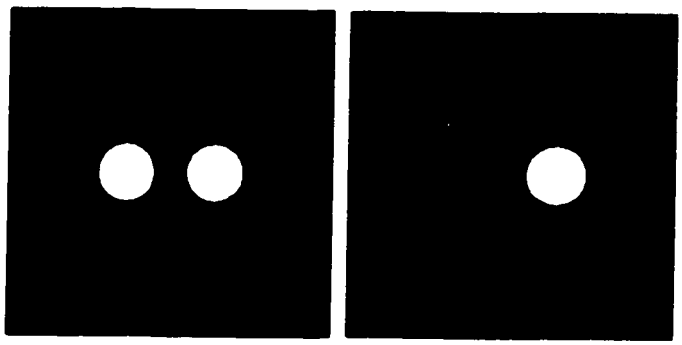

FIGURE 3.1. *The irradiance and phase in the pupil of a two-aperture system with piston errors.*

The associated polychromatic PSF is:

$$I(x,y) = \sum_{\lambda} A_\lambda \left(\frac{\pi D^2}{2}\right)^2 Somb^2\left(\frac{D}{\lambda f}\sqrt{x^2+y^2}\right)\cos^2\left(\pi\delta + \frac{\pi\Delta}{\lambda f}x\right). \qquad (3.3)$$

where A_λ is the height of the spectrum at a given wavelength. The equation shows that the piston, δ, shifts the cosine fringes but doesn't shift the associated *Somb* envelope. With increasing amounts of piston, then, the fringes "walk" out from under the envelope.

If the light were monochromatic, the fringe pattern would extend forever in space. A fringe would be located at the peak of the *Somb* envelope every time δ was an integer number of wavelengths. The fringe shift would have little effect on the performance of the system, then. But broadband, the fringes have a visibility envelope, as shown in Chapter 2. Broadband, the fringes have a distinct center. Moving the envelope away from that fringe center will steadily decrease the contrast in the combined image.

Images with increasing amounts of piston error are shown in Figure 3.2. The fringe visibility steadily degrades for increasing errors, until the final image is just two overlapping images without any interference. The fringe center has moved completely away from the individual images, leaving two incoherently-combining images. Equivalently, the two beams have arrived in the image plane with a time delay between them greater than a coherence time, or a spatial delay greater than the coherence length.

The calculations for Figure 3.2 are for a two-aperture system with a baseline of 14.4 meters and aperture diameters of 8.4 meters. The spectrum was rectangular, centered on $\lambda = 4.8\ \mu m$ and with a width of $1.2\ \mu m$. This gives a coherence length of about 16 μm, since $\Delta\nu = 1.85 \cdot 10^{13} Hz$ and $t_c = 5.4 \cdot 10^{14}$ sec.

In multiple aperture telescopes, incoherent combination can be used to improve the signal to noise ratio over that of a single mirror telescope. The collecting area

is increased over that of a single mirror, but the resolution is not improved. This is referred to as the "light bucket" mode of operation.

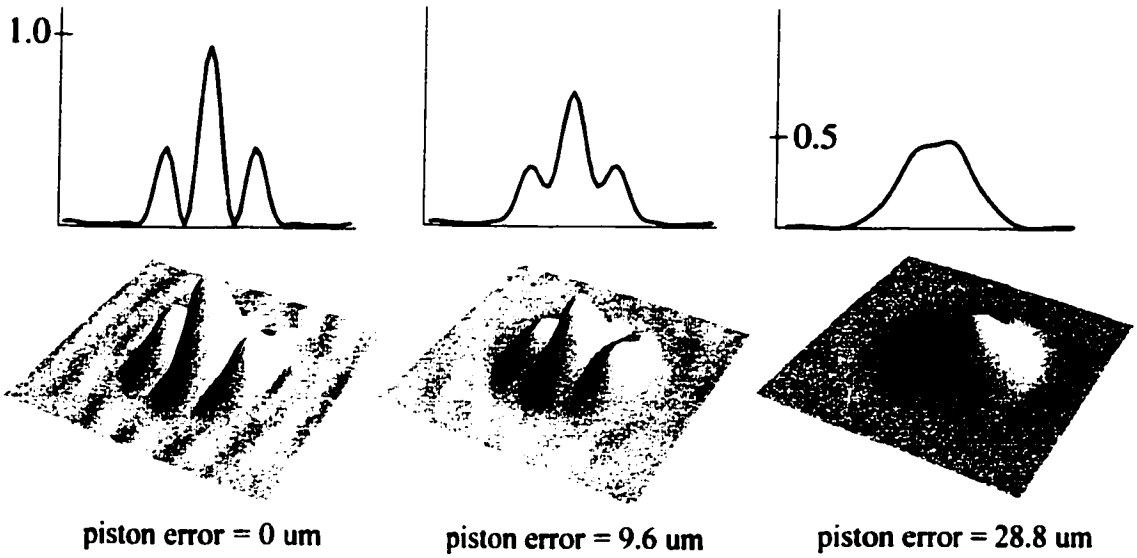

FIGURE 3.2. *The PSF for a two-aperture system with piston errors. The fringe visibility decreases with increasing amounts of piston error. The coherence length of the spectrum is 16 μm.*

For small piston errors, the Strehl ratio is related to the RMS wavefront error in the system. This will be discussed in more detail in Chapter 4. For large piston errors, the height of the PSF will have 1/2 of its unaberrated value, since the two images overlap but don't combine coherently. The Strehl ratio as a function of piston error is shown in Figure 3.3 for a two aperture system with apertures 8.4 meters in diameter on a baseline of 14.4 meters, in the M-band centered on 4.8 μm. The Strehl ratio here is taken to be the peak PSF intensity with aberrations divided by the peak PSF intensity with no aberrations present. It levels off at a value of 1/2. In the case of n apertures, the behavior of the system is similar. A large piston between any pair of apertures will prevent those two images from combining coherently. For a out of n apertures having large piston errors, the Strehl ratio will fall to $(n-a)/n$.

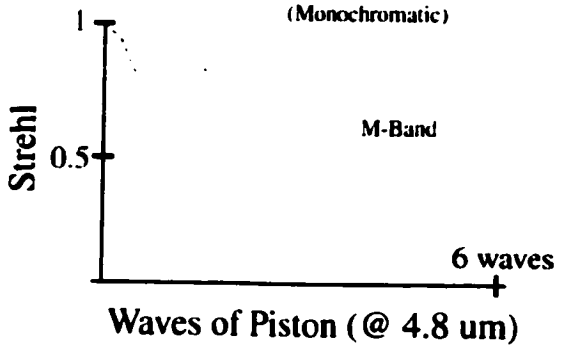

FIGURE 3.3. *For large piston errors, the Strehl falls to 1/2 for a two-aperture system. The images from each aperture still overlap, but don't interfere.*

There are several other interesting features shown on this plot. As discussed above, if the effect of the piston error is calculated monochromatically, the image will return to perfect each time the pathlength error between the arms is an integer number of wavelengths. This is shown by the dotted line in Figure 3.3. This is equivalent to assuming that the coherence length of the system is infinite - the images will interfere with one another no matter how much they're separated by phase. This doesn't represent reality, since an infinite coherence length corresponds to an infinitely narrow wavelength filter, which would pass zero photons through to the system.

In the polychromatic case, shown by the solid line in the plot, the fringes have a visibility envelope. This visibility envelope prevents the Strehl from recovering once the fringe center has moved away from the envelope.

Figure 3.3 also shows discontinuities in the plot of Strehl vs. piston error. This feature does not appear in single-aperture systems. For multiple aperture systems, the peak of the PSF cannot be assumed to fall at the geometrically predicted image center. To calculate a Strehl ratio, the peak of the image must be located before it is measured. The discontinuity in Figure 3.3 occurs when one peak in the image becomes larger than another peak of the image - the Strehl ratio "jumps" from

measuring one peak to measuring another. For more complicated systems, this may happen many times, producing many bumps in the Strehl as a function of piston error.

3.3 Lateral image separation (tilt errors)

The individual images can separate in space anytime there is a tilt phase error in the wavefront. The analytic representation of the pupil amplitude is similar to that of Equation ??, except for a phase term that is linear as a function of position on the second aperture:

$$A(x,y) = Cyl\left(\frac{1}{D}\sqrt{\left(x+\frac{\Delta}{2}\right)^2+y^2}\right) + e^{i4\pi\alpha(x-\frac{\Delta}{2})/(D\lambda)}Cyl\left(\frac{1}{D}\sqrt{\left(x-\frac{\Delta}{2}\right)^2+y^2}\right) \quad (3.4)$$

where α is the waves of tilt at one edge of the aperture. Assuming no other aberrations in the system, the image irradiance for a point object will be as follows:

$$I(x,y) = \left\{\frac{\pi D^2}{2}\cos(\frac{\pi\Delta}{\lambda f}x)\left[Somb\left(\frac{D}{\lambda f}\sqrt{x^2+y^2}\right) + Somb\left(\frac{D}{\lambda f}\sqrt{(x-\frac{2\alpha f}{D})^2+y^2}\right)\right]\right\}^2 \quad (3.5)$$

As expected, the total image consists of an unshifted image from one aperture and a shifted image from the second aperture. The cosine fringes are also unshifted, but their amplitude is modified by the product of the two individual images.

Figure 3.4 shows the pupil irradiance and phase for a two-aperture system with a tilt error on one aperture.

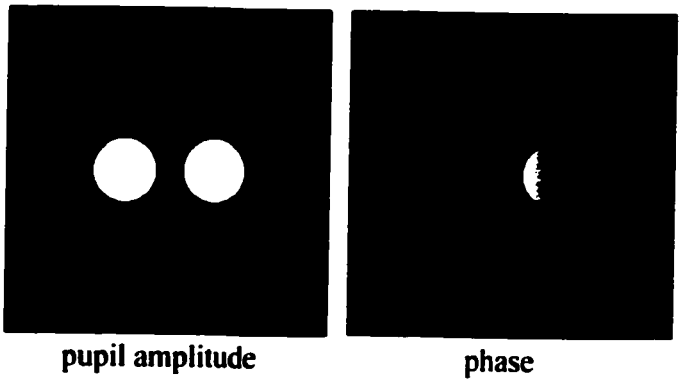

FIGURE 3.4. *The irradiance and phase plots for a two-aperture system. A tilt in phase is present on one of the apertures.*

Plots of the images from the system are shown in Figure 3.5, with increasing amounts of tilt in each image. The final frame shows that one of the images is almost completely unaffected by the other. This happens when the tilt angle is roughly twice the width of the Somb functions, or at $a = 2.4\lambda$, which gives about 2.5 waves of tilt at one edge of the tilted apertures. This calculation was done at 1 μm for 9 meter apertures on a 14 meter baseline.

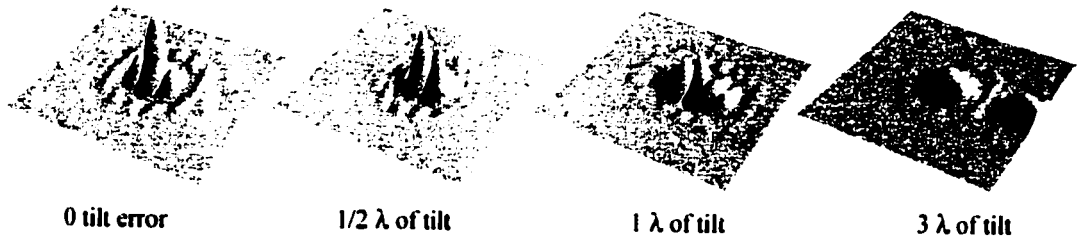

FIGURE 3.5. *Point spread functions from a two-aperture system, with increasing amounts of a tilt phase error in one aperture. The last figure shows the individual images completely separated in space.*

As shown in Figure 3.6, the peak intensity when the images have completely separated is 1/4 that of the perfectly combined image, if both apertures had the same incident amplitude.

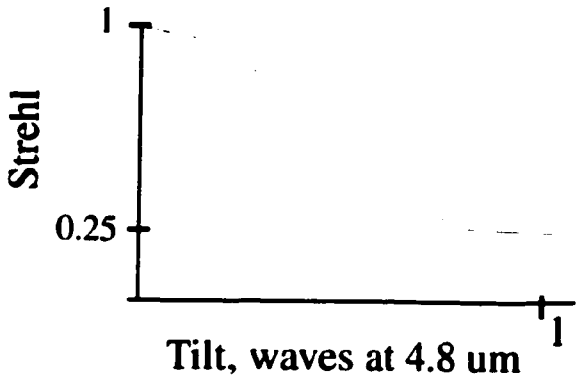

FIGURE 3.6. *The Strehl ratio falls as a function of tilt error in one of the apertures. When the two images are completely separate, the Strehl falls to 1/4, since all interference is gone.*

The particular example shown in Figure 3.6 was calculated for two apertures 8.4 meters in diameter on a 14.4 meter baseline.

The Strehl for a larger number of apertures shows similar behavior. The image from any one aperture with a large tilt error will move away from the other images. For a out of n apertures with large tilt errors, the Strehl ratio will be $(n-a)^2/n^2$, where a must be less than n, since one of the images must be defined as having the correct location. For small tilt errors, the Strehl ratio is related to the RMS wavefront error. This will be discussed in Chapter 4.

3.4 Longitudinal image separation (defocus errors)

The combined image will be degraded if the images separate longitudinally, moving in or out of the image plane. The axial rays in each branch may still overlap in such a case, but one beam comes to focus too soon or too late. This is equivalent to a quadratic phase error in one aperture, or a power error. The amplitude in the pupil for a two-aperture system with a defocus error in one of the apertures can be written as:

$$A(x,y) = Cyl\left(\frac{1}{D}\sqrt{\left(x+\frac{\Delta}{2}\right)^2+y^2}\right) + e^{i2\pi\frac{\beta}{\lambda}((x-\frac{\Delta}{2})^2+y^2)/((D/2)^2)} Cyl\left(\frac{1}{D}\sqrt{\left(x-\frac{\Delta}{2}\right)^2+y^2}\right) \tag{3.6}$$

where D is the diameter of both apertures, Δ is the aperture separation, λ is the wavelength, and β is the defocus error in waves at the edge of the aperture.

Figure 3.7 shows the intensity and phase in the entrance pupil of a two aperture system. There is a power error in one of the apertures. Figure 3.8 shows the system images with increasing power error. In this case, one of the individual images is getting broader than the other while both images stay centered. The images were calculated at a wavelength of 1 μm for apertures 10 meters in diameter and separated by 14 meters.

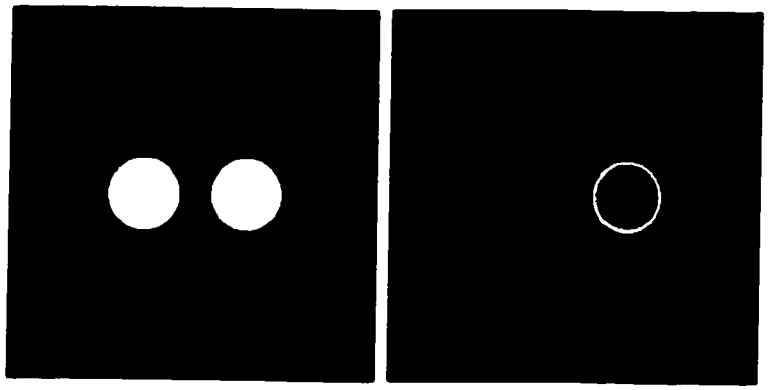

FIGURE 3.7. *The pupil irradiance and phase in the exit pupil of a two-aperture system, with a defocus error in one of the apertures.*

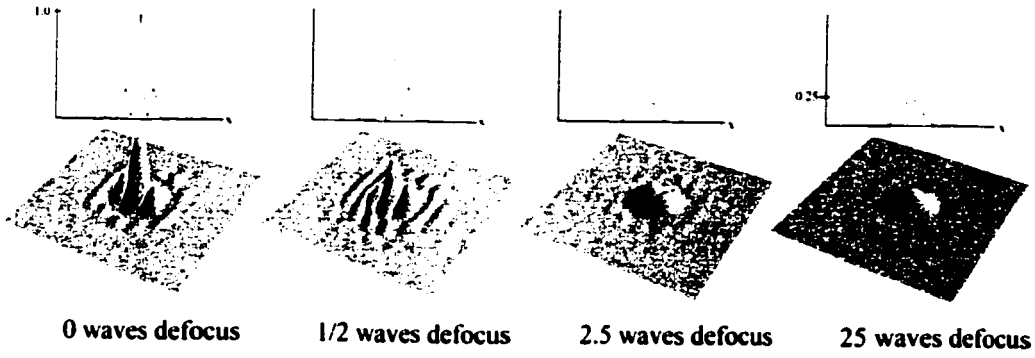

FIGURE 3.8. *Point spread functions from a two-aperture system, with increasing amounts of defocus error in one aperture.*

When the power error is very large, the image from one beam is effectively just a small, constant intensity over the width of the other image. The Strehl for large defocus errors will be 1/4 of the height of the combined image. This is shown in Figure 3.9, and this plot was created for the particular case of two aperture 8.4 meters in diameter on a 14.4 meter baseline.

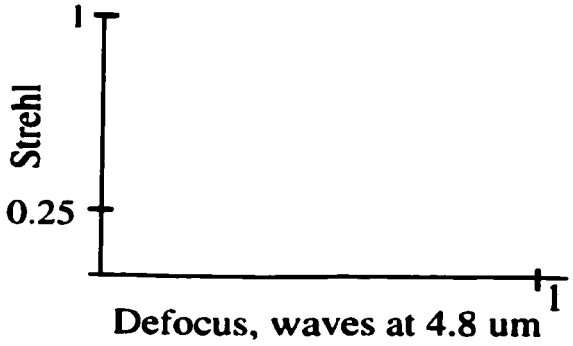

FIGURE 3.9. *The Strehl ratio from a two aperture system, falling with increasing amounts of defocus in one aperture.*

For more than two apertures, the effect of the defocus is very similar. Any aperture affected by a large defocus error will broaden so that it doesn't contribute to the final PSF. If 1 out of n apertures is defocussed, the PSF height for large

errors will be $(n-1)^2/n^2$ of the perfect PSF. If a apertures are defocussed, the Strehl for large errors will be $(n-a)^2/n^2$, where a must be less than n, because one of the images must be defined as lying in the correct focal plane. For small defocus errors, the Strehl will be related to the RMS wavefront error of the system, and this is dicussed in detail in Chapter 4.

3.5 Aberrations in the individual images

Aberrations in a single arm of the system will also affect the system performance. Figure 3.10 shows point spread functions from a system of two apertures, with increasing amounts of coma error in one of the apertures. The individual images are no longer perfect *Somb* functions, but are an aberrated version of the function. The combined image is also aberrated, then. These images were calculated for aperture diameters of 10 meters, a baseline of 7 meters, and a wavelength of 1 μm. The width of the central lobe is 14.3 μm.

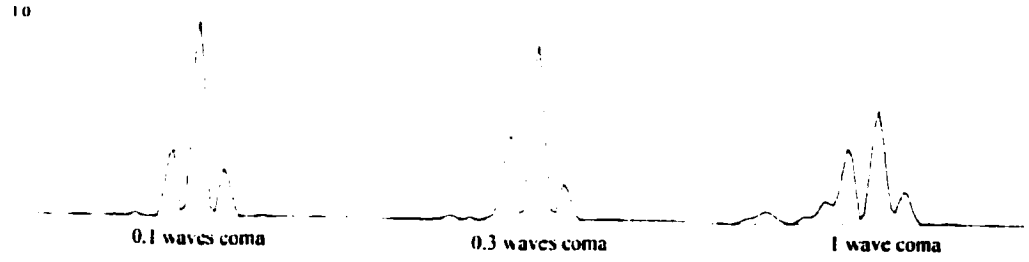

FIGURE 3.10. *The combined image from a two-aperture system with increasing amounts of coma in one of the apertures.*

It is tempting to think that equal amounts of a given aberration may improve the performance, since the spot diagrams in the image planes would have more overlap. However, this is generally not the case. This is easily seen if the wavefront of the whole system is considered, as shown in Figure 3.11. Equal amounts of coma are shown in the two apertures on the left. This appears to produce more overlap of the

spots in the image plane. But the wavefront considered as a whole is a very complex aberration that will degrade the system's performance. The system on the right, with only one aperture corrected, appears to have less image overlap, but is in fact the better combined image.

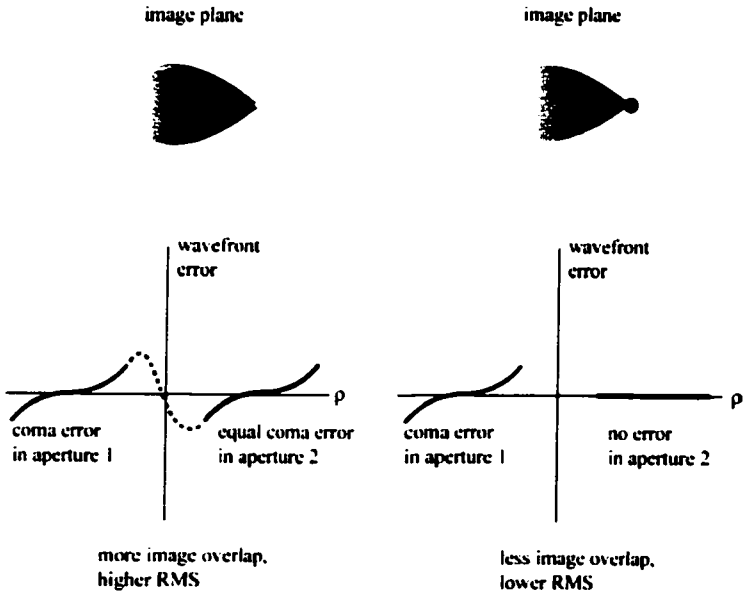

FIGURE 3.11. *Equal amounts of aberrations in each aperture produces more image overlap, but in fact aberration "matching" produces a high-order phase error in the pupil plane, degrading the combined image.*

Any aberration that causes deterioration of the individual image will cause deterioration of the combined image. Aberrations that move the individual images but do not affect their quality (such as equal amount of tilt) may be permissible in certain situations. This is discussed in more detail in Chapter 4.

3.6 Conclusions

The perfect image from a multiple aperture system is the sum of an image from each aperture and a set of fringes from each pair of apertures. Only four things can

prevent this image from being perfect. The beams can separate laterally in the image plane, the beams can separate longitudinally in the image plane, the beams can fail to combine coherently, or the individual images may be aberrated.

If the images fail to combine coherently, it is due to relative piston errors in the wavefront. Piston error is a constant phase error that doesn't depend on position in the pupil. Equation 3.3 shows that piston errors in the wavefront shift the fringes away from the images, causing them to combine incoherently. For large amounts of piston error in a two-aperture system, the Strehl will have a value of 1/2, since both images still overlap but combine incoherently.

Lateral image separation corresponds to tilt errors in the wavefront. The tilt error causes one image to move away from the other images. For large amounts of tilt in a two aperture system, the Strehl ratio will be 1/4, since one of the images' amplitudes has been removed from the final image.

Longitudinal image separation is due to defocus errors in the wavefront. One of the images is broadened by defocus until it contributes only a small constant amplitude to the final image. For large amounts of defocus in a two aperture system, the Strehl ratio will be 1/4 since one of the images' amplitudes has been removed from the final image.

Chapter 4

QUANTIFYING AND CORRECTING LOW-ORDER ERRORS

In the previous chapter, the effects of tilt, piston, and defocus errors on the perfect image were demonstrated. In this chapter, the physical sources of these errors will be discussed. Each type of error can occur as any function of field angle. The errors that are constant and linear as a function of field angle are demonstrated and corrected. The RMS wavefront error in the presence of these errors are calculated and used to predict an example system's performance.

4.1 Wavefront reconstruction

The beam combining errors discussed in the previous chapter were: lateral image separation (tilt), longitudinal image separation (defocus), coherence of the image combination (piston), and aberrations of the individual images. These are the only errors that can cause the combined image to depart from perfect. Each of these errors can be identified in the wave fans of an aberrated system. Wave fans are plots of the phase departure of the real wavefront in the exit pupil from a perfect, spherical wavefront as a function of position in the exit pupil.

Unlike single-aperture systems, wave fans in multiple aperture systems can have discontinuities, as shown in Figure 4.1. The piston errors show up in the wave fans of the complete system as offsets of the wavefront in the aperture. Tilt errors appear as slopes at the aperture centers, and power errors show up as curvature of the wavefront within the aperture. Often, these errors show up in the wave fans in combination with higher-order problems. However, for small field angles, errors that are constant and linear as a function of field angle will certainly dominate the performance. It is logical to attempt to correct these errors from lowest to highest dependence on field

angle.

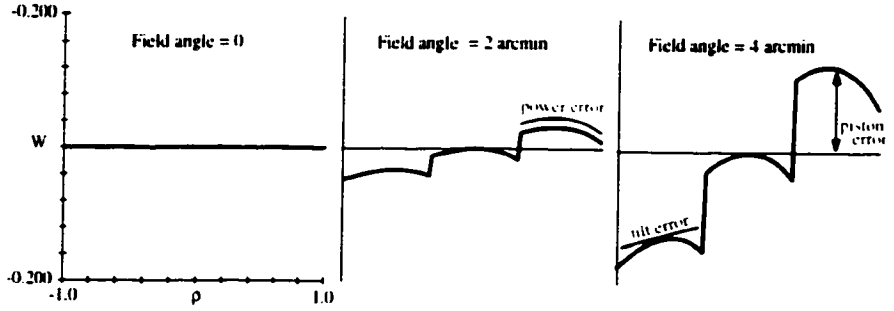

FIGURE 4.1. *Wave fans showing piston, tilt, and power errors increasing as a function of field.*

Wavefront reconstruction provides an easy way to estimate the wavefront error due to all of these lower-order combining errors. On-axis and linear tilt, power, and piston errors can be calculated as geometric distances and converted to wavefront errors. Wave fans such as the ones shown in Figure 4.1 can be reconstructed with a few simple geometric calculations, and the system RMS wavefront error and Strehl ratio calculated from the reconstruction. This estimation method avoids the difficulties of full raytrace modeling.

If there are many branches in the system, the RMS wavefront error, σ, for the whole system of apertures will be a sum weighted by the areas of each aperture, A_k:

$$\sigma = \sqrt{\frac{\sum A_k \cdot \sigma_k^2}{\sum A_k}} \tag{4.1}$$

where the RMS wavefront error in each aperture is calculated by:

$$\sigma_k^2 = \frac{1}{A_k} \iint_{A_k} (W_k - \langle W \rangle)^2 \delta A_k. \tag{4.2}$$

In this equation, W_k is the mathematical representation of the wavefront's departure from perfect in the k^{th} aperture (see section 3.1.1). The term $\langle W \rangle$ in equation 4.2 is the weighted average of the wavefront over all of the apertures:

$$\langle W \rangle = \frac{\sum A_k \langle W_k \rangle}{\sum A_k} \tag{4.3}$$

and the term $\langle W_k \rangle$ is the average wavefront error over the k^{th} aperture:

$$\langle W_k \rangle = \frac{\iint W_k \cdot \delta A_k}{A_k}. \tag{4.4}$$

Finally, for small wavefront errors, the RMS wavefront error is related to the Strehl ratio by:

$$S = e^{-(2\pi\sigma)^2}. \tag{4.5}$$

This calculation can be carried out for a set of field angles, so that the Strehl can be plotted versus field angle.

4.1.1 Wavefront coefficients for plane-symmetric systems

The term W_k must describe the wavefront's departure from perfect in the k^{th} aperture. The branches in the majority of multiple aperture systems have only a single plane of symmetry, and so W_k must describe a given error's dependence on field angle and pupil coordinate, with respect to the plane of symmetry.

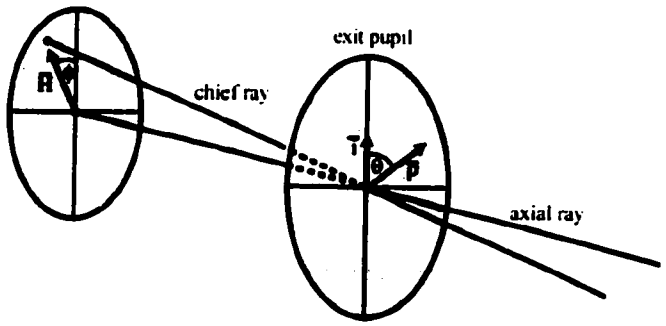

FIGURE 4.2. *Definitions for describing the wavefront's departure from perfect in a system with a single plane of symmetry. The vector $\vec{i}$ lies along the intersection of the plane of symmetry with the exit pupil.*

Let the unit vector $\vec{i}$ lie in the plane of symmetry of the branch. $\vec{H}$ is the field angle normalized by the maximum field angle in the system, and $\vec{\rho}$ is the coordinate

in the pupil normalized by the pupil's radius, as shown in Figure 4.2. Then the wavefront error can be described by:[31]

$$W_k = \sum_{k,m,n,p,q} W_{2k+n+p,2m+n+q,n,p,q}(\vec{H}\cdot\vec{H})(\vec{\rho}\cdot\vec{\rho})(\vec{H}\cdot\vec{\rho})(\vec{i}\cdot\vec{H})(\vec{i}\cdot\vec{\rho}). \quad (4.6)$$

Considering just constant and linear piston, tilt, and defocus errors, the wavefront departure in the k^{th}aperture simplifies to:

$$\begin{aligned} W_k &= (W_{00000} + W_{10010}(\vec{i}\cdot\vec{H}) + W_{01001}(\vec{i}\cdot\vec{\rho}) & (4.7)\\ &\quad + W_{11100}(\vec{H}\cdot\vec{\rho}) + W_{02000}(\vec{\rho}\cdot\vec{\rho}) + W_{12010}(\vec{i}\cdot\vec{H})(\vec{\rho}\cdot\vec{\rho}))_k. & (4.8)\end{aligned}$$

Letting $(\vec{i}\cdot\vec{H}) = H\cos\phi$ and $(\vec{i}\cdot\vec{\rho}) = \rho\cos\theta$, this becomes:

$$\begin{aligned} W_k &= (W_{00000} + W_{10010}H\cos\phi + W_{01001}\rho\cos\theta & (4.9)\\ &\quad + W_{11100}H\rho\cos(\theta+\phi) + W_{02000}\rho^2 + W_{12010}H\rho^2\cos\phi)_k. \end{aligned}$$

The W_{abcde} coefficients are expressed in waves of error, at the edge of the aperture, at the maximum field angle chosen for the system. Some of the coefficients also appear in rotationally-symmetric systems. W_{02000}, for example, is just standard defocus, and W_{11100} is tilt. The rest of the forms only occur in systems with planar symmetry.

For each error discussed below, the value of the appropriate coefficient and the form of W_k will be given. Multiple errors can be summed into a single W_k, to predict the Strehl ratio of a system with multiple errors.

4.2 Piston

4.2.1 Independent of field angle

As shown in the previous chapter, piston errors cause the fringes to move away from the locations of the images. Piston errors can be calculated by measuring the optical

path length (OPL) in the system for an axial ray in each branch. Any differences in OPL are piston errors. A piston error at zero field angle just indicates that the optical path lengths of the axial rays are not equal for all branches. This can easily be corrected by design.

The mathematical description of the wavefront error in the case of constant piston must be:

$$W_k = (W_{00000})_k = (OPL_k - OPL_{reference})/\lambda \tag{4.10}$$

and the OPLs of the axial rays can usually be calculated with simple geometry. Alternatively, a single arm can be modelled in a raytrace program, and the OPL measured in that way. Modelling a single arm is often much simpler than modelling the entire system.

4.2.2 Linear with field angle - the sine condition

Unless explicitly corrected for, linear piston errors will occur in a multiple aperture system. Unless the coherence length is very long, the linear piston errors must be corrected for the system to have any significant field of view. Figure 4.3 shows the origin of linear piston errors in a multiple aperture system.[21] For an on-axis wavefront, the optical path lengths through systems A and B are equal. Both wavefronts arrive in the image plane at the same time. For a tilted wavefront, though, there is a phase delay of δ as the wavefront enters the system. After both beams have traveled an equal OPL, the beam in system B has reached the image plane, but the beam in system A has not. It is delayed by the phase δ, which must be equal to the baseline length times the field angle:

$$\delta = \Delta \cdot \alpha \tag{4.11}$$

This is a piston error that is linear as a function of the field angle.

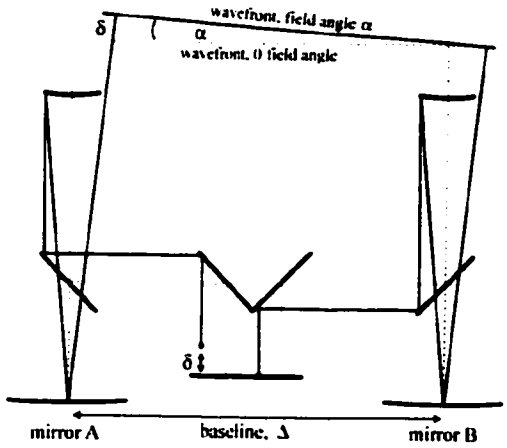

FIGURE 4.3. *The origin of linear piston error in a multiple aperture system. The off-axis wavefront has an additional pathlength on entering the system at mirror A, and does not reach the image plane at the same time as the wavefront entering at mirror B.*

For the system shown in Figure 4.3 which is not corrected for linear piston errors, the wavefront error can be estimated. The functional form of the wavefront is just

$$W_k = W_{10010} H \cos\phi = \frac{\Delta \cdot \alpha_{\max}}{\lambda} H \cos\phi \tag{4.12}$$

where Δ is the baseline length between two apertures, λ is the wavelength, and $\alpha_{\max}$ is the maximum field angle chosen for the system. (The normalized field angle H is equal to $\alpha/\alpha_{\max}$.) This says that the piston error will have the value $(\Delta \cdot \alpha_{\max}/\lambda)$ if the field angle lies in the page, as shown in Figure 4.3. If the field angle is rotated by an angle ϕ out of the page, though, the piston error will fall off by a cosine factor.

For a more general system, the maximum value of W_{10010} may not be strictly proportional to the baseline length. The OPL between axial rays would need to be calculated or measured at the maximum field angle, using a raytrace model of the k^{th} arm of the system. In that case,

$$W_k = W_{10010} H \cos\phi = \frac{1}{\lambda}(OPL_k - OPL_{reference})|_{\alpha\,\max} H \cos\phi. \tag{4.13}$$

The effect of a linear piston error on a system's image is shown in Figure 4.4. This calculation was done at a wavelength of 1 μm and a bandwidth of 0.05 μm, for a coherence length of 10 μm. A two-aperture system was used, with aperture diameters of 2.2 m and a baseline of 10 meters. The focal length was assumed to be 100 meters. The sine condition violations shown gave pathlength errors of 0, 10, and 20 μm at a field angle of 1 degree. For the system in the third row, the fringe visibility is clearly zero at the full field. Reductions in fringe visibility appear long before full field is reached. Stars in the center of the image from this system would have sharp fringes, but stars at the edge of the field would look very broad.

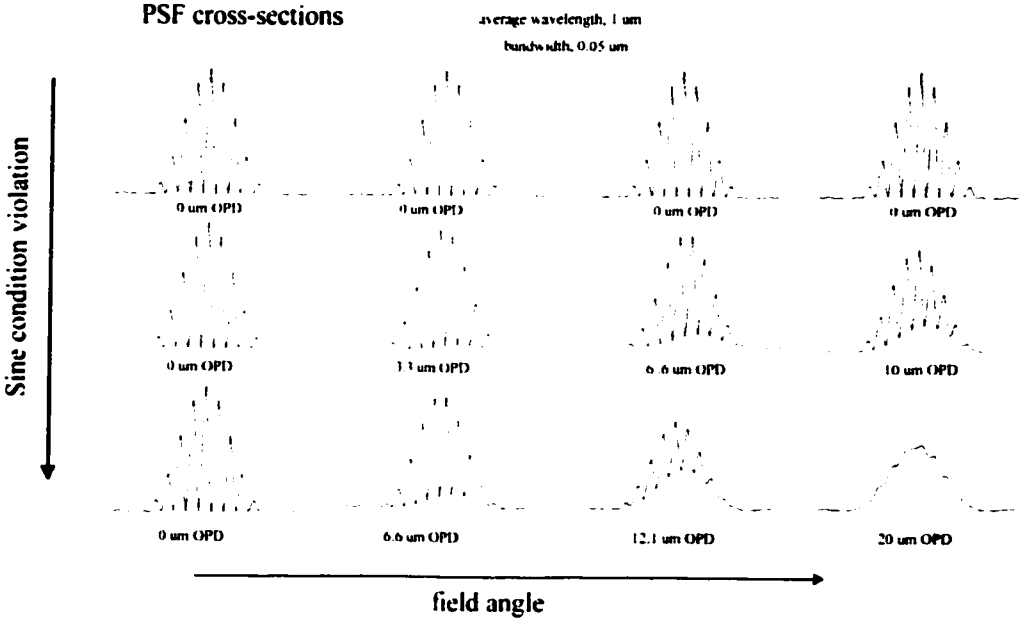

FIGURE 4.4. *The effect of a sine condition violation on an interferometric telescope's image.*

Piston errors that are linear with field angle can be corrected by satisfying the Abbe sine condition for the axial rays of the system. Consider the system in Figure 4.3 again, but now add a combining system at the former image plane, as shown in Figure 4.5. The pathlength error into the system is still $\Delta\alpha$, or more accurately,

$\Delta \sin\alpha$. Coming out of the telescope, the angle of the beam is given by the angular magnification of the telescope times the field angle, $m_t\alpha$. The separation of the beams going into the combiner is still a variable. Let the separation be some fraction of the baseline length, Δm_c. The pathlength difference between the beams going into the combiner is then: $(\Delta/m_c)\sin(m_t\alpha)$. To force the beams and fringe center to overlap, the pathlength difference going into the system should equal the pathlength difference going into the combiner. This forces the fringe center to be shifted by the same amount as the individual images. So:

$$\left(\frac{\Delta}{m_c}\right)\sin(m_t\alpha) = \Delta\sin\alpha \qquad (4.14)$$

$$m_c = \frac{\sin(m_t\alpha)}{\sin\alpha}$$

which means that the separation of the beams going into the combiner should be set to the ratio of input to output ray angles in the combining telescopes.[22]

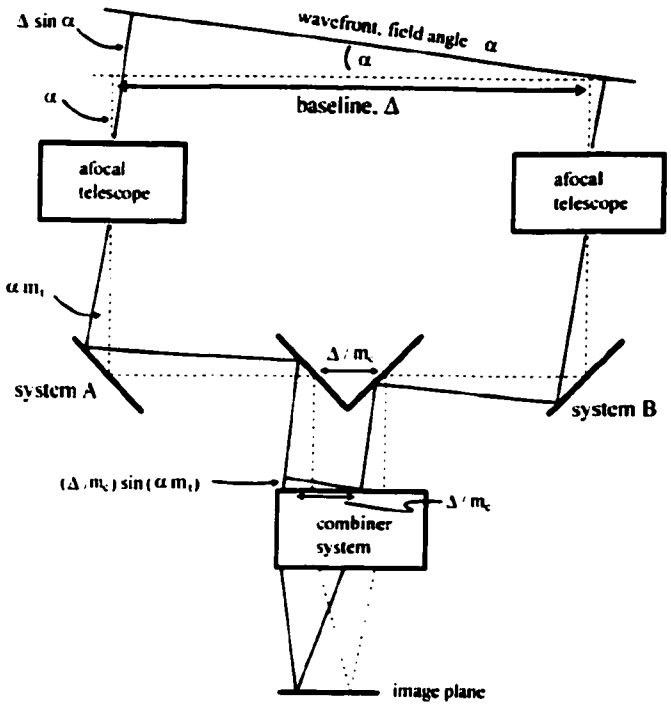

FIGURE 4.5. *Figure showing the relevant parameters for deriving the condition that satisfying the Abbe sine condition for the axial rays in a multiple aperture system eliminates linear piston errors.*

Equation 4.14 is exactly equivalent to satisfying the Abbe sine condition for the axial rays in the system. Lens designers are familiar with the Abbe sine condition as a way of eliminating coma. For a system with finite conjugates, the Abbe sine condition requires that the ratio of the input and output angles of a ray incident at angle u be equal to the magnification of the system, or

$$m = \frac{\sin u'}{\sin u}. \tag{4.15}$$

This must be satisfied everywhere in the pupil for all possible values of u.[32] This is shown in Figure 4.6.

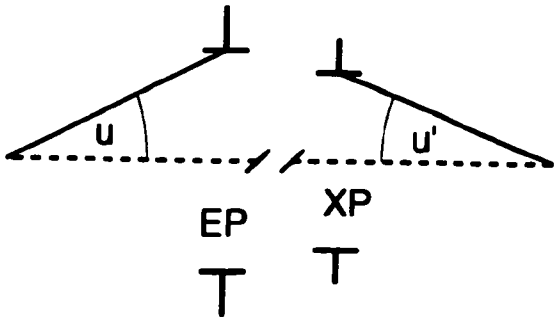

FIGURE 4.6. *The Abbe sine condition requires that sinu'/sinu = m everywhere in the pupil.*

At first glance, this coma correction method seems physically unrelated to the correction of linear piston errors. The relationship is clear, though, if the entire wavefront of a multiple aperture system is considered. Figure 4.7 shows a two aperture system. If the entire wavefront had coma (W_{131}) in it, as shown, it would appear in the two apertures only as a piston error. The rest of the wavefront isn't sampled. For one aperture, the wavefront precedes the ideal in phase, and in the other aperture, the wavefront lags behind the ideal. Since coma is linear as a function of field, the piston error between the two apertures would also increase linearly as a function of field.

Unlike traditional coma correction, then, correcting linear piston errors does not require that the sine condition be satisfied everywhere in the pupil. If the sine condition is satisfied for the axial rays at zero field in each arm, the linear piston errors will be eliminated. The sine condition in the remaining parts of the aperture will be satisfied when the individual arm is corrected for coma, and it can be ignored while working on the combining issues.

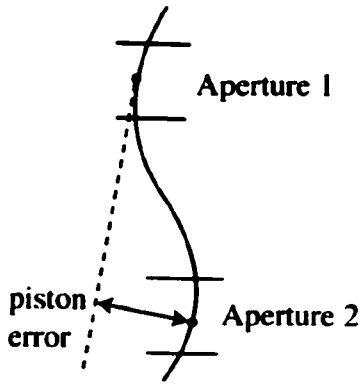

FIGURE 4.7. *Linear piston error in a multiple aperture system can be viewed as due to system coma, and thus can be eliminated by satisfying the Abbe sine condition for the centers of the apertures.*

For systems with an infinite conjugate so that $u = 0$, the Abbe sine condition has an alternate form: $h = a \cdot \sin u'$. Since $a \cdot \sin u' = h'$, this is equivalent to saying that rays anywhere in the pupil must be scaled down equally (see Figure 4.6). This can be interpreted as a requirement that the entrance and exit pupils of the system must be scaled copies of one another. For an afocal set of telescopes with a single combiner, this is even simpler: the diameters and separations of beams in image and object space must be differ only by a scaling factor. This can also be seen by making the paraxial approximation to equation 4.14, so that it becomes $m_c = m_t$, or $m_c = \frac{d_{out}}{d_{in}}$, since the angular magnification of an afocal telescope is given by the ratio of input to output beam diameters.[22]

This is a useful concept because it is so simple. It is also useful for systems that don't use afocal combiners, where it says that the aperture configuration in the exit pupil must be a scaled version of the aperture configuration in the entrance pupil. Keeping this in mind in the early design stages prevents obvious errors, like flipping one of the beams between the entrance and exit pupils. The concept is less useful when optimizing a real system, since the rays that define the edges of the apertures in the entrance and exit pupils may be out of place due to other aberrations.

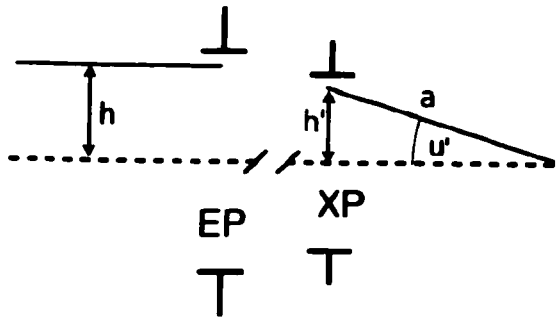

FIGURE 4.8. *The sine condition has the form $h = a \cdot \sin\theta$ for systems with an infinite conjugate.*

An optimization method that we have found useful is sketched in Figure 4.9. It relies only on axial and nearly-axial rays, which are the least likely to be aberrated in a system. Since piston errors cause the cosine fringes to move away from the individual images, we can correct the linear piston errors by demanding that the images and fringe centers stay together, to first order and for small angles. This can be done by satisfying the following condition:

$$\frac{d}{\sin\theta} = \frac{\Delta y}{\sin\alpha} \tag{4.16}$$

where the variables are defined in Figure 4.9, and α is a very small angle. The left side of the equation locates the fringe center, while the right side locates the individual images. Any additional arms of the interferometer must satisfy this same condition.

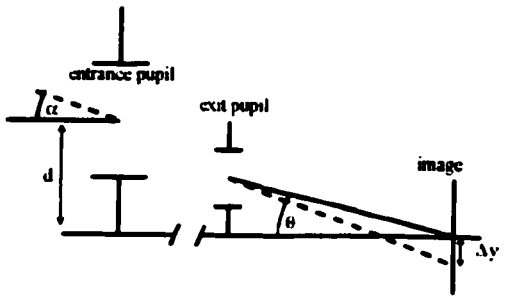

FIGURE 4.9. *The locations of the individual images and the center of the fringes must coincide for small field angles.*

This method requires tracing only an axial ray and a ray at a small angle. Such rays are the least likely to be aberrated in a real system, making this correction method ideal for use in computerized optimization routines.

4.2.3 Validity of RMS wavefront error analysis

In the case of piston errors, estimating the Strehl using the monochromatic RMS wavefront error is not valid for all pupil configurations. In particular, the Strehl estimate is invalid for very sparse two-aperture systems, and is also invalid for sparse three-aperture systems that are not in a linear configuration. To predict the performance of those two types of system, the broad-band diffraction PSF must be calculated directly.

The Strehl ratio calculated with the equation $S = e^{-(2\pi\sigma)^2}$, where σ is the RMS wavefront error of the system, will be referred to as the "RMS Strehl". It is a monochromatic calculation, and is normally valid for small values of σ.

The previous chapter shows that a piston error, δ, causes the fringes to shift out from under their amplitude envelope. For two apertures of equal diameter:

$$I(x,y) = \sum_{\lambda} A_{\lambda} \left(\frac{\pi D^2}{2}\right)^2 Somb^2\left(\frac{D}{\lambda f}\sqrt{x^2+y^2}\right) \cos^2\left(\pi\delta + \frac{\pi\Delta}{\lambda f}x\right) \qquad (4.17)$$

If the aperture diameters are quite large with respect to the system's baseline, the *Somb* envelope function is very narrow. Even in the monochromatic case, a shift of the fringes causes a drastic decrease in the amplitude of the fringes and in the amplitude of the combined image. Then the monochromatic PSF is a good approximation of the polychromatic PSF. Then, the RMS Strehl is valid.

This effect is shown in Figure 4.10, for two rectangular apertures with increasing amounts of relative piston errors. The calculations were done for an average wavelength of 1 μm and a bandwidth of 10%, giving a coherence length of roughly 10 μm. The system has a fill factor of approximately 1, and the polychromatic and monochromatic Strehls are identical for pistons less than 1 μm. Then, the RMS Strehl shows good agreement for piston errors under 0.5 μm, or 1/2 wave.

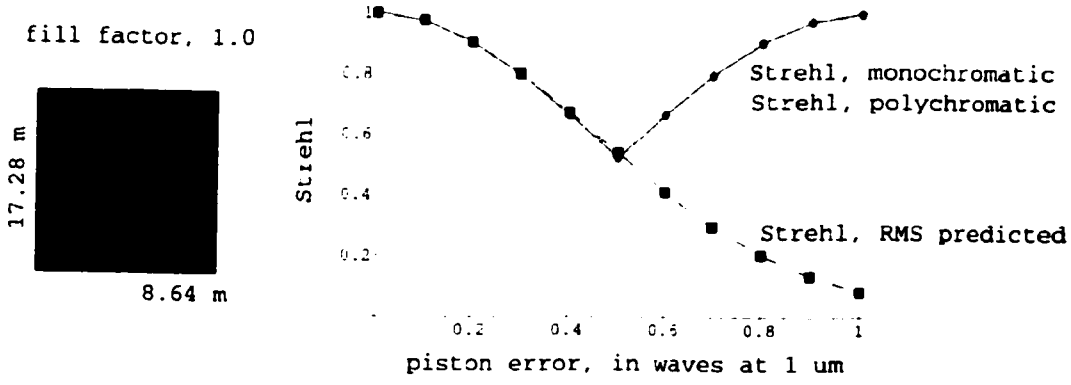

FIGURE 4.10. *A two aperture system with a fill factor of 1 shows that the monochromatic Strehl is a good approximation of the polychromatic Strehl. The Strehl estimated from the monochromatic RMS wavefront error is in good agreement for piston less than 1/2 wave.*

On the other hand, if the apertures are very small ($D \approx 0$) then the *Somb* envelope function is almost infinitely wide, and effectively has a constant amplitude. The shift of the cosine fringes under this constant does not affect the height of the fringes or the height of the combined image. In the monochromatic case, very large piston errors can be present, and the height of the fringes will be unchanged even though

the RMS wavefront error may be very large. In the broadband case, the height of the fringes will also be unchanged due to the *Somb* envelope function. But, each set of monochromatic fringes shifts by a slightly different amount, since $\delta = d/\lambda$ where d is the real length of the piston error. These relative shifts cause the broadband fringes to lose visibility as a function of the spectral width. Then, the monochromatic PSF (which predicts perfect Strehls for any amount of piston error) is not a good estimate of the polychromatic PSF (which deteriorates depending on the spectral width). The broadband image deterioration is completely unrelated to the monochromatic RMS wavefront error. Instead, the performance of the system will be very good for any amount of piston error less than a coherence length.

This situation is shown in Figure 4.11. The calculations were done for an average wavelength of 1 μm and a bandwidth of 10%, giving a coherence length of roughly 10 μm. The system has a fill factor of approximately 0. The RMS Strehl does not agree with the real Strehl ratios of the system for any amount of piston error. As expected, the bottom figure shows that the polychromatic Strehl is not in good agreement with the monochromatic Strehl for piston errors above 1/2 μm.

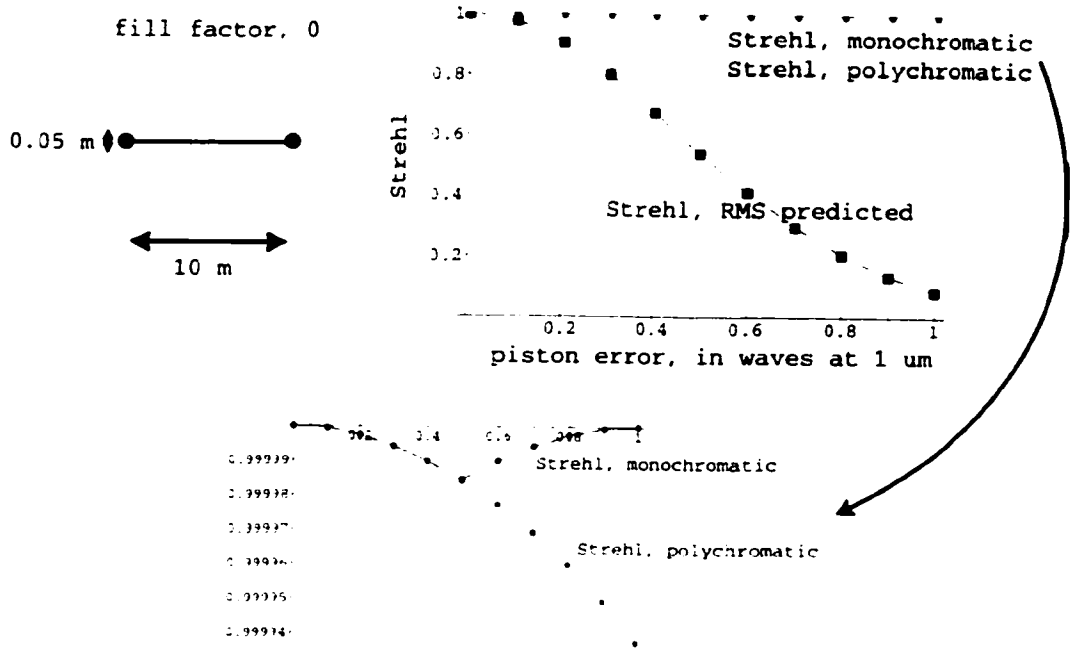

FIGURE 4.11. *In the case of the sparse two-aperture system, the monochromatic RMS wavefront error does not correctly predict the system performance, for any amount of piston error.*

The difference between these two systems can also be understood by looking at the wavefront errors in the pupil. The two systems and their wave fans are shown in Figure 4.12. For a sparse two-aperture system, a piston error in one aperture produces a system wave fan that contains only tilt. The monochromatic image is shifted, but does not deteriorate with increasing amounts of piston. For the filled system, though, the piston error produces a fairly complicated system wave fan. The error shown will clearly degrade the combined, monochromatic image. Looking more closely, if the tilt error in the filled wavefront is removed, the fringes will be located at the center of the image plane. But there will be equal amounts of tilt remaining in each aperture, indicating that the images from each aperture have together moved away from the fringe center.

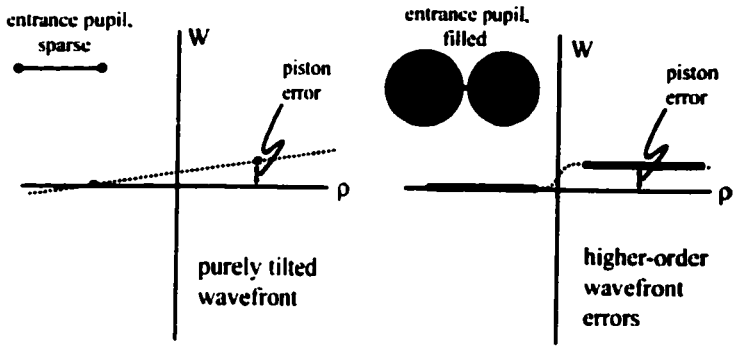

FIGURE 4.12. *For a sparse two-aperture system, a piston error produces a wavefront with pure tilt. The image is shifted but is still perfect. For a filled two-aperture system, a piston error produces a complicated wavefront that will cause the image to deteriorate.*

This argument also holds for the three-aperture system. In the case of the sparse system, piston errors in each aperture just define a tilted wavefront. The image shifts but does not deteriorate with increasing piston errors. Then, the monochromatic RMS wavefront error does not predict the Strehl of the system accurately. The polychromatic Strehl must be calculated with diffraction analysis, or it can be assumed to be perfect for piston errors much less than the coherence length of the system. For the filled three-aperture system, like the filled two-aperture system, the wavefront with piston errors is complicated. The image degrades with increasing amounts of piston error. In that case, the RMS Strehl is correct. These two situations are shown in Figure 4.13.

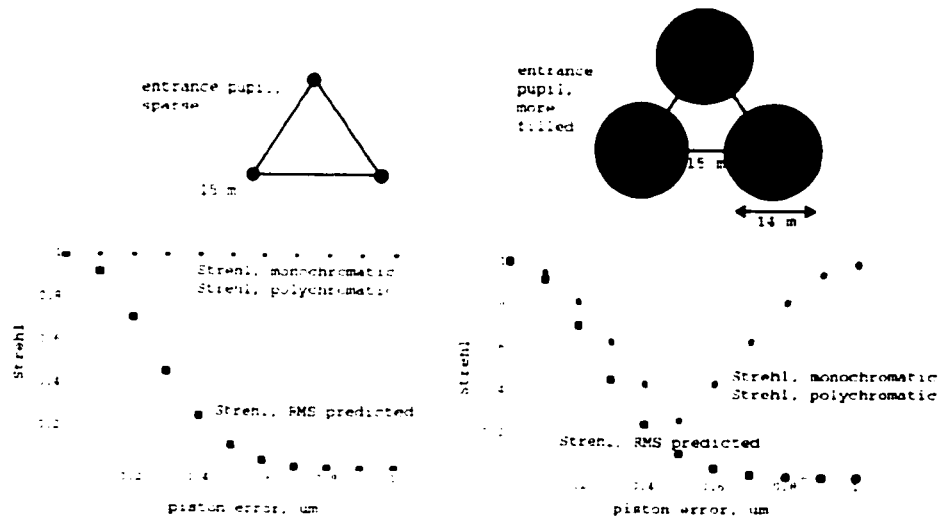

FIGURE 4.13. *The performance of a sparse 3-aperture system is not correctly predicted by the RMS Strehl. The performance of a more filled system is correctly predicted by the RMS Strehl, for piston errors less than about 1/2 wave.*

If the three-aperture system happens to have a linear configuration, though, the wavefront with piston errors cannot be approximated with a purely tilted wavefront, even if the system is very small. For the three-aperture linear configuration, then, the RMS wavefront error does accurately predict the Strehl ratio, for any fill factor. This is shown in Figure 4.14.

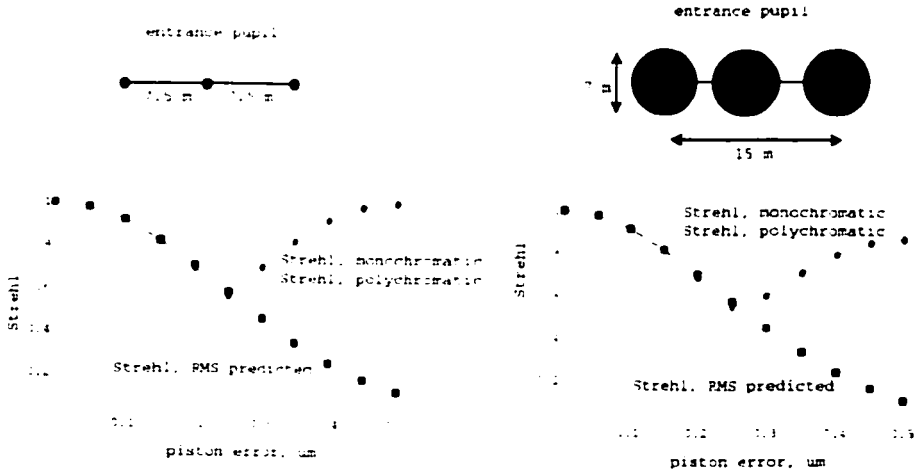

FIGURE 4.14. *If the 3-aperture system has a linear configuration, the RMS Strehl predicts the correct performance for any fill factor, for piston errors less than 1/2 wave.*

There is an interesting transition region between the cases of completely sparse and completely filled. Two and three-aperture systems that fall in this regime may be approximated adequately by the RMS Strehl for very small amounts of piston. The true Strehls and the RMS Strehl are shown in Figure 4.15 for a two-aperture system with a fill factor of 0.47.

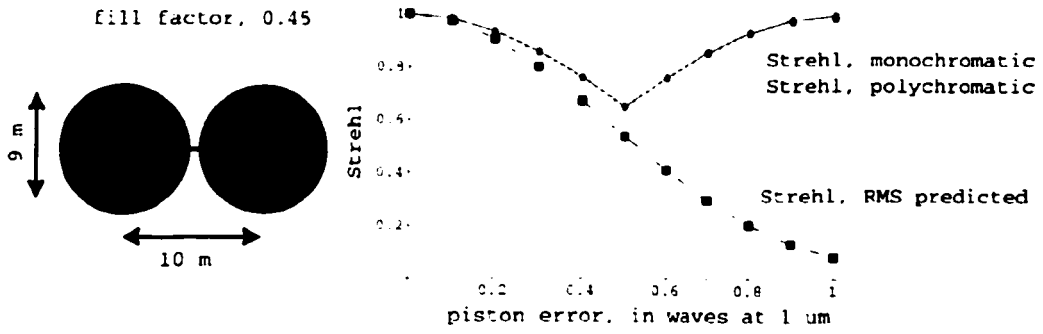

FIGURE 4.15. *There is a transition region between the sparse and filled two-aperture cases. This data shows that the Strehl for a fill factor of 0.47 is accurate for about 1/10 wave of piston error.*

In summary, two-aperture and nonlinear three-aperture systems with high fill factors have performance that is correctly predicted by the RMS Strehl, for piston errors out to about 1/2 wave. As the fill factor drops to 1/2, the region of validity for the RMS Strehl drops to about 1/10 wave of piston error. For fill factors under 1/2, the true polychromatic Strehl must be calculated with diffraction analysis. For very low fill factors, it is safe to assume that the performance of the system will be good for piston errors smaller than the coherence length of the system.

For all other pupil configurations, the RMS Strehl is accurate to about 1/2 wave of piston error.

4.3 Tilt

4.3.1 Independent of field angle

Constant tilt is caused by a pointing error in one of the branches of the system. The images don't overlap in the image plane, even for zero field angle. This just sets the pointing of the telescope, or the final angle of the axial ray out of the system. Current interferometers use active control to maintain the pointing, since wind and thermal effects can cause pointing errors as a function of time.

If an image is separated from its correct position at zero field angle by a distance β, then the resulting tilt error in the wave fan will be:

$$W_{01001} = \frac{2}{D\lambda} \tan\left[\arctan\left(\frac{\Delta/2+\beta}{f}\right) - \arctan\left(\frac{\Delta}{2f}\right)\right] \tag{4.18}$$

where D is the aperture diameter, λ is the wavelength, f is the system focal length, and $\Delta/2$ is the height of the aperture from the normal to the center of the image plane.

The functional form of the constant tilt error is then:

$$W_k = \frac{2}{D\lambda} \tan\left[\arctan\left(\frac{\Delta/2+\beta}{f}\right) - \arctan\left(\frac{\Delta}{2f}\right)\right] \rho\cos\theta \tag{4.19}$$

The $\cos\theta$ term is present because the tilt is in the direction of the displaced image.

4.3.2 Linear with field angle

Tilt errors that are linear as a function of field can be corrected by matching the focal lengths in each branch, provided the focal planes can still be made to overlap. This is shown in Figure 4.16. If the field angle is α, then to first order each image moves up its own image plane by $\alpha \cdot f$. If the focal lengths do not match, the images will separate by $(f_1 - f_2) \cdot \alpha$. If $f_1 = f_2$, there will be no linear tilt errors.

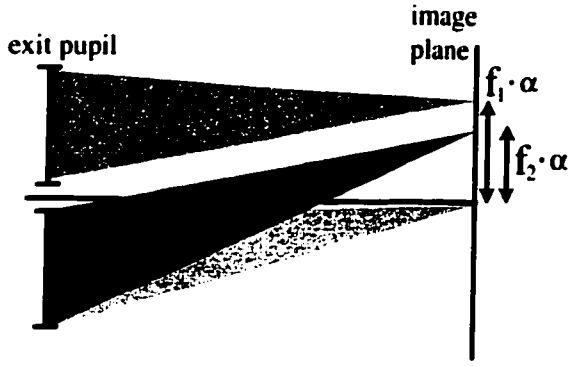

FIGURE 4.16. *If the focal lengths of the branches don't match, the images separate in the focal plane linearly with field angle.*

The image separation can be calculated and converted to a tilt error. For two interferometer arms with mismatched focal lengths and overlapping image planes, the maximum distance of separation between the focal points in the system image plane must be:

$$(f_2 - f_1) \cdot \alpha_{\max} \tag{4.20}$$

where $\alpha_{\max}$ is the maximum field angle chosen for the system and f_1 and f_2 are the effective focal lengths of two arms. If we assume that all of this distance is due to a tilt error in one of the arms and think of the other arm as correct, then the magnitude of the tilt wavefront error in waves at the edge of the pupil in waves can be calculated as:

$$W_{11100} = \frac{D \cdot \alpha_{\max}}{2 \cdot \lambda} \frac{f_2 - f_1}{f_1} \tag{4.21}$$

where D is the aperture diameter and λ is the wavelength. This gives a wavefront error functional form of:

$$W_k = W_{11100} \cdot H\rho\cos(\theta+\phi) = \frac{D \cdot \alpha_{\max}}{2 \cdot \lambda}\frac{f_2 - f_1}{f_1}H\rho\cos(\theta+\phi). \tag{4.22}$$

4.4 Power

4.4.1 Independent of field angle

Each branch in a multiple aperture system can have its own, unique image plane. Because of this, any two image planes may be displaced or tilted with respect to another. Power errors independent of field angle indicate that the power or positions of one of the elements has been chosen incorrectly, causing a constant displacement of the affected image plane. The images at zero field angle are separated in space longitudinally, so that one beam is defocussed in the image plane chosen as the system's image plane. The distance between the images at zero field angle, ε_z, can be calculated paraxially using standard methods. This distance can then be converted to a wavefront error by using:

$$W_{02000} = \frac{\varepsilon_z}{8(f/\#)^2 \cdot \lambda} \tag{4.23}$$

where ε_z is the distance between the zero-field-angle images, λ is the wavelength, and $(f/\#)$ is the f-number of the branch rather than of the entire system.[33] The wavefront error has the form:

$$W_k = \frac{\varepsilon_z}{8(f/\#)^2 \cdot \lambda} \cdot \rho^2 \tag{4.24}$$

where D is the aperture diameter.

4.4.2 Linear with field angle

The individual image planes in a multiple aperture system may also be tilted with respect to one another. If one of the image planes is selected as the system image plane, then the remaining beam will be defocussed in the system image plane, as shown in Figure 4.17. The defocus distance will increase linearly as a function of field.

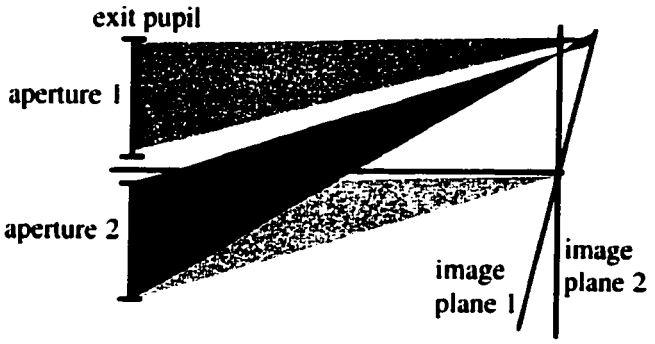

FIGURE 4.17. *Image planes that are tilted with respect to one another will produce a defocus error that is linear with field angle.*

For a tilt between two image planes of γ, the maximum distance between the defocussed spot and the system's image plane will be $\varepsilon_z \approx f \cdot \gamma \cdot \alpha_{\max}$, where $\alpha_{\max}$ is the maximum field angle chosen for the system, γ is the angle between the system and tilted image planes, and f is the system focal length. The wavefront coefficient will have the form:

$$W_k = W_{12010} H \rho^2 \cos\phi = \frac{f \cdot \gamma \cdot \alpha_{\max}}{8(f/\#)^2 \cdot \lambda} \cdot H \rho^2 \cos\phi. \tag{4.25}$$

In a system with planar symmetry, it is not possible to produce tilt in any direction except about an axis perpendicular to the plane of symmetry. Then the defocus error will be maximum for field angles such that the chief ray lies in the plane of symmetry.

The $\cos\phi$ term is 1 if this is the case. For field angles not in the plane of symmetry, the linear defocus error will be reduced in magnitude.

Calculating the orientation of the image plane in a system with tilted and decentered optics is not covered in introductory geometric optics textbooks, but it is needed to calculate the parameter γ, which is the tilt between image planes of the individual branch and the system. The orientation of the image plane for any system can be calculated using the Scheimpflug condition.[34] This condition states that the object and image planes must intersect over the principle planes of the system, as shown in Figure 4.18. If a ray that lies in the object plane is traced, the ray in image space must lie in the image plane. For a single element, then, a simple raytrace equation gives the image plane tilt, u', for a given object:

$$n' \tan u' = n \tan u - (y_o + z \tan u)\phi \tag{4.26}$$

where ϕ is the element's power, and y_o is the height of the ray at the object plane, z is the distance from the object to the element, and u is the tilt of the object plane measured from the axial ray. Light travelling from left to right has $n = 1$, and light travelling from right to left has an index of $n = -1$. All distances are measured from the optical element being considered, so any distance to the left of the mirror is negative and any distance to the right is positive. Any distance above the axial ray is positive, and any below is negative. All concave mirrors have positive powers.

Equation 4.26 can be applied in series, with the image from one element becoming the object for the following element, with the appropriate decenters and tilt angles.

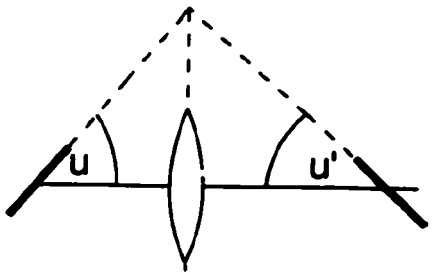

FIGURE 4.18. *The Scheimpflug condition states that the object and image plane must intersect in the system's principle planes. The image plane's tilt can be calculated by tracing a ray in the object plane. The ray must also lie in the image plane.*

In a multiple aperture system, some of the optical elements may be encountered at an angle by the axial ray (at zero field angle). The paraxial raytrace above is still useful, but all distances z must be measured along the axial ray of the system. In addition, "oblique power" must be substituted for the paraxial power of any element that the axial ray encounters at an angle.[35] The corresponding "oblique focal length" is the distance along the axial ray from the optical surface to the subsequent image. In Figure 4.19, the mirror appears to be foreshortened to the fan of rays along the y-axis. The oblique power will then be: $\phi_{OB} = \phi/\cos\theta$. Since $\cos\theta$ must be less than one, the oblique power will be larger than the paraxial power of the element. The image will be formed at a distance less than f along the axial ray. For a fan of rays along the x-axis, though, the oblique power will be: $\phi_{OB} = \phi \cdot \cos\theta$. The image will be formed at a distance greater than f, along the axial ray. In particular, it will be formed at a distance of $f/\cos\theta$, which is exactly the distance along the axial ray required to place the image in the paraxial focal plane.

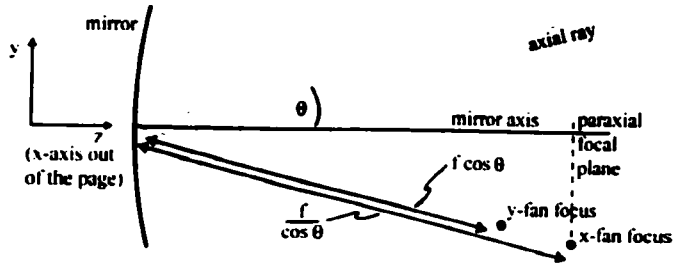

FIGURE 4.19. *The oblique power of an optic is larger than its paraxial power.*

Certain designs will not have tilted image planes. A system of afocal telescopes that share a single combiner will not suffer from image plane tilt problems. All mirrors are axially symmetric, and the image plane orientation is always either perfectly horizontal or vertical as it passes through the fold flats to the combiner. Any afocal beam entering the combiner will be directed onto the combiner's image plane. Also, a system that is a derivative of an axially-symmetric system will not have relative tilt errors between the branches. These system types are sketched in Figure 4.20.

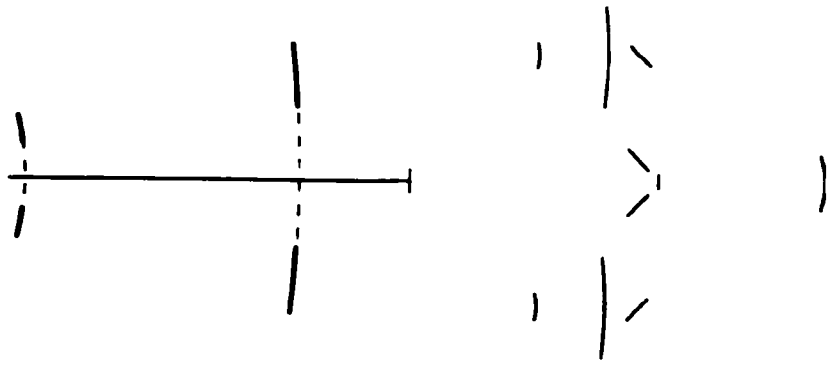

FIGURE 4.20. *Two systems that have no relative tilts between their image planes.*

In a more general system that mixes axially-symmetric and off-axis optics, an off-axis mirror can be used to correct for the tilt of the image planes. If the error must be tolerated, then it can usually be minimized by bringing the individual beams

together at as shallow an angle as possible.

4.5 An example system

As an example, consider a two aperture system. The performance can be predicted for any of the errors discussed above. Each aperture has diameter D and the baseline length is Δ. The maximum field angle will be chosen to be $\alpha_{\max} = 1/2$ arcmin. Consider aperture 1 as "correct" and aperture 2 as having aberrations.

Suppose that the axial pathlengths in the two arms at zero field angle do not match. This is a constant piston error. Let OPL_1 and OPL_2 be the axial pathlengths in the two arms. Then the RMS wavefront error and Strehl ratio as a function of field angle can be calculated using equations 4.1 to 4.5:

$$\begin{aligned} W_1 &= 0 \text{ and } W_2 = (OPL_1 - OPL_2)/\lambda \\ \langle W_1 \rangle &= 0 \text{ and } \langle W_2 \rangle = (OPL_1 - OPL_2)/\lambda \\ \langle W \rangle &= \frac{1}{2}\frac{(OPL_1 - OPL_2)}{\lambda} \\ \sigma_1^2 &= \sigma_2^2 = \frac{1}{4}\frac{(OPL_1 - OPL_2)^2}{\lambda^2} \\ \sigma &= \frac{1}{2}\frac{(OPL_1 - OPL_2)}{\lambda} \end{aligned} \tag{4.27}$$

If there is a linear piston error between the apertures:

$$W_1 = 0 \text{ and } W_2 = \frac{1}{\lambda}(OPL_1 - OPL_2)|_{\alpha\,\max} H \cos\phi \tag{4.28}$$

$$\sigma = \frac{1}{2}\frac{(OPL_1 - OPL_2)|_{\alpha\,\max}}{\lambda} H \cos\phi \tag{4.29}$$

and the RMS wavefront error will vary depending on the field angle chosen. It will have a maximum when the field angle lies in the plane of symmetry and has the magnitude $\alpha_{\max}$, so that $H = 1$ and $\cos\phi = 1$.

If there is a constant tilt error in the second aperture so that a paraxial raytrace of chief rays gives an image separation of β, then the RMS wavefront error calculation

will go as follows:

$$\begin{aligned}
W_1 &= 0 \\
W_2 &= \frac{2}{D\lambda} Tan\left(ArcTan\left(\frac{\Delta/2+\beta}{f}\right) - ArcTan\left(\frac{\Delta}{2f}\right)\right)\rho\cos\theta \\
\langle W_1\rangle &= \langle W_2\rangle = \langle W\rangle = 0 \text{ and } \sigma_1^2 = 0 \\
\sigma_2^2 &= \frac{1}{D^2\lambda^2} Tan^2\left(ArcTan\left(\frac{\Delta/2+\beta}{f}\right) - ArcTan\left(\frac{\Delta}{2f}\right)\right) \\
\sigma &= \frac{1}{\sqrt{2}D\lambda} Tan\left(ArcTan\left(\frac{\Delta/2+\beta}{f}\right) - ArcTan\left(\frac{\Delta}{2f}\right)\right)
\end{aligned} \tag{4.30}$$

A linear tilt error due to the fact that the focal lengths of each arm don't match will give an RMS wavefront error of:

$$\begin{aligned}
W_1 &= 0 \text{ and } W_2 = \frac{D\alpha_{\max}}{2\lambda}\frac{f_2 - f_1}{f_1} H\rho\cos(\theta+\phi) \\
\sigma &= \frac{D\alpha_{\max}}{4\sqrt{2}\lambda}\frac{f_2 - f_1}{f_1} H
\end{aligned} \tag{4.31}$$

where f_1 and f_2 are the focal lengths of the two branches, respectively. Notice that the RMS wavefront error is the same for all orientations of H. This is expected, since a mismatch in focal lengths will produce the same amount of image separation in any direction of field angle.

A constant defocus error indicates that the focal planes for each branch are offset by a constant distance. The RMS wavefront error if the image planes of the two-aperture system are displaced by ε_z will be:

$$\begin{aligned}
W_1 &= 0 \text{ and } W_2 = \frac{D^2\varepsilon_z}{8f^2\lambda}\rho^2 \\
\langle W_1\rangle &= 0 \text{ and } \langle W_2\rangle = \frac{D^2\varepsilon_z}{16f^2\lambda} \\
\langle W\rangle &= \frac{D^2\varepsilon_z}{32f^2\lambda} \\
\sigma_1^2 &= \frac{D^4\varepsilon_z^2}{1024f^4\lambda^2}, \sigma_2^2 = \frac{7D^4\varepsilon_z^2}{3072f^4\lambda^2} \\
\sigma &= \frac{1}{32}\sqrt{\frac{5}{3}}\frac{D^2\varepsilon_z}{f^2\lambda}
\end{aligned} \tag{4.32}$$

A linear defocus error, due to a relative focal plane tilt of γ, gives an RMS wavefront error of:

$$\begin{aligned} W_1 &= 0 \text{ and } W_2 = \frac{f\gamma\alpha_{\max}}{8(f/D)^2\lambda} H\rho^2 \cos\phi \\ \sigma &= \frac{1}{32}\sqrt{\frac{5}{3}}\frac{D^2\gamma\alpha_{\max}}{f\lambda} H\cos\phi \end{aligned} \tag{4.33}$$

Of course, a system will generally suffer from multiple aberrations. Suppose that the two aperture system has been corrected for constant piston, constant tilt, and constant defocus. The focal lengths of the two arms don't match, the image planes are tilted with respect to one another, and the sine condition is not satisfied, so linear piston errors occur. This is exactly the situation shown in the wave fans in Figure 4.1, for a three-aperture system. The wavefront error for the two aperture system, if the first aperture is defined as correct, will be given by the sum of the individual errors:

$$\begin{aligned} W_2 &= \frac{1}{\lambda}(OPL_k - OPL_{reference})|_{\alpha\max} H\cos\phi \\ &+ \frac{D\cdot\alpha_{\max}}{2\cdot\lambda}\frac{f_2 - f_1}{f_1} H\rho\cos(\theta+\phi) + \frac{f\gamma\alpha_{\max}}{8(f/D)^2\lambda} H\rho^2\cos\phi \end{aligned} \tag{4.34}$$

and the calculation of RMS wavefront error can proceed as usual.

Figure 4.21 shows the Strehl ratios calculated with equation 4.5 for a two aperture system with 10 meter aperture diameters, a 10 meter baseline, a focal length of 50 meters, and a wavelength of 1 μm. The Strehl as a function of field angle is shown for each wavefront error individually, and it is then shown for all the wavefront errors combined.

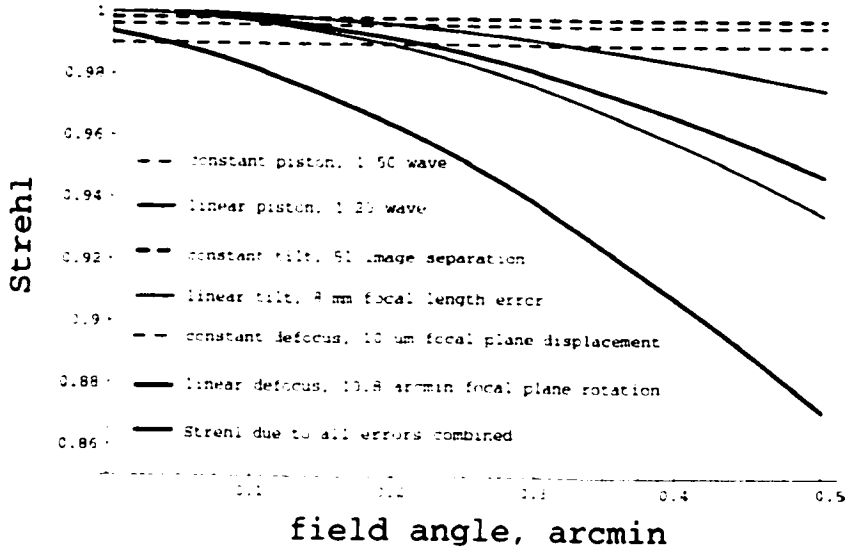

FIGURE 4.21. *The Strehl ratio for a two aperture system, with low-order beam combining errors.*

4.6 Conclusions

The table below summarizes the results of this chapter. Each type of beam combining error has a different effect on the system's image. Piston errors cause a decrease in the coherence of the combining. Tilt errors cause the individual images from each branch to separate. Defocus errors cause the images to separate longitudinally away from the image plane.

Each error can be represented as a wavefront error, with the proper dependence on pupil coordinate and field angle. The RMS wavefront error of the systems can be calculated, and then the Strehl of the system predicted as a function of field angle. This gives a good way to estimate the system's performance, without needing a complete, interferometric raytrace model, which can be time-consuming to develop.

In certain cases, the Strehl predicted with equation 4.5 may be inaccurate. If the wave fans as a function of field angle show predominantly piston error, and the system configuration is either a sparse two aperture or nonlinear three aperture system, then

the Strehl should be calculated with a full polychromatic diffraction calculation of the system's PSF.

Methods of correcting each error were given. To prevent constant piston, the axial pathlengths in all branches of the system should match. To prevent linear piston errors, the Abbe sine condition must be satisfied for all the axial rays in the system. Constant tilt is caused by a pointing error in the telescope, and can be controlled by the position and orientation of the elements in the system. Linear tilt errors are caused by mismatched focal lengths between the arms. Constant defocus errors are caused by power errors in the arms, resulting in a mispositioning of the on-axis images. Linear defocus is caused by individual image planes that are tilted with respect to one another. The image plane tilts can be calculated using the Scheimpflug condition, and corrected by design.

PISTON errors:	
effect:	reduction in coherence
constant error:	$W_{00000}=\frac{1}{\lambda}(OPL_k-OPL_{ref})\|_{\alpha=0}$
linear error:	$W_{10010}H\cos\phi=\frac{1}{\lambda}(OPL_k-OPL_{ref})\|_{\alpha_{max}}H\cos\phi$
to correct constant:	match axial pathlengths
to correct linear:	satisfy sine cond. for all axial rays
TILT errors:	to correct:
effect:	images from each aperture separate laterally
constant error:	$W_{01001}\rho\cos\theta=\frac{2}{D\lambda}\tan\left\|\arctan\left(\frac{\Delta/2+\beta}{f}\right)-\arctan\left(\frac{\Delta}{2f}\right)\right\|\rho\cos\theta$
linear error:	$W_{11100}H\rho\cos\theta=\frac{D\alpha_{max}}{2\lambda}\frac{f_2-f_1}{f_1}H\rho\cos\theta$
to correct constant:	set correct telescope pointing in all arms
to correct linear:	match focal lengths in all arms
DEFOCUS errors:	to correct:
effect:	images from each aperture separate longitudinally
constant error:	$W_{02000}\rho^2=\frac{D^2\epsilon_z}{8f^2\lambda}\rho^2$
linear error:	$W_{12010}H\rho^2\cos\phi=\frac{f\gamma\alpha_{max}}{8(f/D)^2\lambda}H\rho^2\cos\phi$
to correct constant:	set correct powers in each arm
to correct linear:	force focal plane tilts to be equal

TABLE 4.1. *Effects on the system performance and correction methods for the low-order combining errors.*

Chapter 5

PLANE-SYMMETRIC ABERRATION THEORY IN WIDE-FIELD BEAM COMBINING

As discussed in Chapter 4, the branches of a multiple aperture system usually have a single plane of symmetry. These systems must be treated with a larger set of aberrations than the standard rotationally-symmetric aberrations. Section 4.1 investigates the higher order aberrations that can occur in plane-symmetric systems. Section 4.2 uses plane-symmetric aberration theory to more rigorously derive the design rules discussed in Chapter 4, and to derive higher-order design rules for wide-field multiple aperture systems.

5.1 Correction of higher-order aberrations

Often, the branches of a multiple aperture system will have only one plane of symmetry. The aberrations in these systems are also only required to have planar symmetry, so the set of possible plane-symmetric aberrations is much larger than the set of standard, rotationally symmetric aberrations.

The set of aberrations (to third order) that can occur in a system with planar symmetry is shown in Table 5.1.[31] $\vec{H}$ is the normalized field angle, $\vec{\rho}$ is the normalized pupil coordinate, and the vector $\vec{i}$ lies in the plane of symmetry of the system (see Figure 5.1).

aberration form	description
W_{00000}	piston error, constant with field angle
$W_{10010}(\vec{i}\cdot\vec{H})$	linear piston error
$W_{01001}(\vec{i}\cdot\vec{\rho})$	tilt in the plane of symmetry, constant with field
$W_{11100}(\vec{H}\cdot\vec{\rho})$	tilt, linear with field
$W_{02000}(\vec{\rho}\cdot\vec{\rho})$	defocus, constant with field
$W_{12010}(\vec{i}\cdot\vec{H})(\vec{\rho}\cdot\vec{\rho})$	defocus, linear with field
$W_{20000}(\vec{H}\cdot\vec{H})$	quadratic piston, any direction of field
$W_{02002}(\vec{i}\cdot\vec{\rho})^2$	constant astigmatism
$W_{11011}(\vec{i}\cdot\vec{H})(\vec{i}\cdot\vec{\rho})$	anamorphism
$W_{20020}(\vec{i}\cdot\vec{H})^2$	quadratic piston, field angles in the plane of symmetry
$W_{03001}(\vec{i}\cdot\vec{\rho})(\vec{\rho}\cdot\vec{\rho})$	constant coma
$W_{12101}(\vec{i}\cdot\vec{\rho})(\vec{H}\cdot\vec{\rho})$	linear astigmatism
$W_{21001}(\vec{i}\cdot\vec{\rho})(\vec{H}\cdot\vec{H})$	quadratic distortion, any direction of field
$W_{21110}(\vec{i}\cdot\vec{H})(\vec{H}\cdot\vec{\rho})$	quadratic distortion, field angles in the plane of symmetry
$W_{30010}(\vec{i}\cdot\vec{H})(\vec{H}\cdot\vec{H})$	cubic piston
$W_{04000}(\vec{\rho}\cdot\vec{\rho})^2$	spherical
$W_{13100}(\vec{H}\cdot\vec{\rho})(\vec{\rho}\cdot\vec{\rho})$	linear coma
$W_{22200}(\vec{H}\cdot\vec{\rho})^2$	quadratic astigmatism
$W_{22000}(\vec{H}\cdot\vec{H})(\vec{\rho}\cdot\vec{\rho})$	field curvature
$W_{31100}(\vec{H}\cdot\vec{H})(\vec{H}\cdot\vec{\rho})$	distortion
$W_{40000}(\vec{H}\cdot\vec{H})^2$	quartic piston

TABLE 5.1. *Aberrations, to third order, that can occur in a systems with a single plane of symmetry.*

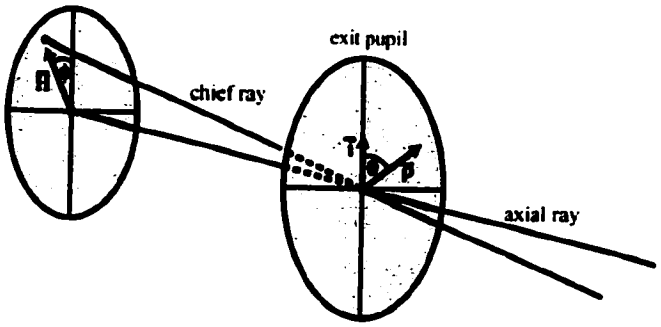

FIGURE 5.1. *Definitions of the field vector, H, and the pupil coordinate, ρ. The vector i lies at the intersection of the plane of symmetry with the entrance pupil.*

As discussed in Chapter 4, the physical origins of the first six of these aberrations are known. Constant piston error, W_{00000}, occurs when the axial pathlengths in the system aren't equal. Linear piston error, W_{10010}, occurs when the Abbe sine condition is violated for the axial rays in the system. Constant tilt errors, W_{01001}, occur due to pointing errors in the telescope and can be corrected by tilting an optic in the system. Linear tilt errors, W_{11100}, occur when the focal lengths of each branch aren't equal. Constant defocus, W_{02000}, occurs if a branch's image plane is displaced from the system's image plane. Linear defocus, W_{12010}, occurs when the branch's image plane is tilted with respect to the system's image plane.

Some of these aberrations will reduce the quality of the image produced by the branch and cannot be tolerated. Their presence will always degrade the quality of the combined image. These include the astigmatisms, coma, and spherical aberrations. Other aberration terms will only move the image. These include the piston terms, distortion terms, and the field curvature terms. These aberrations may be tolerable in a branch of a multiple aperture system, if the conditions for beam combining can still be satisfied. For example, a two-aperture system with equal amounts of quadratic piston, W_{20000}, would still have coherent combining everywhere in the image plane. It is the differences in pistons and image positions that lead to the beam combining errors, not their absolute magnitudes.

5.1.1 Higher-order tilt errors

As discussed in Chapter 4, constant and linear tilt errors are due to pointing errors and mismatched focal lengths in a system. As Table 5.1 shows, tilt errors that are both quadratic (W_{21001}, W_{21110}) and cubic (W_{31100}) with tilt error can also occur in a plane-symmetric system. A system composed of plane-symmetric branches can have image separations that are quadratic and cubic with field angle, then.

In certain situations, distortion errors may be allowed in multiple aperture systems. Consider the rotationally symmetric, distorted image plane shown in Figure 5.2. Equal amounts of rotationally symmetric distortion (W_{31100}) might be possible in a two-aperture system with identical but mirror-image branches, since the images would still overlap for positive and negative field angles. The images would not necessarily combine coherently, however. A modification to the Abbe sine condition could eliminate the linear piston errors at the new, distorted image points. The distortion in the otherwise perfect image could be eliminated in post-processing.

If the constraint of rotational symmetry is relaxed to planar symmetry, though, the image plane can have any form that is symmetric about the plane of symmetry. The field circled in red in Figure 5.2 is one potential form for plane-symmetric distortion (assuming the image position variations are quadratic with field angle, not cubic). In that case, the distortion in two identical branches operating as a multiple aperture system would generally be equal in magnitude, but opposite in sign. This would result in the image plane for a two-aperture system shown in Figure 5.3, which has large amounts of image separation. We have been referring to this problem as "differential distortion", since it is the difference between the distortions in the two arms that leads to the image separations.

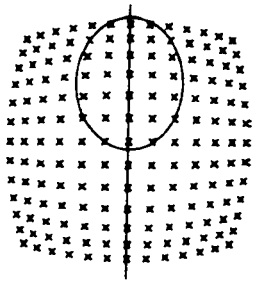

FIGURE 5.2. *Rotationally-symmetric barrel distortion. The field circled in red shows one possible type of plane-symmetric distortion, which needs only to have symmetry about a single axis.*

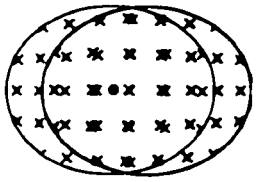

FIGURE 5.3. *Differential distortion in the image plane of a two-aperture system, caused by distortion that is not symmetric.*

5.1.2 Higher-order power errors

Constant and linear power errors have been discussed in Chapter 4. Quadratic defocus, or field curvature, appears in both rotationally symmetric and plane-symmetric systems. Figure 5.4 shows the physical origin of quadratic power errors between two apertures. If the magnitudes of the field curvature aberrations in each arm are equal, this error is eliminated. Again, the image overlap longitudinally in space, but will not necessarily combine coherently. Relative piston errors on the curved image surface would have to be eliminated for the combined image to be high in quality.

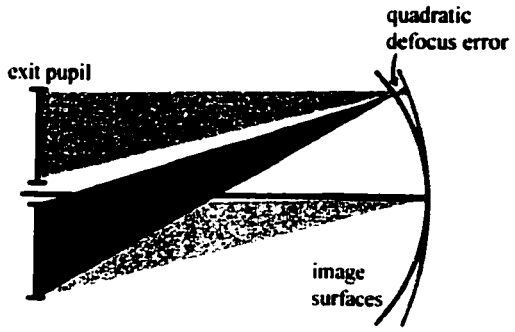

FIGURE 5.4. *A field curvature error between two apertures of a multiple aperture system.*

5.2 Aberration theory applied to multiple aperture systems

By definition, a single-aperture, rotationally-symmetric system has no beam-combining errors such as the ones described in Chapters 3 and 4. An off-axis piece of this system will have no beam-combining errors, then, either. This principle may be used to quantitatively put conditions on the plane-symmetric aberration coefficients listed above. If the conditions are met for each arm in a system, then the beam combining will be perfect.

This section is a summary of the paper given in Appendix B. The important results will be presented, but the detailed derivations can be found in the paper.

5.2.1 A system with perfect beam combining

The set of aberrations to third order that are possible in a rotationally symmetric system are given in Table 5.2.[36] To achieve a diffraction-limited system, the system cannot have aberrations that degrade the image quality: spherical aberration, coma, and astigmatism must be zero.

However, aberrations that do not degrade the point images may be acceptable. These include field curvature, distortion, defocus, tilt, and piston errors. In all of

aberration	name
W_{000}	piston
$W_{200}(\vec{H}\cdot\vec{H})$	quadratic piston
$W_{111}(\vec{H}\cdot\vec{\rho})$	tilt
$W_{020}(\vec{\rho}\cdot\vec{\rho})$	defocus
$W_{040}(\vec{\rho}\cdot\vec{\rho})^2$	spherical
$W_{131}(\vec{H}\cdot\vec{\rho})(\vec{\rho}\cdot\vec{\rho})$	coma
$W_{222}(\vec{H}\cdot\vec{\rho})^2$	astigmatism
$W_{220}(\vec{H}\cdot\vec{H})(\vec{\rho}\cdot\vec{\rho})$	field curvature
$W_{311}(\vec{H}\cdot\vec{H})(\vec{H}\cdot\vec{\rho})$	distortion
$W_{400}(\vec{H}\cdot\vec{H})^2$	quartic piston

TABLE 5.2. *Aberrations (to third order) possible in a system with rotational symmetry.*

these cases, the image plane could be moved, curved, or stretched in postprocessing into returning a perfect image over a wide field. Then, a wavefront that is perfect to third order by this definition will have the form:

$$\begin{aligned} W(H,\rho) &= W_{000} + W_{200}(\vec{H}\cdot\vec{H}) + W_{111}(\vec{H}\cdot\vec{\rho}) + W_{020}(\vec{\rho}\cdot\vec{\rho}) \\ &\quad + W_{311}(\vec{H}\cdot\vec{H})(\vec{H}\cdot\vec{\rho}) + W_{220}(\vec{H}\cdot\vec{H})(\vec{\rho}\cdot\vec{\rho}) + W_{400}(\vec{H}\cdot\vec{H})^2 \end{aligned} \tag{5.1}$$

To make this useful in a multiple aperture system, assume that an off-axis piece of this system will become one branch of a multiple aperture system. This is shown in Figure 5.5. The wavefront must be referenced to the center of the off-axis system, located at ρ_o. This transformation leaves the wavefront unchanged, so by definition it will still have perfect behavior.

FIGURE 5.5. *An off-axis piece of the perfect wavefront will have ideal behavior if used as an arm in a multiple aperture system. The wavefront should be reference to the center of the off-axis system, located at* ρ_o.

Let $\rho_o = \Delta/(D/2)$, where Δ is the real height in the exit pupil of the off-axis aperture in space and D is the diameter of the original, symmetric system. The normalized coordinate in the pupil of the off-axis system will be $\rho' = r/(D/2)$, where r is the real position in the exit pupil of the off-axis aperture. Both of these vectors, ρ_o and ρ', must have values less than one, unlike the usual definition of a normalized coordinate. Letting $\rho \rightarrow \rho_o + \rho'$ shows that the off-axis piece of the perfect wavefront has the form:

$$\begin{aligned} W(H,\rho') &= W_{000} + W_{200}(\vec{H}\cdot\vec{H}) + W_{111}(\vec{H}\cdot\vec{\rho}_o) + W_{111}(\vec{H}\cdot\vec{\rho}') \\ &+W_{020}(\vec{\rho}_o\cdot\vec{\rho}_o) + 2W_{020}(\vec{\rho}_o\cdot\vec{\rho}') + W_{020}(\vec{\rho}'\cdot\vec{\rho}') \\ &+W_{220}(\vec{H}\cdot\vec{H})(\vec{\rho}_o\cdot\vec{\rho}_o) + 2W_{220}(\vec{H}\cdot\vec{H})(\vec{\rho}_o\cdot\vec{\rho}') \\ &+W_{220}(\vec{H}\cdot\vec{H})(\vec{\rho}_o\cdot\vec{\rho}') + W_{311}(\vec{H}\cdot\vec{H})(\vec{H}\cdot\vec{\rho}_o) \\ &+W_{331}(\vec{H}\cdot\vec{H})(\vec{H}\cdot\vec{\rho}') + W_{400}(\vec{H}\cdot\vec{H})^2 \\ &-(nD\tan\overline{u})(\vec{H}\cdot\vec{\rho}_o) - ((nD\tan(u/2))(\vec{\rho}_o\cdot\vec{\rho}_o) \end{aligned} \tag{5.2}$$

where the last line is an adjustment that shifts the reference point to the new, mean value of the off-axis wavefront section. D is the diameter of the original aperture, n is an index of refraction, and u and $\overline{u}$ are marginal and chief ray angles, respectively. The second-order wavefront coefficients can be expressed in terms of system

parameters: $W_{000} = \sum nt$, $W_{111} = n'D' \tan \overline{u}'$, and $(n'D' \tan(u'/2)$. W_{000} has been defined to measure total pathlength through the system, rather than departure from a reference wavefront. W_{020} is defined as total curvature rather than just departure, as well. To second order, the pupils are defined as optically conjugate, so $W_{200} = 0$.

5.2.2 Forcing a plane symmetric system to have perfect beam-combining

Now this perfect wavefront can be compared to the general set of aberrations in plane symmetric systems. The coefficients on the plane-symmetric aberration terms must have the same form as the coefficients of the perfect wavefront with the same functional dependences. Note that $\vec{\rho}_o = |\rho_o| \vec{i}$. Also, allow for mispositionings in the entrance and exit pupils of the plane symmetric system, as compared to the pupils of the perfect system: $\delta_z, \delta'_z, \delta_y, \delta'_y$.

Because the aberration coefficients for aberrations that degrade the point image were set to zero in the perfect system, the terms in the plane symmetric system that degrade the point image are also required to be zero:

$$\begin{aligned} W_{02002} &= W_{11011} = W_{10010} = W_{03001} = W_{12101} = 0 \\ W_{12010} &= W_{21110} = W_{04000} = W_{13100} = W_{22200} = 0 \end{aligned} \tag{5.3}$$

The general wavefront for a plane-symmetric system, to third order, is then:

$$\begin{aligned} W_{PS}(H,\rho) &= \left[(n\delta_z - n'\delta'_z) + W_{00000}\right] + W_{01001}(\vec{i} \cdot \vec{\rho}) + W_{02000}(\vec{\rho} \cdot \vec{\rho}) \\ &+W_{11100}(\vec{H} \cdot \vec{\rho}) + [n\delta_y \tan \overline{u} - n'\delta'_y \tan \overline{u}' + W_{10010}](\vec{i} \cdot \vec{H}) \\ &+[n'\delta'_z \sin^2(\overline{u}'/2) - n\delta_z \sin^2(\overline{u}/2)](\vec{H} \cdot \vec{H}) + W_{21001}(\vec{i} \cdot \vec{\rho})(\vec{H} \cdot \vec{H}) \\ &+W_{30010}(\vec{i} \cdot \vec{H})(\vec{H} \cdot \vec{H}) + W_{22200}(\vec{H} \cdot \vec{\rho})^2 \\ &+W_{31100}(\vec{H} \cdot \vec{H})(\vec{H} \cdot \vec{\rho}) + W_{40000}(\vec{H} \cdot \vec{H})^2 \end{aligned} \tag{5.4}$$

Comparing equations 5.2 and 5.4 places requirements on the coefficients in the

plane-symmetric wavefront. If the requirements are satisfied, the plane-symmetric system will have perfect beam combining.

Comparing the constant phase terms gives:

$$(n\delta_z - n'\delta'_z) + W_{00000} = \sum nt - (nn'DD'/2nf')\rho_o^2 \tag{5.5}$$

where D and D' are the diameters of the wavefronts in the entrance and exit pupil of the full, perfect system, and f' is the rear focal length. This rule requires that the axial pathlength of the system be equal in the plane-symmetric and perfect systems. The term $(n\delta_z - n'\delta'_z)$ says that if it is not correct, the pupil positions should be adjusted longitudinally. This reiterates the discussion in Chapter 4, showing that the axial pathlength is easily controlled by the system geometry.

Comparing the constant tilt terms gives:

$$W_{01001} = n'D' \tan u'(1 - \rho_o)\rho_o. \tag{5.6}$$

This rule just states that the pointing in the plane symmetric systems and the perfect system must match, so that the axial rays have the same orientation out of the exit pupil. This again agrees with the constant tilt discussion in Chapter 4, which says that the pointing in the two branches should be chosen so that the images at zero field angle overlap.

Comparing the defocus terms gives:

$$W_{02000} = ((n'D' \tan u')/2)(1 - \rho_o)^2 \tag{5.7}$$

which says that the defocus in the plane symmetric system must be correct. Again, this is equivalent to the requirement from Chapter 4 that the power be chosen so that the image points at zero field angle overlap.

The linear tilt terms lead to the rule that:

$$W_{11100} = (n'D' \tan \overline{u}')(1 - \rho_o) \tag{5.8}$$

which keeps the images together as a linear function of field. It requires the magnifications in branches of a multiple aperture system to be equal.

Finally, comparing the linear piston terms gives:

$$(n\delta_y \tan\overline{u} - n'\delta'_y \tan\overline{u}') + W_{10010} = 0. \tag{5.9}$$

This says that linear piston terms are not acceptable in the plane symmetric system, but that they can be adjusted by changing the height of the pupil. This was discussed in Chapter 4, as a way to satisfy the Abbe sine condition and eliminate linear piston errors.

The remaining design rules are:

$$(n'\delta'_z \sin^2(\overline{u}'/2) - n\delta_z \sin^2(\overline{u}/2)) + W_{20000} = W_{200} + W_{220}\rho_o^2 \tag{5.10}$$

$$W_{30010} = W_{311} + nD\tan^3(\overline{u}/2) - n'D'\tan^3(\overline{u}'/2) \tag{5.11}$$

$$W_{21001} = 2W_{220}(1-\rho_o)\rho_o \tag{5.12}$$

$$W_{22000} = W_{220}(1-\rho_o)^2 \tag{5.13}$$

$$W_{31100} = W_{311}(1-\rho_o) \tag{5.14}$$

$$W_{40000} = W_{400} \tag{5.15}$$

Among other things, these rules suggest that quadratic piston can be corrected by pupil shift, and that a simple rule might exist that eliminates it. These rules also indicate that field curvature and distortion may be possible in a multiple aperture system and still satisfy the design rules for perfect beam combining.

5.3 Conclusions

Plane symmetric aberrations add significantly to the complexities of beam combining. A clear understanding of the forms of plane-symmetric aberrations is helpful, though, especially with regard to distortion.

By comparing an off-axis piece of a perfect wavefront to a general plane-symmetric wavefront, design rules for branches of multiple aperture systems were derived. Constraints on the wavefront coefficients in a plane symmetric system were given, and agree well with the low-order design rules discussed in Chapter 4. The constraints also suggest that quadratic piston can be corrected, and that field curvature and distortions in arms of multiple aperture systems may still lead to good beam combining under certain conditions.

Chapter 6

TWO 100 METER BASELINE DESIGNS

As discussed in the introduction, achieving 100 meter baselines will be very important for future generations of space telescopes and earth surveillance systems. Surveillance systems will ideally have fields of view of many degrees, while space telescopes will require fields of view on the order of arcminutes.

Designing systems with large baselines is challenging. However, applying just the first-order design rules discussed in the previous chapter shows that two of the simplest design types are plausible for use as space telescopes.

The first type of system is just a larger version of a traditional, rotationally symmetric telescope. The system is segmented to convert it to a multiple aperture system, as shown in Figure 6.1. A second common type of multiple aperture system uses an array of afocal telescopes that share combining optics. The two designs discussed here will illustrate the advantages and disadvantages of these types of systems.

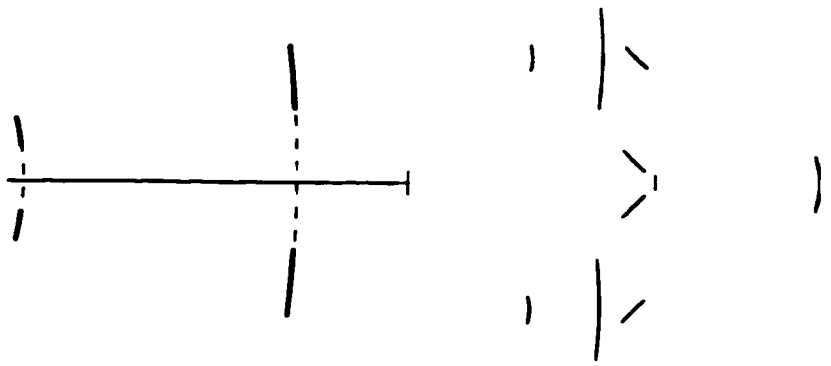

FIGURE 6.1. *A traditional system that has been segmented into a multiple aperture system, and an array of afocal telescopes with shared combining optics.*

6.1 Segmented rotationally-symmetric system

6.1.1 Geometry

The first design considered is shown in Figure 6.2. It is a traditional three-mirror telescope known as a "Paul" system, which has been segmented to produce a four-aperture system.[37] This type of segmented system has only traditional, rotationally-symmetric aberrations that are sampled by the primary array.

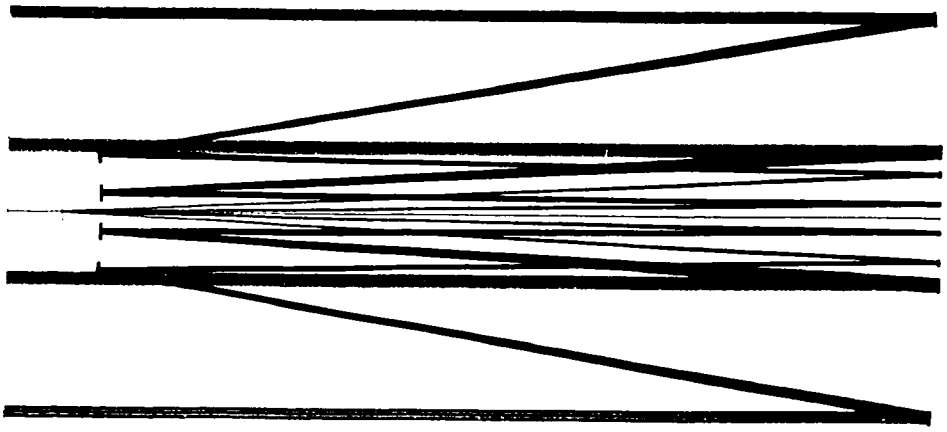

FIGURE 6.2. *A traditional three-mirror telescope, segmented for use as a multiple aperture system.*

The specifications for the system are shown in Table 6.1. The primary and tertiaries are convex, while the secondary is concave. The distance between the primary and secondary is 210 meters. The f/# of the system is 9.66 meters, because the effective focal length is 1000 meters and the total primary diameter is 103.5 meters.

6.1.2 Performance and limitations

The image has a high-frequency fringe pattern. The width of one fringe is equal to the width of the system's PSF before segmenting it. Compared to the unsegmented

	Primaries	Secondaries	Tertiaries
Radius	-590 m	-187.993704 m	-651.326293 m
Conic	-1.15802	-2.29980	-1.48738
Centers of outer mirrors	±50 m	±14.4369 m	±11.0091 m
Centers of inner mirrors	±16.666 m	±4.8034 m	±11.0091 m
Diameters of each segment	3.5 m	2.0 m	4.0 m

TABLE 6.1. *Geometry of the segmented Paul system.*

design, the segmented design wastes more light in the side lobes. The envelope is fairly wide because the individual apertures are small. At 1 μm, the width of the envelope over the fringes is (2.44 * 1 μm * 1000 m)/(3.5 m) = 697 μm. The width of one fringe, though, is (2.44 * 1 μm * 1000 m)/(103.5 m) = 23.6 μm. Thus, 29 fringes appear before the irradiance falls off to zero.

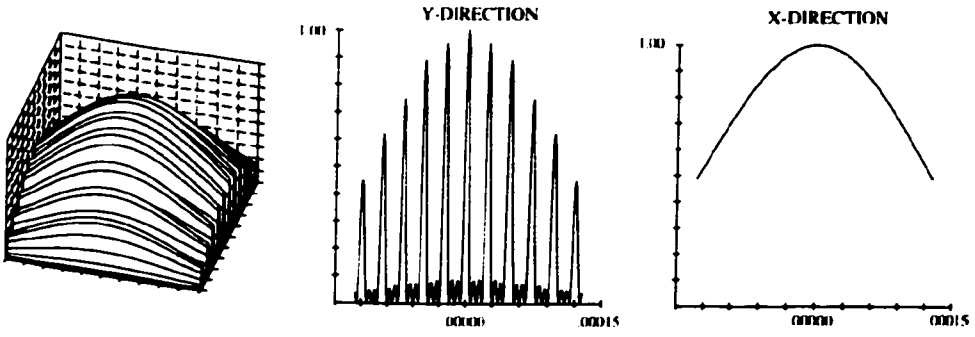

FIGURE 6.3. *Image for the segmented system, at zero field angle.*

The field of view in this system is 2.4 arcmin, where the Strehl value at that point is about 0.7. On axis, fifth-order spherical aberration dominates. Off axis, the performance is dominated by W_{242}, a fifth-order wavefront aberration that produces a distinct eye-shaped profile in the image. Vignetting at the tertiaries begins at roughly 7 arcminutes, so the size of the tertiaries could be reduced without degrading the system performance.

6.1.3 Satisfying the low-order design rules

Because this system is just a subset of a rotationally-symmetric system, the design rules are automatically satisfied. For example, the image planes from each arm cannot possibly be tilted or displaced with respect to one another because they are by definition the same image plane. Linear piston has been eliminated because the parent system has been corrected for coma. By definition, the focal lengths of each branch are equal. The tilt, defocus, and piston errors in the wave fans from the segmented system are at least quadratic as a function of field angle (see Figure 6.4). Comparing the wave fans of the parent and segmented system shown in Figure 6.4, it is clear that the segmented system is constrained to having only rotationally symmetric aberrations that can occur in the parent system.

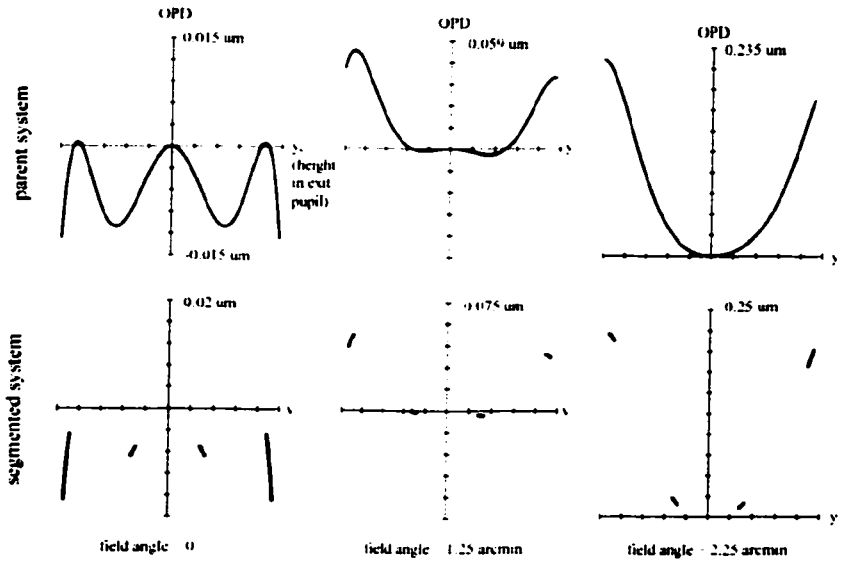

FIGURE 6.4. *Wave fans from the parent and segmented systems.*

6.2 Afocal primaries with a shared combiner

6.2.1 Geometry

Another common design to consider uses afocal telescopes in an array. The telescopes share a combiner, and a series of fold flats brings the beams from the afocal telescopes to the combiner. The layout is shown in the sketch below. Like the previous system, the system's f-number is 9.66 and the focal length of the system is 1000 meters, with a total system width of 103.5 meters. The center-to-center distance of the outer pair of collectors is 100 meters. The distance form the primary mirrors to the first combining mirror is 20 meters.

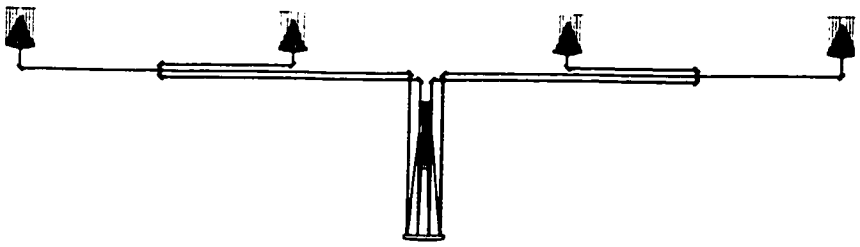

FIGURE 6.5. *A system with afocal primary telescopes that share a combiner.*

The four identical afocal telescopes each have a concave primary and a convex secondary. Both mirrors are parabolas, and their separation is 3.36 meters. Details are given in Table 6.2, and a closer view of the afocal telescopes is shown in Figure 6.6.

Afocal telescope	**Primary**	**Secondary**
radius	-7 m	-0.28 m
conic	-1	-1
shape	concave parabola	convex parabola
diameter	3.5 m	0.3 m

TABLE 6.2. *Specifications for the afocal collecting telescopes.*

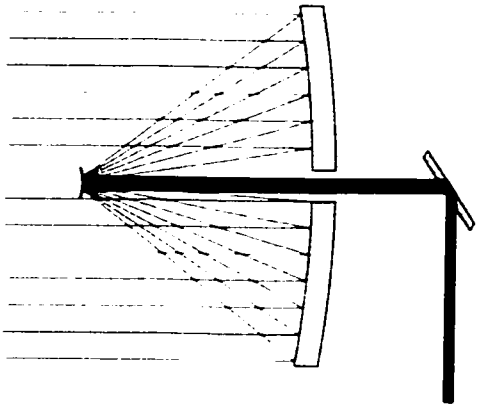

FIGURE 6.6. *Close-up of one of the afocal telescopes.*

The combiner is also a two-mirror system, and is shown in Figure 6.7. Details of the mirror are shown in Table 6.3.

Combiner	**Primary**	**Secondary**
radius	-38.919 m	-12.190
conic	-1.08099	-8.86364
shape	concave	convex
diameter	5 m	0.3 m

TABLE 6.3. *Specifications for the combiner.*

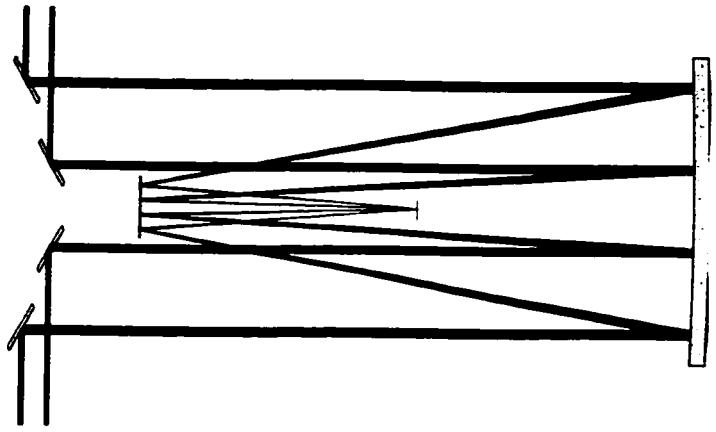

FIGURE 6.7. *A closer view of the two-mirror combiner, with input beams from an array of four afocal telescopes.*

6.2.2 Satisfying the low-order design rules

At any field angle, the focal lengths in each branch will match. This is due to the fact that the afocal telescopes have zero power. All the beams share a single combiner, so each branch will have the combiner's focal length.

The image planes for the various branches are all either horizontal or vertical anywhere in the beam path, since all the fold flats occur at an angle of 45 degrees and all the other elements are vertical with respect to the beams.

At zero field angle, the axial pathlengths from each arm do not generally match. The fold flats must be positioned to enforce this condition. This was done with two additional fold mirrors in each of the inner arms, as shown in Figure 6.8.

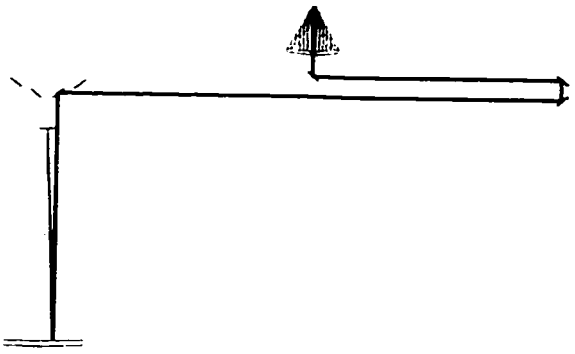

FIGURE 6.8. *The axial pathlengths in each arm are forced to match by sending the beam from the inner arm out and back with a pair of fold flats.*

Satisfying the sine condition for the axial rays is also straightforward. As discussed elsewhere, the sine condition can be restated for afocal systems as a requirement that the ratio of beam diameters to separations must remain constant between object and image space. The sine condition can then be satisfied in stages. The input beams have a diameter of 3.5 meters and separations of 33 1/3 meters. If the output beams have diameters of 0.1 meters, for example, then the beams must be separated by 0.952 meters before they enter the shared combiner. If the combiner is corrected for spherical and coma, then it will not introduce errors in the sine condition, and the system will have no linear piston errors.

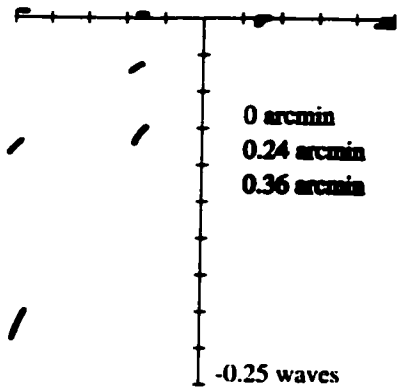

FIGURE 6.9. *Wave fans for various field angles, for the system with afocal primaries and a shared combiner.*

Figure 6.9 shows wave fans for the system, with the first aperture on the right obviously defined as the reference aperture. For a Strehl of 0.7, the field of view for this system is 0.8 arcminutes. This is smaller than the FOV of the previous system. The performance is limited by quadratic piston. A plot of the residual piston errors is shown in Figure 6.10, and they are quadratic with a linear component of zero clearly shown by the flat center region. At a field angle of 1.8 arcminutes, the beam is half-vignetted by one of the fold flats.

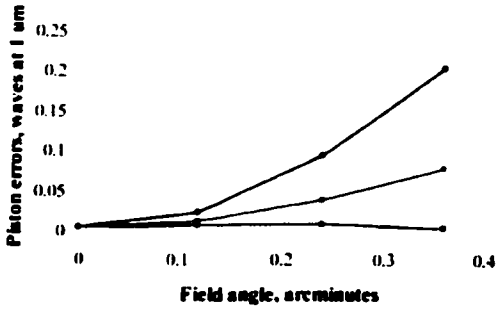

FIGURE 6.10. *The performance of the afocal system with shared combiner is limited by quadratic piston. The flat center of this plot shows that the linear piston has been corrected by satisfying the sine condition for the axial rays in the system.*

6.3 Comparison of the two systems

It is interesting to compare the two systems. "Segmented system" will refer to the system shown in Figure 6.2 and "afocal system" will refer to the system that uses an array of afocal telescopes, shown in Figure 6.5.

The segmented design is just a scaled version of a familiar three-mirror design. The aberrations in these systems are well known, since they are rotationally symmetric aberrations. No degrees of freedom in this system need to be used to satisfy the beam combining design rules because the design rules are automatically satisfied. The afocal system's design is less familiar. The available degrees of freedom must be used to satisfy the design rules and correct the aberrations within each branch. Because of this, systems like the afocal system will usually have a smaller field of view than segmented systems.

The segmented system is very long, about 200 meters, since scaling the system to reach a baseline of 100 meters also scales the system's length. The afocal system, in contrast, is just 20 meters long despite its 100 meter baseline in the perpendicular direction. This will simplify the mechanical structure needed to support the afocal system.

The mirrors in the segmented system will be more difficult and expensive to fabricate, since they are off-axis sections of conic surfaces. The afocal system contains only axially-symmetric mirrors. In each arm, two mirrors are parabolic and two to four are flat, so the mirrors in the afocal system will be inexpensive to fabricate.

The segmented system uses only three reflections per beam, while the afocal system uses up to eight reflections in each arm. More reflections will cause more losses and more background noise in the thermal IR. The afocal system also has eight reflections in the outer arms and six on the inner arms. This could lead to amplitude mismatches and polarization problems.

The afocal system has the advantage that afocal beams are easy to use when

matching pathlengths. Optical trombones have been used extensively in ground-based interferometers to maintain the equal pathlengths between the arms. The segmented system has no such convenient regions for pathlength adjustment.

A tolerance analysis at zero field angle shows that the segmented system has tighter tolerances than the afocal system. The exception is the tolerance on the tilt about the x-axis for the inner primary elements, which is comparable in the two systems. (The y and z axes will be defined to lie in the plane of the page, and the x axis comes out of the page.) The tolerance on this tilt angle is 0.035 microdegrees, which may be prohibitively tight for either system and will certainly require some kind of active control.

Mirror	z (um)	y	x	θ_x (μdegrees)	θ_y	θ_z
SEGMENTED:						
upper primary	0.011	0.14	6	0.5	0.5	6.0
inner primary	0.01	0.35	6	0.5	6.0	20.0
upper secondary	0.01	0.13	6.5	2.5	2.0	25.0
inner secondary	0.011	0.45	7	2.0	2.0	80.0
upper tertiary	0.011	0.65	30	2.5	2.5	160.0
inner tertiary	0.0105	1.8	30	2.5	2.75	450.0
AFOCAL:						
upper primary	0.4	2.7	2.6	22.0	20.0	—
upper secondary	0.4	2.7	2.6	0.25	0.27	—
inner primary	0.07	0.035	1.5	600.0	500	—
inner secondary	0.075	0.035	1.5	6.0	300	—
combiner primary	90.0	2750	28000	8000	4e5	—
combiner secondary	75.0	2600	25000	60000	2.7e6	—
upper fold	0.7	0.7	—	500	700	—
upper unfold	0.7	0.7	—	500	700	—
inner fold 1	0.7	0.7	—	6	400	—
inner fold 2	0.7	0.7	—	6	400	—
inner fold 3	0.7	0.7	—	6	400	—
inner fold 4	0.7	0.7	—	6	400	—

TABLE 6.4. *Tolerances at zero field angle for the segmented and afocal systems discussed.*

The tolerances are shown in Table 6.4. The tolerances were calculated by mul-

tiplying the effective degrees of freedom for each element (n) with the number of elements (m). Assuming the total allowable error for the zero field angle is 0.1 waves RMS and that the individual errors add as root mean squares, the error on each element can cause an RMS wavefront error of $0.1^2/(n*m)$. Each element was perturbed to generate this RMS wavefront error, and the value of the perturbation was taken as the tolerance. Perturbations in the plus and minus directions were similar for each perturbation.

In the segmented system, every offset and rotation has some effect on the system. The afocal system, though, clearly has some motions that don't affect the system performance overall. For example, rotation about the z-axis (horizontal in the page) has no effect on any of the elements in the afocal system, since they are all rotationally symmetric.

Also, as long as all of the afocal beams are collected, the exact position of th ecombining system is unimportant. This is true for finite fields of view, as well. Similarly, the exact positions of the afocal telescopes with respect to one another is relatively unimportant. If the fold flats are positioned correctly, the afocal telescopes can shift in x and y, and the sine condition remains satisfied.

The relative positions of the two mirrors in each afocal telescope will be important, but they are separated by a short distance that will be easily controlled in the design of the mechanical structure.

Basically, if the afocal telescopes are rigid and the combiner is rigid, their positions with respect to one another are largely irrelevant, provided the beams don't miss any of the mirrors altogether and that there is active control of the axial pathlengths in the system. This would be especially convenient for a configuration that in which the afocal telescopes are not mechanically trussed together.

It is important to notice that these two types of design are fairly common, but are only a very small part of all possible design space for multiple aperture systems. More general systems may take advantage of the strengths in both of these designs.

6.4 Conclusions

Two systems with 100 meter baselines were compared. Both systems had the same f/#, aperture diameters, and aperture separations.

The first system was a rotationally-symmetric Paul system that was then segmented to make a four-aperture system. The low-order design rules in this system were shown to be automatically satisfied. This is logical, since the parent system can have no beam combining errors.

The second system was an array of four afocal telescopes that share a three-mirror combining telescope. Fold flats were used in the inner two arms to satisfy the requirement that the axial pathlengths should match. Linear piston errors were eliminated by forcing the beam configuration into the combiner to be a scaled version of the afocal array. The angles of the fold flats were chosen so that there were no pointing errors in the system. The focal lengths of each arm were all equal to the focal length of the combining system, since the collection telescopes have zero power. Because the combining optics are shared, there were no defocus errors due to focal plane offsets or tilts.

The Paul system gave a larger field of view than the afocal array system, and used fewer reflections per arm of the system (which is especially important in the IR regime). The Paul system is also a very large system (200x100m), while the afocal array system is relatively compact (20x100m). The lack of afocal beams anywhere in the Paul system means that pathlength adjustment may be difficult, while the fold mirrors in the afocal system allow straightforward correction of axial pathlength errors. The tolerances on the mirrors in the Paul system were much tighter than the tolerances on the afocal system. Also, the mirrors for the Paul system were off-axis conics, which will be more difficult and expensive to fabricate than the rotationally-symmetric optics in the afocal system.

Chapter 7

LARGE BINOCULAR TELESCOPE BEAM COMBINER

7.1 Introduction

The Large Binocular Telescope is currently under construction on Mt. Graham in Arizona.[2],[26] A diagram of the LBT in operation is shown in Figure 7.1. The telescope consists of two 8.4 meter primary mirrors, mounted together on a 14.4 meter baseline.

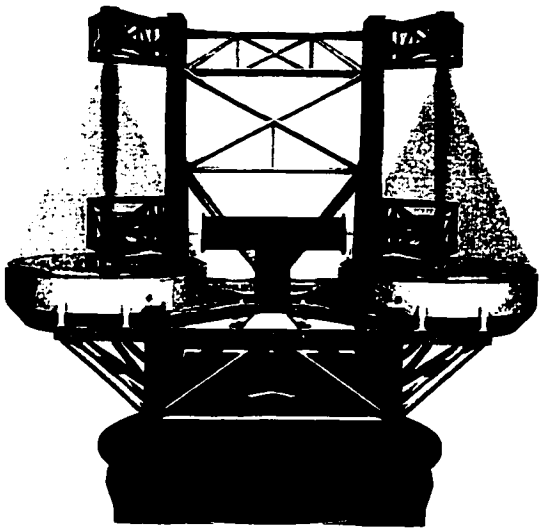

FIGURE 7.1. *A drawing of the Large Binocular Telescope. The beam combiner is housed in the T-shaped container at the center. Image created by ADS Italia and Max-Planck-Institut für Astronomie (Heidelberg).*

As an imaging interferometer, the LBT will operate over a wide field of view in the infrared at wavelengths from 2 to 20 μm, and it will have a resolution in one direction equivalent to a 22 meter single dish. The unaberrated PSF and MTF of the system are shown in Figure 7.2. Its relatively short baseline and large mirrors

give it a very broad MTF, so it transmits a wide range of spatial frequencies very well. Because of the two-aperture configuration, there is a second peak in the MTF at a spatial frequency proportional to the baseline length of the system, 14.4 meters. The large mirrors also give the LBT high sensitivity.

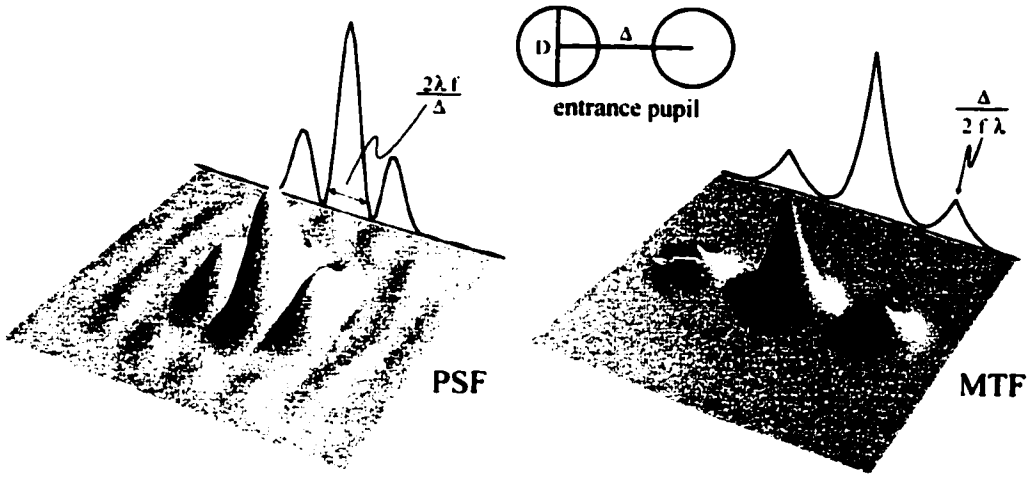

FIGURE 7.2. *The unaberrated PSF and OTF of the Large Binocular Telescope.*

Because of the relatively short, fixed baseline, it is possible to design a first-light beam combiner for the LBT that has a field of view of over an arcminute at a wavelength of 1 μm. The design, discussed in this chapter, illustrates some basic principles of designing beam combiners for wide-field, interferometric imaging.[38]

7.2 Primary / secondary configuration

A raytrace schematic of the LBT is shown in Figure 7.3. Each of the primaries is an f/1.142 parabola with a diameter of 8.408 meters and a central obscuration of 0.89 meters. The primaries were fabricated at the University of Arizona's Mirror Lab. They were cast as a single piece in borosilicate glass with a facesheet of 28 mm and a honeycomb structure behind it. Each weighs 16 metric tons. The primary/secondary systems are Gregorian telescopes, with concave adaptive secondaries.[39]

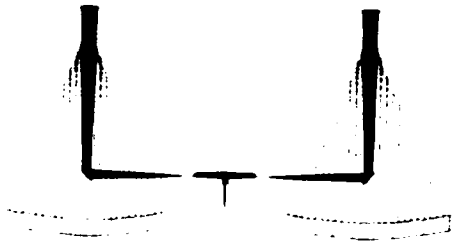

FIGURE 7.3. *A schematic of the Large Binocular telescope. Each primary mirror is 8.4 meters in diameter, with a baseline of 14.4 meters between their centers.*

The details of the primaries, secondaries, and tertiaries of the LBT are given in Table 7.1. The vertex coordinates of the mirrors are given with respect to the center of the image plane, where +z is up and +y is to the right in the figure. The angle α, refers to the tilt about the x-axis, which is out of the plane of the paper in the figure.

	Primary	**Secondary**	**Tertiary**	**Internal image**
radius	-19.2 m	-1.974 m	∞	—
shape	concave	concave	flat	—
conic	-1	-0.733	—	—
diameter	8.408 m	1.006 m	0.6034 m	—
y	7.2085 m	7.2085 m	7.2085 m	1.9085 m
z	-0.391 m	10.273 m	1.859 m	1.859 m
α	0	0	45°	90°

TABLE 7.1. *Specifications for the LBT primaries, secondaries, and tertiaries.*

7.3 Beam Combiner Design

The requirements for the beam combiner are fairly straightforward. The field of view should be diffraction limited over a field corresponding to the size of the isoplanatic patch in the best possible seeing conditions. The LBT is intended to operate from wavelengths of 0.4 μm to 20 μm, and the corresponding fields are then 5 arcsec to 10 arcminutes, respectively. In addition to this requirement, the beam combiner should

use a minimum number of warm reflections to reduce the infrared background noise. For the same reason, any obstruction of the beams should be avoided.[39]

The final beam combiner design, proposed by Phil Hinz, has three reflections in each arm of the system, and is shown in Figure 7.4. The image plane is at the bottom of the figure. Of the three mirrors, one is an ellipse and the other two are fold flats. The individual beams are f/40, and the entire LBT with the beam combiner is f/15. Specifications for the mirrors are given in Table 7.2. The vertex coordinates of the mirrors are given with respect to the center of the image plane, where +z is up and +y is to the right in the figure. The angle, α, refers to the tilt about the x-axis, out of the plane of the paper in the figure.

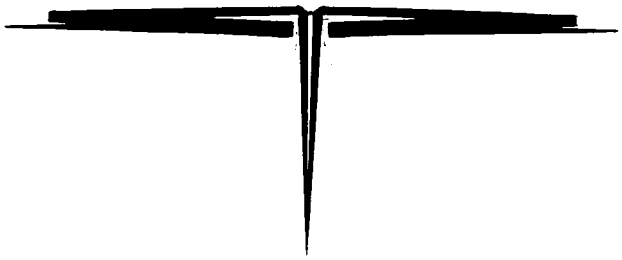

FIGURE 7.4. *The final design geometry of the LBT beam combiner. It uses one ellipse and two fold flats, and a total of three reflections.*

	Ellipse	**Fold 1**	**Fold 2**
radius	-2.642 m	∞	∞
shape	concave	flat	flat
conic	-2.16036	—	—
diameter	0.5224 m	0.0942 m	0.12 m
y	0.115 m	1.543 m	0.043 m
z	1.702 m	1.939 m	2.013 m
α	94.999°	90.181°	42.986°

TABLE 7.2. *Specifications for the final design of the LBT beam combiner.*

This system has several advantages. Two of the mirrors are flats and will be inexpensive and easy to fabricate. The image performance is good even at 1 μm and

will have more than adequate field in the range of 2 to 20 μm. However, the elliptical mirror partially obscures the beam starting at a field angle of about 3 arcmin, so at 20 μm the full isoplanatic patch cannot be used. The fold flats furthest from the elliptical mirrors offer a good position for tip/tilt adjustment if the tolerances show that active control will be needed.

The beam combiner is about 3.1 meters wide and 2 meters behind the image plane. Because this system must operate in the thermal infrared, the beam combiner must be cooled inside a dewar. The size of the system poses a challenge for the mechanical design of the dewar, but a solution using multiple chambers has been found. A smaller system would have avoided this problem.

7.4 Image and limitations to the field

The beam combiner described above has a 1 arcminute field of view at a wavelength of 1 μm, where the lowest Strehl ratio allowed is 0.7. Cross sections of the point spread functions at 1 μm are shown in Figure 7.5. Each fringe in these images is 36 μm in width.

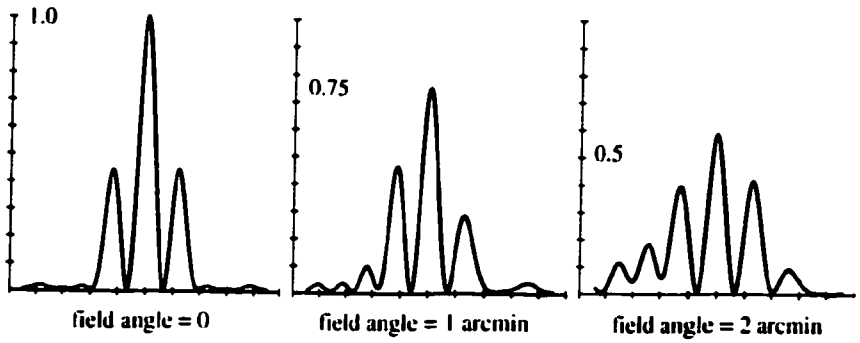

FIGURE 7.5. *Cross-sections of the point spread functions from the LBT at 0, 1, and 2 arcminutes. The FOV for a Strehl ratio of 0.7 is 1 arcminute at 1 um.*

The Strehl ratios as a function of field angle are shown in Figure 7.6. The PSF height falls off slightly faster in the x direction (motion parallel to the image fringes)

than in the y (motion perpendicular to the image fringes).

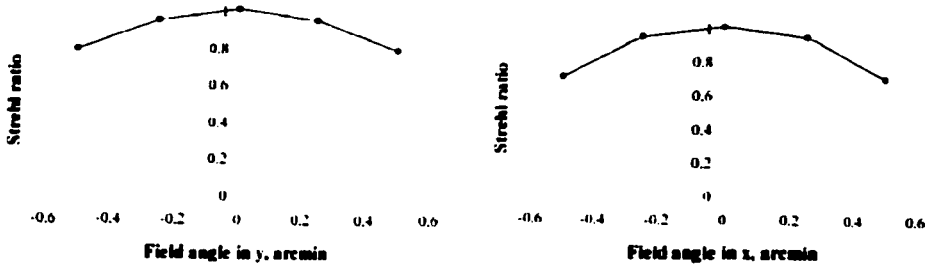

FIGURE 7.6. *The Strehl ratios as a function of field angles, for the LBT configuration with beam combiner.*

Figure 7.7 shows that there is no linear beam separation in the image, which just indicates that the focal lengths of each arm are equal. There is a strong quadratic beam separation due to the asymmetric distortion in each arm. Since each arm has only one plane of symmetry, the distortion in the arms is generally not rotationally symmetric. This type of situation is discussed in more detail in Chapter 4. One arm is the mirror image of the other, so the images from each arm separate due to the asymmetric distortions in each arm of the system.

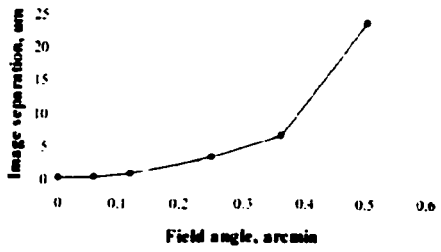

FIGURE 7.7. *Quadratic image separation (differential distortion) as a function of field angle. The linear component is zero because the focal lengths of the arms match.*

The system is designed to bring the beams together at the shallowest angle possible. This minimizes the difference between the image plane tilts, since the image

planes from each branch are nearly horizontal. The defocus errors that are linear with field are then very small.

The linear piston errors are eliminated by using the optimization routine discussed in Chapter 4. The method uses only axial or nearly axial rays, which are the least likely rays to be aberrated. It demands that the fringes and image locations stay together for small field angles and has the form $\frac{d}{\sin\theta} = \frac{\Delta y}{\sin\alpha}$. Figure 7.5 shows the PSFs of the system as a function of field, and it is clear that the fringes are not traveling off the images, indicating that the sine condition has been satisfied. Figure 7.8 shows the remaining piston error after the linear piston is corrected. The quadratic piston is not the dominant aberration remaining in this system, however.

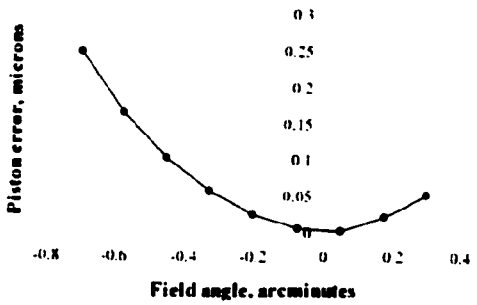

FIGURE 7.8. *The linear component of the piston error is zero, because the sine condition has been satisfied for the axial rays in each branch.*

The field of view of this system is limited primarily by astigmatism in the individual arms and secondarily by the differential distortion. Wave fans from the system are shown in Figure 7.9. The differential distortion is visible in the wave fans as increasing tilt error in the aperture on the left. In the image plane, the tilt error is causing the image from the left branch to move away from the ideal image point. The aperture on the right shows no tilt because its image point has been taken as the reference point. The quadratic piston is also visible as a constant offset of the wave fan in the left aperture.

The limiting aberration of the system is astigmatism in the individual arms, and only appears in a two-dimensional plot of the phase errors. A contour plot with strong astigmatism at a field angle of 1/4 arcminute is shown in Figure 7.10. One of the flats in the system could be powered to allow for correction of the astigmatism, and then the differential distortion would be the primary limitation.

If the system were designed instead to use on-axis optics, the differential distortion problem would be eliminated. The sine condition for the axial rays would then need to be modified so that the fringes remained at the distorted image points, rather than the geometrically predicted image points. Field curvature would also become a problem with an on-axis design, as well as the usual physical obscuration problems when using on-axis optics.

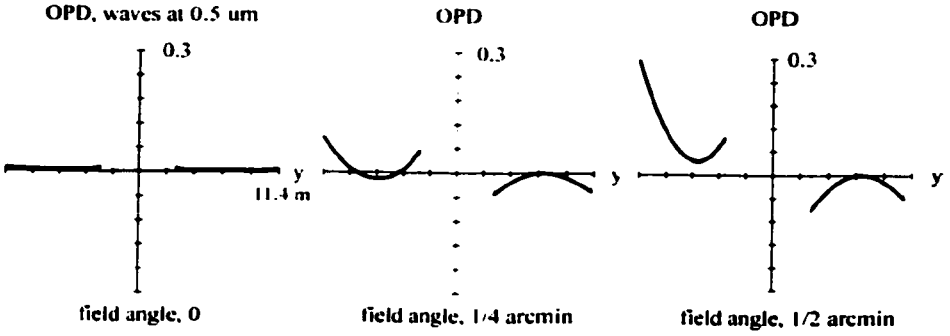

FIGURE 7.9. *Wave fans from the LBT, at field angles of 0, 1/4 arcmin, and 1/2 arcmin. The field angle is in the direction of the baseline between the primary mirrors.*

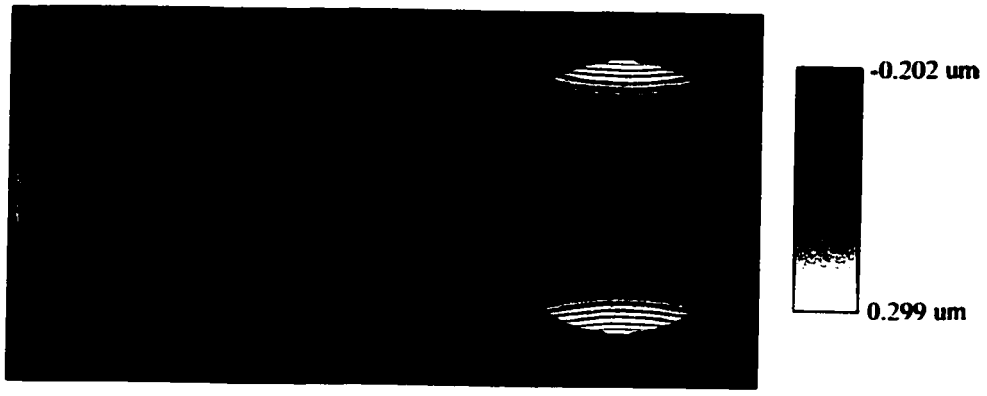

FIGURE 7.10. *A contour plot of the astigmatic wavefront in the exit pupil of the LBT. The field angle is 1/4 arcminute.*

7.5 Tolerances

The tolerances in the optical system will determine whether one of the mirrors in the beam combiner will require active tip/tilt/piston control. Since the system is intended to run at 2 - 20 μm, the beam combiner will be inside a dewar, where active control is difficult. An initial tolerance analysis suggests that active control will be necessary.

To carry out a simple tolerance analysis, diffraction analysis was used to determine how much piston, tilt, and defocus difference between the two branches of the system could be tolerated. This total amount of error was then divided between the mirrors in each arm to give an estimate of the tolerance on the mirror positions.

Diffraction analysis was used to determine the total amounts of piston, tilt, and defocus that the LBT system could tolerate. Phase terms were added to the perfect exit pupil phase function, of the form $e^{i2\pi\Delta}$, $e^{i2\pi(ax+by)}$, or $e^{i2\pi c(x^2+y^2)}$ corresponding to piston, tilt, and defocus, respectively. Fraunhofer diffraction theory was then used to calculate the image from the aberrated exit pupil. The height of the resulting image versus the height of the unaberrated image was used to calculate the Strehl

ratio. This method is discussed in detail for a two-aperture system like the LBT in Chapter 3.

The peak Strehls as a function of the aberrations considered are shown in Figure 7.11. Because these point spread functions can have double-peak features, especially in the case of piston, "peak Strehl" was used instead of the traditional Strehl ratio which assumes that the PSF of a system has one distinct peak. "Peak Strehl" was defined as the highest point in the PSF, wherever it might be located. This leads to the discontinuity in the plot of Peak Strehl versus piston: the Strehl has stopped measuring one peak and started measuring another, now higher, peak. The calculations were done in the M-band, centered at 4.8 μm and with a width of 1.2 μm.

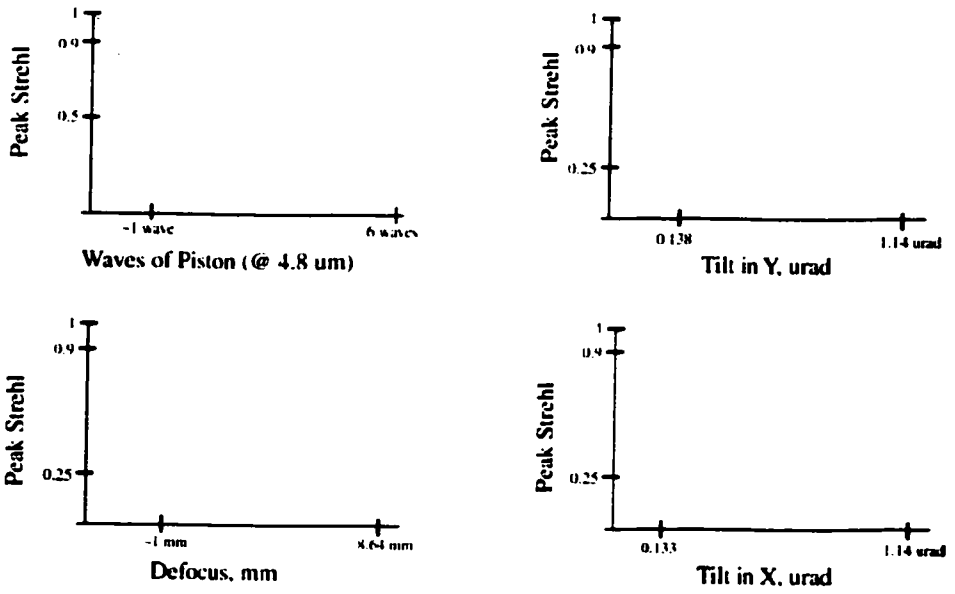

FIGURE 7.11. *The Strehl ratios for the LBT with its beam combiner, as a function of the low-order aberrations in one of the telescopes.*

These plots give a good estimate of the total amount of each aberration that could be tolerated by the system, as shown in Table 7.3. These numbers are relative: a "tilt error" is the difference in tilt between the two apertures, for example. A peak

Strehl of 0.9 was taken to be the minimum tolerable for each aberration, and if all the errors were present at their maximum allowed amounts, the Strehl of the overall system would be 0.68.

A first guess at the positional tolerances on the mirrors, then, says that the total error allowable should be divided by the number of mirrors in the system, which is 12. The piston and defocus tolerances are not extremely tight, especially since the LBT will have adaptive secondaries. However, even with the adaptive secondaries, the tilt tolerances are tight. Active control of one of the beamcombiner's mirrors will almost certainly be necessary.

aberration	**total error allowable**	**per mirror**
piston	1 wave (4.8 μm)	0.4 μm
defocus	1 mm (f/15 system)	83 μm
tilt perpendicular to baseline	0.028 arcsec	0.002 arcsec
tilt along the baseline	0.027 arcsec	0.002 arcsec

TABLE 7.3. *An estimate of the positional tolerances for the LBT beam combiner mirrors.*

7.6 Conclusions

The Large Binocular Telescope illustrates a design that has only planar symmetry. A coherent image with a wide field of view is achieved with just three reflections, only one of which is powered. This could not have been done by relying on more axially-symmetric designs.

The behavior of the LBT beam combiner illustrates some of the errors expected in a plane-symmetric system. Astigmatism is the limiting aberration, and could be corrected if necessary with a toric surface on one of the fold flats in each arm. Linear defocus errors also appear, but are minimized by bringing the beams to focus as closely together as possible. The constant piston, tilt, and defocus errors are all zero, since the two arms in the system are mirror-images of one another. This leads

to differential distortion in the system, though. The sine condition is satisfied so that the linear piston errors are zero. A small amount of quadratic piston remains in the system.

An estimate of the tolerances was calculated by plotting the Strehl ratio at zero field angle for the system in the presence of low order aberrations (piston, tilts, and defocus). Assuming that the errors should initially be equally divided among the mirrors, the tolerances on each mirror's position and power were estimated. The results indicate that active control on one of the mirrors in the beam combiner will be necessary.

Chapter 8

INVESTIGATION OF FLAT-MIRROR TELESCOPES

8.1 Introduction

A gossamer mirror technology is being developed in our lab, and it is currently one of the few technologies that may be light enough to build 100 meter baseline telescopes with high fill factors. Baselines of 100 meters would allow extrasolar planet imaging and earth-observation satellites in geosynchronous orbit around the earth.

The technology utilizes thin membranes that are stretched over frames to create flat mirrors. A uniform frame allows for uniform tension in the membrane. If the membrane has constant thickness, a flat mirror of good quality can be achieved. A current six-inch gossamer mirror has a wavefront error of $\lambda/20$ in the visible, and is shown below in Figure 8.1. Demonstrations of 1 meter have been flat to $\lambda/4$ in the visible for the inner 60% of the areas.[40]

FIGURE 8.1. *A membrane mirror, 6" in diameter.*

We have studied a plausible design for a space telescope that uses these flat membrane mirrors. In this chapter, the system geometry is discussed. The performance of the proposed systems is predicted using wavefront reconstruction, and the calculations are confirmed with full raytrace models of a few of the systems. Then, the

design space for these systems is explored.

8.2 A space telescope design with flat membrane mirrors

Membrane mirrors could be used to form a very large primary mirror for a space telescope. A sketch of the fundamental design idea is shown in Figure 8.2. The primary is an array of flat, membrane mirrors. Each flat is tilted so that the overall structure approximates a single concave primary. A mechanical structure holds the primary mirrors in place.

The primary array could fly separately from the rest of the telescope, allowing the system to be long and the primary to be weak. This would improve the performance of the faceted primary. For simplicity, the primaries could share a secondary mirror. The secondary, tertiary array, and image planes could be mounted together mechanically to form the second free-flying part of the system.

The tolerances on the primary positions will be prohibitively tight unless the system is designed to compensate for it. In the proposed system, the secondary images the primary array onto a tertiary array so that the exit pupils of the system are at the tertiary locations. Each mirror in the tertiary corresponds to one of the primary mirrors. If the tertiary array has tip/tilt/piston motion control, the tertiaries can be used to compensate for motion in the primary flats. This eases the tolerances on the positions of the primary flats and allows the large backing structure of the primaries to be much lighter than it would otherwise have to be for rigidity reasons.

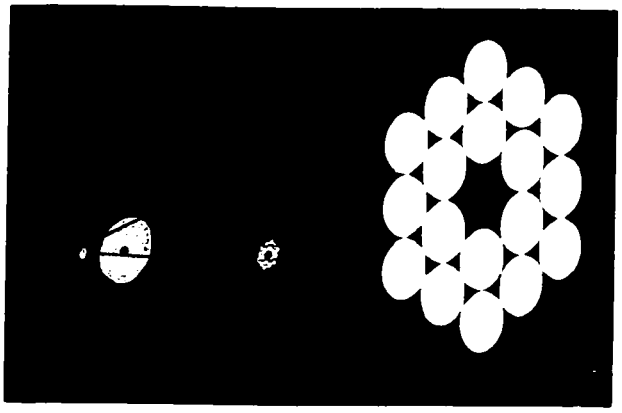

FIGURE 8.2. *Flat, gossamer mirrors could be used to assemble a large primary. A tertiary in the system could be used to compensate for motion of the primary segments.*

8.3 Geometry of a single arm in the system

Figure 8.3 shows a sketch of what a single arm of such a system might look like. This system can be thought of as a three-mirror telescope, with the power that should have been in the primary mirror now moved to the tertiary mirror. Alternatively, the system can be interpreted as a two-mirror Gregorian telescope with a siderostat directing light into the telescope. A complete space telescope would be comprised of many of these branches.

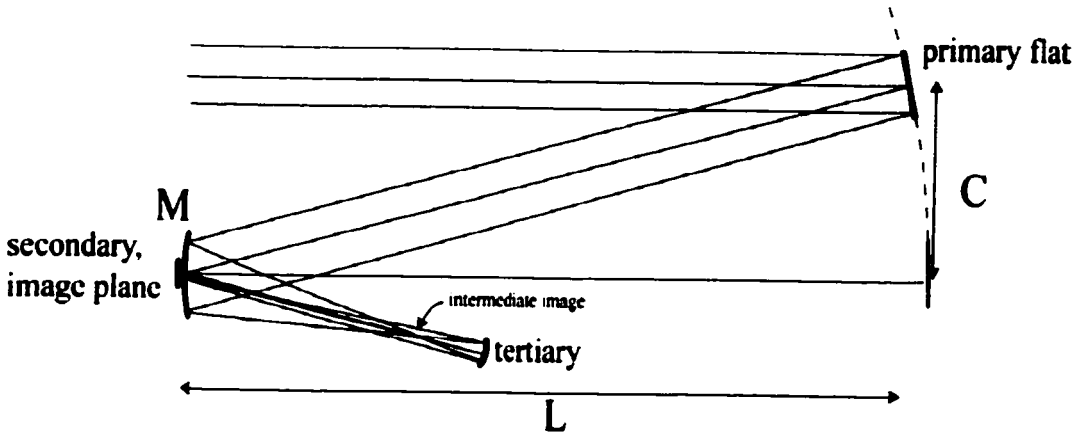

FIGURE 8.3. *A sketch of a single arm of the gossamer system.*

The parameter C is the distance the primary flat is off-axis, where the axis is defined as perpendicular to and at the center of the secondary mirror. The parameter L is the distance between the secondary and primary for the case where $C = 0$. The system in which $C = 0$ will be used as a reference for all the arms in the completed system; all other arms will be made to work with the on-axis arm, so that the system as a whole works as a single unit. The parameter M describes the demagnification of the primary onto the tertiary, and the parameter D is the diameter of the primary flat.

8.3.1 Primary mirror position and tilt

The tilt of the primary flat must be chosen so that the axial ray is directed to the center of the secondary mirror. The secondary's power does not affect the output angle of the axial ray, and the angle after the secondary will be equal and opposite the input angle, as shown in Figure 8.5.

The vertex position of the primary is constrained by the sine condition, as shown next. To eliminate linear piston errors as a function of field angle, the sine condition must be satisfied for the axial ray of any branch in the completed system.

As shown in Figure 8.4, the afocal sine condition requires that:

$$\frac{h}{\sin\theta} = \kappa \tag{8.1}$$

where κ is a constant, h is the height of an axial ray in the entrance pupil with a field angle of zero, and θ is the ray angle in image space.[41]

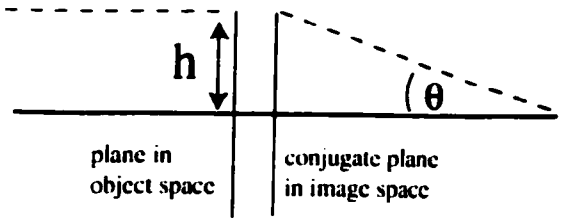

FIGURE 8.4. *The afocal sine condition requires that* $h/\sin\theta = \kappa$ *for all* θ, *where* κ *is a constant.*

In the case of one arm of the gossamer system, the axial ray angle in image space for any branch is equal to the ray angle after reflection from the primary, as shown in Figure 8.5. The axial ray has an initial height of C. The angle of the axial ray in image space is just θ, and $\tan\theta = C/L$, which is approximately equal to $\sin\theta$ for small θ. Then Equation 8.1 is satisfied for all branches of the final system if $\kappa = L$. This says that the vertex of the primary in any arm should be located on a sphere of radius L, with respect to the center of the secondary.

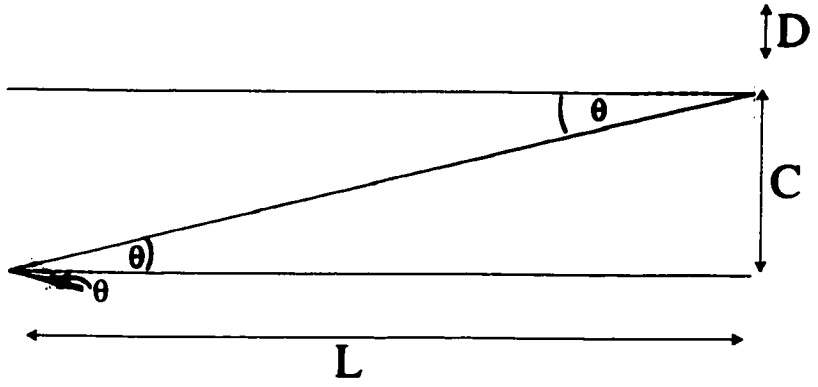

FIGURE 8.5. *For the five-flat systems, the sine condition requires that the primaries be located on a sphere of radius L.*

The tilt of the primary must still direct the axial ray to the center of the tertiary. Then, the vertex of the primary mirror is located on a sphere of radius L, but the primary's tilt is not tangent to that sphere. The primary flat has instead been tilted to "focus" at the center of curvature of the primary array, rather than at the focal length of the primary array at $L/2$.

The tilt angle and vertex position for the primary flat are given in Table 8.1, where the origin is defined as the vertex of the secondary mirror. The y-axis extend up vertically from the origin, and the z-axis extends horizontally to the right. The tilt angle, α, is about the x-axis and is measured from the vertical.

coordinate	value
y	C
z	$\sqrt{L^2 - C^2}$
α	$\frac{1}{2}\arctan(\frac{C}{\sqrt{L^2-C^2}})$

TABLE 8.1. *Vertex locations and tilt angle for a primary flat in the gossamer system.*

8.3.2 Secondary mirror power and shape

Because the secondary is shared by all of the primaries, its surface shape was chosen to be spherical. Because of this design choice, an arm in any orientation with the same parameter C will "see" the same secondary. For the reference system of $C = 0$, the primary lies a distance L away from the secondary. The magnification between the primary and tertiary is M, so the secondary power will be:

$$\varphi_2 = \frac{1+M}{ML} \tag{8.2}$$

Used in a general branch of the gossamer system, the axial ray will encounter the secondary at an angle. This will produce astigmatism because each collimated beam from the primary segments sees two radii of curvature in the secondary: one radius of curvature in the x-direction and a foreshortened radius of curvature in the y-direction. The Coddington equations calculate where the two astigmatic foci are located, as measured along the axial ray.[35] In the y-z plane, the focal distance is shorter than the paraxial focal length of the secondary:

$$t' = \frac{ML}{M+1}\frac{\sqrt{L^2-C^2}}{L}. \tag{8.3}$$

In the x-z plane, the focal distance is longer than the paraxial focal length of the secondary:

$$s' = \frac{ML}{M+1}\frac{L}{\sqrt{L^2-C^2}}. \tag{8.4}$$

These distances can be used to define "oblique" powers for the secondary mirror:

$$\varphi_t = 1/t' \tag{8.5}$$

$$\varphi_s = 1/s'. \tag{8.6}$$

8.3.3 Tertiary mirror position and tilt

The tertiary position must be chosen so that the axial pathlengths in all branches are equal, so that there are no constant piston errors in the beam combining. Again

considering the reference system, and beginning in the plane $z = 0$, the pathlength that the axial ray travels through the system will be $L + L + ML + ML$. Beginning in the plane $z = 0$, the pathlength through the system when $C \neq 0$ will be $L\cos\theta + L + 2ML \cdot f(\theta)$, where $f(\theta)$ is some function that shows how the pathlength between the secondary and tertiary changes with the system angle, θ. Equating the above OPLs and solving for $f(\theta)$ gives:

$$f(\theta) = \frac{1+M}{M} - \frac{1+\cos\theta}{2M} \tag{8.7}$$

so that the pathlength between the secondary and the tertiary, d, measured along the axial ray for a given primary segment, is:

$$d = L(M + \frac{1}{2}(1 - \frac{\sqrt{L^2 - C^2}}{L})) \tag{8.8}$$

using the fact that $\cos\theta = \sqrt{L^2 - C^2}/L$.

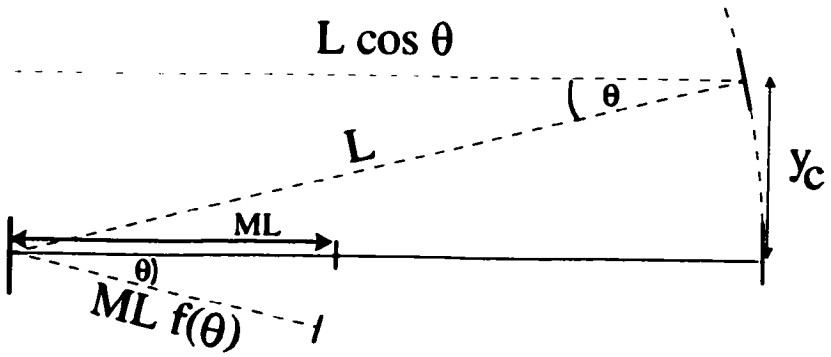

FIGURE 8.6. *Axial ray pathlengths must be equal for all branches. Calculate $f(\theta)$ by equating the pathlength in an off-axis branch to the pathlength in an on-axis branch.*

Then, the vertex positions of a tertiary mirror in a branch of the gossamer system can be calculated with simple geometry, and these positions are shown in Table 8.2.

The tilts of the tertiary mirrors are just equal to θ. This places the tertiary perpendicular to the axial ray in the branch, and directs the ray back on itself to the image point at the origin. This also means that the tertiary mirror doesn't add

Coordinate	Value
y	$\frac{-1}{2L}\sqrt{2LC\left\{L(1+2M+2M^2)-\sqrt{L^2-C^2}(1+2M)\right\}-C}$
z	$\sqrt{L^2-C^2}\left(\frac{1}{2}-\frac{\sqrt{L^2-C^2}}{2L}+M\right)$
α	$-\arctan\left(\frac{C}{\sqrt{L^2-C^2}}\right)$

TABLE 8.2. *Tertiary locations and tilts for a general branch of the gossamer system.*

additional astigmatism to the beam. The tilt in terms of the system parameters is also shown in Table 8.2, and it is twice the tilt of the primary flat but in the negative direction.

8.3.4 Tertiary mirror power

The tertiary is allowed to be aspheric, to correct for the aberrations introduced by the primary/secondary pair. To first order, it will be used to correct for the astigmatism introduced by the secondary. The oblique powers given by equations 8.5 and 8.6 determine the distance from the secondary to the intermediate images, measured along the axial ray. Then, the distance between the intermediate images and the tertiary are known. The distance from the tertiary to the image plane is also known. Using the imaging equation, the necessary focal lengths of the tertiary can be solved for. These are given in Table 8.3.

Tertiary focal lengths
$f_y = \frac{2L^2(1+4M+4M^2+2M^3)-2L(1+2M)^2\sqrt{L^2-C^2}-C^2(1+3M)}{4(1+2M)(LM+L-\sqrt{L^2-C^2})}$
$f_x = \frac{C^2(1+M)(2L+4ML-\sqrt{L^2-C^2})-2L^3(1+2M)^2+2L^2\sqrt{L^2-C^2}(1+4M+4M^2+2M^3)}{4C^2(1+M)+4L(1+2M)\left[\sqrt{L^2-C^2}(1+M)-L\right]}$

TABLE 8.3. *Tertiary focal lengths in terms of the system's parameters.*

For the reference system with $C = 0$, both of these reduce to $f = (1+2M)/(LM^2)$ since there is no astigmatism introduced by the secondary in that case.

With the tertiary powers chosen, the focal length of a general branch of the system is given by:

$$f_{arm} = \frac{\sqrt{L^2-C^2}M\left[C^2(1+3M)+(2L\sqrt{L^2-C^2}-2L^2)(1+2M)^2-4L^2M^3\right]}{(C+3CM)^2+(2L\sqrt{L^2-C^2}-2L^2)(1+6M+11M^2+6M^3)-4L^2M^4} \quad (8.9)$$

which reduces to $-L$ if $C = 0$.

8.3.5 Image plane location

The image plane has been chosen to lie directly behind the secondary mirror. This allows both to be mounted on a single structure. It also prevents the tertiary from introducing additional astigmatism into the beam. The tilt of the image plane must be chosen to be horizontal, since it must be shared by any number of arms in the system. Tilting it would create very large errors for any arms oriented against the direction of the tilt.

8.3.6 Summary

A summary of the calculations for a general branch of the gossamer system are given in Table 8.4.

8.4 An example system

To get an idea of how these parameters interact, consider a system with $M = 0.05$ and $L = 1000$ meters. Many branches with varying primary flat heights, C, would be used together in the final system. Table 8.5 shows the values of the important parameters for branches with primary flat heights of $C = \{0, 15, 30, 50\}$. Figures 8.7, 8.8, and 8.9 show the oblique focal lengths, tertiary focal lengths, and branch focal lengths as a function of the height of the primary flat, C.

primary	**value**
y	C
z	$\sqrt{L^2 - C^2}$
α	$\frac{1}{2}\arctan(\frac{C}{\sqrt{L^2-C^2}})$
f	∞
secondary	**value**
y	0
z	0
α	0
f	$\frac{ML}{1+M}$
tertiary	**value**
y	$\frac{-1}{2L}\sqrt{2LC\left\{L(1+2M+2M^2) - \sqrt{L^2-C^2}(1+2M)\right\} - C}$
z	$\sqrt{L^2-C^2}(\frac{1}{2} - \frac{\sqrt{L^2-C^2}}{2L} + M)$
α	$-\arctan\left(\frac{C}{\sqrt{L^2-C^2}}\right)$
f, tangential	$\frac{2L^2(1+4M+4M^2+2M^3)-2L(1+2M)^2\sqrt{L^2-C^2}-C^2(1+3M)}{4(1+2M)(LM+L-\sqrt{L^2-C^2})}$
f, saggital	$\frac{C^2(1+M)(2L+4ML-\sqrt{L^2-C^2})-2L^3(1+2M)^2+2L^2\sqrt{L^2-C^2}(1+4M+4M^2+2M^3)}{4C^2(1+M)+4L(1+2M)\left[\sqrt{L^2-C^2}(1+M)-L\right]}$
image	**value**
y	0
z	0
α	0

TABLE 8.4. *A summary of mirror positions, tilts, and powers for a branch of the gossamer system.*

C	0	15	30	50	units
primary, y	0	15	30	50	meters
primary, z	1000	999.887	999.550	998.749	meters
primary, α	0	0.0075	0.0150	0.0250	radians
f, secondary	47.619	47.619	47.619	47.619	meters
f oblique, y	47.619	47.614	47.598	47.559	meters
f oblique, x	47.619	47.624	47.640	47.679	meters
tertiary, y	0	-0.751	-1.507	-2.531	meters
tertiary, z	50	50.051	50.202	50.562	meters
tertiary, α	0	-0.015	-0.030	-0.05	radians
tertiary, f y	2.273	2.329	2.497	2.891	meters
tertiary, f x	2.273	2.319	2.458	2.785	meters
f, branch	-1000	-975.763	-909.857	-785.320	meters

TABLE 8.5. *Specifications for an example system with a length of 100 meters and a primary/tertiary demagnification of 0.05.*

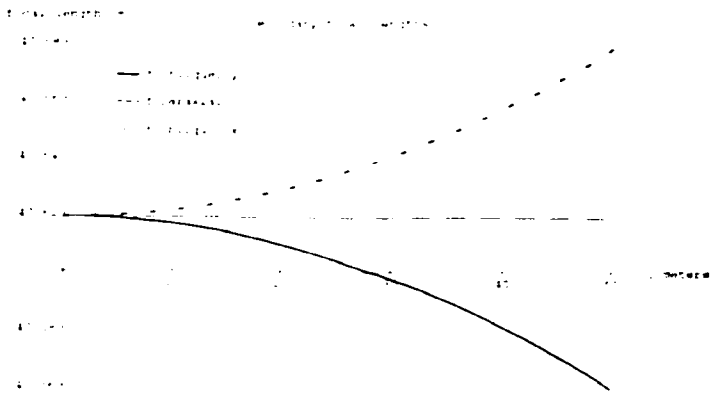

FIGURE 8.7. *A plot showing the paraxial and oblique powers of the secondary mirror, for an example system with L=1000 meters and M=0.05, as a function of the height of the primary flat, C.*

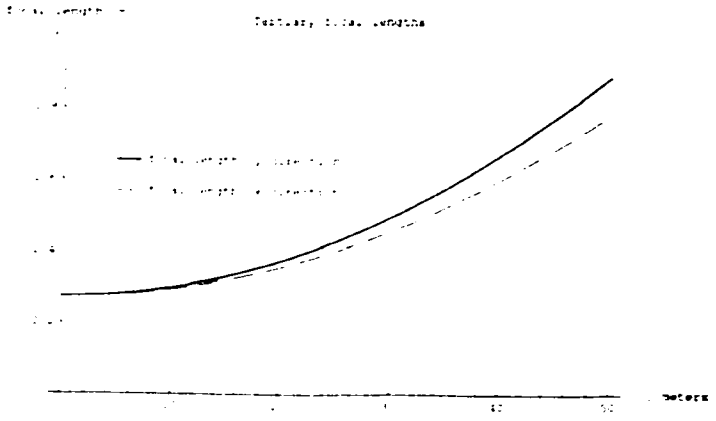

FIGURE 8.8. *A plot showing the powers of the tertiary mirror, for an example system with L=1000 meters and M=0.05, as a function of the height of the primary flat, C.*

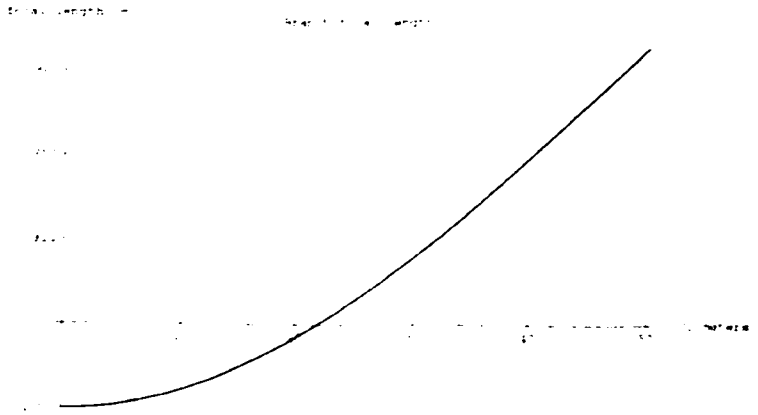

FIGURE 8.9. *A plot showing the focal length of a branch as a function of C, the height of the primary flat, for an example system with L=1000 meters, M=0.05.*

8.5 Linear tilt and defocus errors

Table 8.6 summarizes how the degrees of freedom in this three-mirror system were used to satisfy the low-order combining errors discussed in Chapter 3. The constant defocus has been forced to zero by forcing the focal plane vertex of a general system to have the same location as the focal plane vertex for the reference case ($C = 0$).

The constant piston has been forced to zero by forcing the axial pathlength in the general arm to be equal to that of the on-axis arm. The linear piston has been forced to zero by satisfying the sine condition with the vertex location of the primary flats. And finally, there are no constant tilt errors, since all the images at zero field angle come to focus at (0,0), as set by the tertiary power and tilt. As the table shows, the remaining degrees of freedom have been used for other purposes.

secondary position, tilt	fixed as a reference
secondary power	used to loosen tolerances on position of primary
secondary surface	chosen spherical, since shared
primary position	used to satisfy the sine condition
primary tilt	must direct axial rays to shared secondary mirror
primary power, shape	fixed at flat, so that gossamer mirrors can be used
tertiary position	chosen to make axial pathlengths equal
tertiary tilt	perpendicular to axial ray, for no added astigmatism
tertiary power	chosen to bring light to focus at system image plane
tertiary surface shape	toric, to correct for secondary's astigmatism
image plane location	chosen to be behind the secondary
image plane tilt	chosen as vertical, since it must be shared by all arms

TABLE 8.6. *The degrees of freedom used to satisfy the low-order beam combining requirements in the gossamer space telescope design.*

This leaves no degrees of freedom left to satisfy the low-order combining errors remaining: linear tilt errors and linear defocus errors. The focal lengths of the arms with different off-axis distances, C, will generally differ. This generates linear tilt errors, as the images move apart with field angle. Also, each arm will have its own focal plane that is tilted with respect to the system focal plane. This generates linear defocus errors.

These low-order errors will certainly dominate the system performance for small field angles. The image separation and defocus distances can be calculated geometrically, and the total RMS wavefront error for any system can easily be calculated. This leads to an easy method of estimating the system performance, without resorting to a full raytrace model of every system of interest.

Figure 8.10 shows the reference system with $C = 0$, and a general off-axis branch. The focal length of the reference branch is $-L$. The ideal image point in the system's image plane is then $-L\alpha$, where α is any field angle. For a general field angle, the image point from the general branch will move up its own, tilted image plane by $f_{arm}\alpha$. This leads to an image separation that is more complex than just $(L - f_{arm})\alpha$.

The beam separation distance is the distance between the reference system's image location and the location of the branch's chief ray in the system image plane. In the figure, this is shown as the distance between the blue and the black dots in the system image plane. The defocus distance is the distance between the branch's focal point and the point where the branch's chief ray intersects the system image plane. These points are shown by the two blue dots in the figure.

A symbolic raytrace was used to calculate β, shown in the figure, which is just the output angle of a ray input at a general field angle of α. Oblique power was used for the secondary, and all distances were measured along the axial ray of the branch. The length of the branch axis is known, as is the angle the axial ray makes with the system axis, ϕ. The image plane tilt, γ, was calculated using the Scheimpflug condition, discussed in Chapter 3. Then, triangle geometry was used to calculate the image separation and defocus distances.

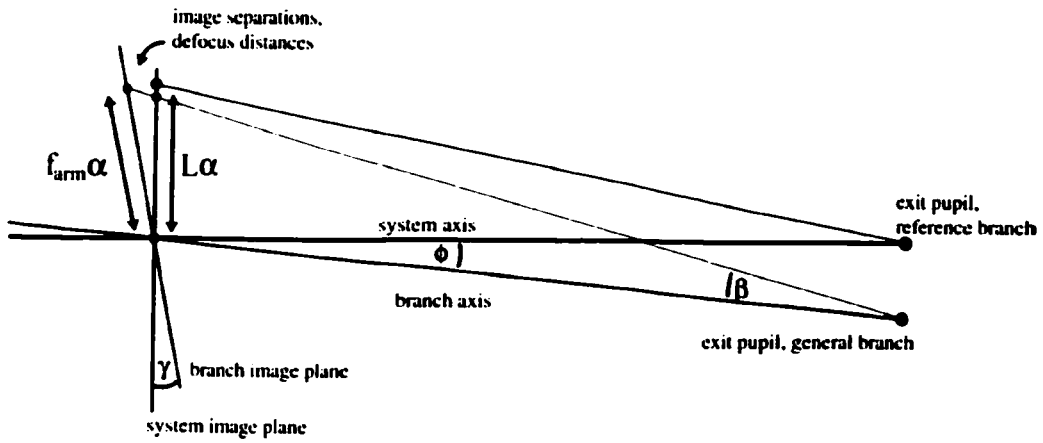

FIGURE 8.10. *Figure showing the reference branch and a general branch of the gossamer system. Linear tilt and defocus errors appear due to the tilted image plane and the mismatch in focal lengths.*

The parametric relationships are too complex to report in full here, but consider the example system discussed previously. The system length is 1000 meters and $M = 0.05$. Figure 8.11 shows γ, the tilt angle of the image plane, as a function of the height of the branch's primary flat, C. The rotations of the image plane are large because the low value of M produces steep tilt angles in the tertiary, and therefore steep tilt angles appear in the image plane.

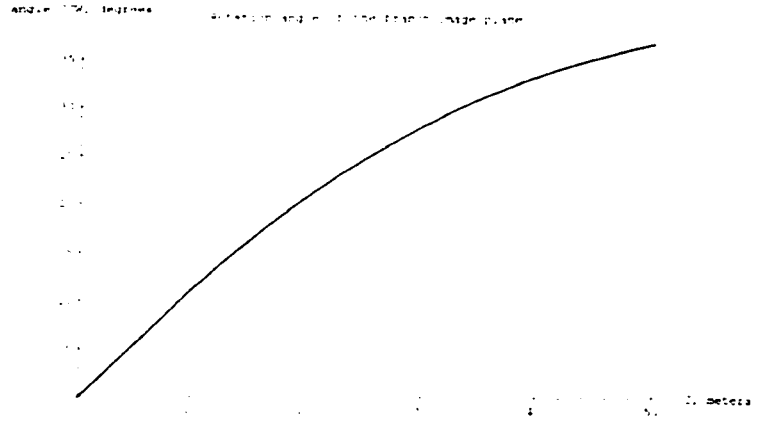

FIGURE 8.11. *The image plane angle for a branch of the multiple aperture system, where $L = 1000$ meters and $M = 0.05$, as a function of the height of the primary flat, C.*

The calculated image separations and defocus distances for this example system are shown in Figures 8.12 and 8.13. The wavelength was taken to be 500 nm. The plots show the values for flat heights of 15 m, 30 m, and 50 m.

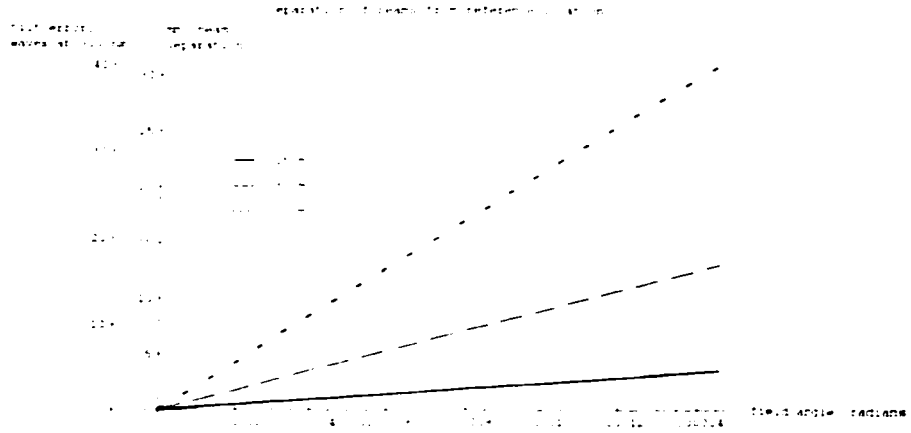

FIGURE 8.12. *The beam separation in mm and tilt errors in waves, for various heights of the primary flats.*

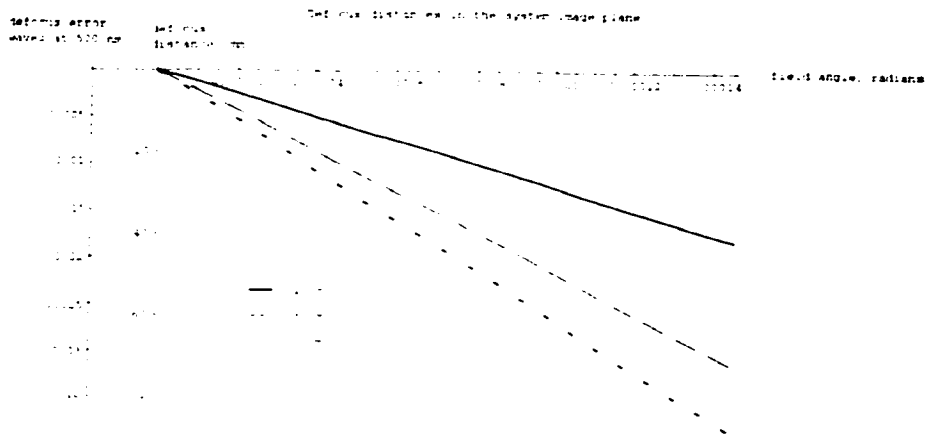

FIGURE 8.13. *The defocus distances and defocus errors in waves, for various heights of the primary flats, C.*

The tilt errors were calculated as waves of tilt at the edge of the aperture, for a given field angle. Let ψ be the difference between the angle the chief ray has and the angle the chief ray needs to have so that the images overlap. Then $\psi = \arctan(y/f_{arm}) - \arctan(y_o/f_{arm})$, where y_o is the reference image point, y is the height of the branch's chief ray in the image plane, and f_{arm} is the focal length of the branch. The image separation distances plotted in Figure 8.12 are equal to $y - y_o$. Recall that D is the diameter of the primary flat. The tilt wavefront error at the edge of the aperture, in waves, is then:

$$W_{111} = \frac{D}{2\lambda} \tan \psi \tag{8.10}$$

To convert the defocus distances to waves of defocus at the edge of the aperture in the exit pupil, let the defocus distance be δz. Then the defocus error in waves is:[33]

$$W_{020} = \frac{\delta z \cdot D}{8\lambda f_{arm}} \tag{8.11}$$

In the defocus values plotted in Figure 8.13, $D = 1$ and $\lambda = 500$ nm.

8.6 Total RMS values

The wavefront coefficients above can be calculated for every branch in the total system. If properly combined, the total RMS for the system will result. This gives an easy way to estimate the system performance for many systems without the need for a complete raytrace model.

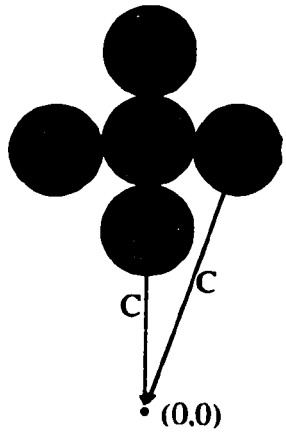

FIGURE 8.14. *Primary configuration of the five-flat systems studied, viewed in the x-y plane.*

Consider a system of five primary flats, as shown in Figure 8.14. The five arms share values of D, M, and L. The branches have primary flat heights of roughly $C, C-D$, and $C+D$. The values of W_{111} and W_{020} for each branch can be calculated using equations 8.10 and 8.11. The functional form of the wavefront error in the k^{th} aperture will be:

$$W_k = W_{111}^{(k)} \cdot \rho \cos\theta + W_{020}^{(k)} \cdot \rho^2 \tag{8.12}$$

where $\rho = \frac{r}{D}$ is the normalized pupil coordinate. The polar position $r \cdot \cos\theta$ specifies a given point in the pupil.

In general, if there are multiple branches in the system, the wavefront variance for the whole system of apertures will be a sum of the individual wavefront variances,

weighted by the areas of each aperture, A_k:

$$RMS = \sigma \tag{8.13}$$

$$\sigma^2 = \frac{\sum A_k \cdot \sigma_k^2}{\sum A_k} \tag{8.14}$$

and the RMS wavefront error is the square root of the variance. The wavefront variance of an individual aperture is:

$$\sigma_k^2 = \frac{1}{A_k} \iint_{A_k} (W_k - \langle W \rangle)^2 \delta A_k \tag{8.15}$$

where $\langle W \rangle$ is the average wavefront over the whole system, and $\langle W_k \rangle$ is the average wavefront in the kth aperture.

$$\langle W \rangle = \frac{\sum A_k \langle W_k \rangle}{\sum A_k} \tag{8.16}$$

$$\langle W_k \rangle = \frac{\iint W_k \cdot \delta A_k}{A_k} \tag{8.17}$$

In the specific case of the five-flat system, the wavefront error in each aperture is given by equation 8.12. Since three of the flats have center heights of roughly C, three of the W_k values are the same: $W_1 \approx W_2 \approx W_3$. The average wavefront in the k^{th} aperture is:

$$\langle W_k \rangle = \frac{1}{2} W_{020}^{(k)} \tag{8.18}$$

and $\langle W_1 \rangle = \langle W_2 \rangle = \langle W_3 \rangle$. The average wavefront in the whole system is the weighted sum of the individual averages:

$$\begin{aligned} \langle W \rangle &= \frac{A_1 \langle W_1 \rangle + A_2 \langle W_2 \rangle + A_3 \langle W_3 \rangle + A_4 \langle W_4 \rangle + A_5 \langle W_5 \rangle}{A_1 + A_2 + A_3 + A_4 + A_5} \\ &= \frac{1}{10} \left(3 \cdot W_{020}^{(1)} + W_{020}^{(4)} + W_{020}^{(5)} \right) \end{aligned} \tag{8.19}$$

since all the aperture areas are equal. Then the wavefront variance in the individual apertures is:

$$\sigma_k^2 = \frac{1}{\pi} \int_0^1 \int_0^{2\pi} \left(W_k - \frac{1}{10} \left[3 \cdot W_{020}^{(1)} + W_{020}^{(4)} + W_{020}^{(5)} \right] \right)^2 \rho \cdot \delta\theta \cdot \delta\rho. \tag{8.20}$$

and finally, the total wavefront variance will be:

$$\sigma^2 = \frac{1}{5}\left(3\sigma_1^2 + \sigma_4^2 + \sigma_5^2\right).$$

For an example case with $L = 1000$ meters, $M = 0.2$, $C = 15$ m, and $D = 1$ meter, the individual and total RMS wavefront errors for the five-flat system are shown in Figure 8.15.

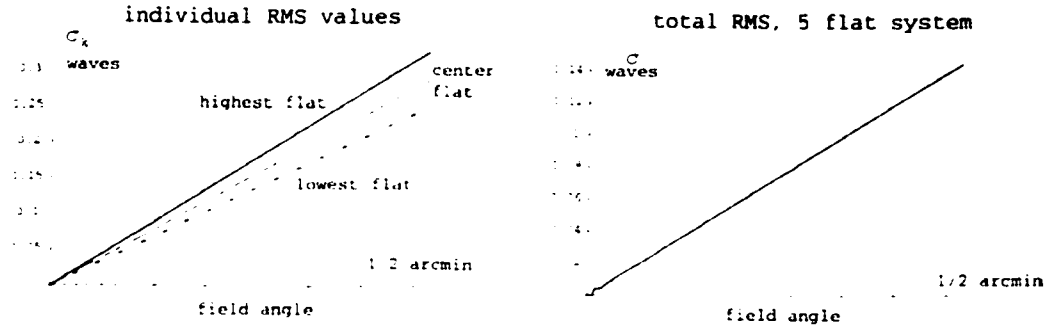

FIGURE 8.15. *Individual and total RMS wavefront errors for a five flat system.*

8.7 Comparison to a full raytrace model

Full raytrace models of several of the five-flat systems were created. They confirmed that the wavefront reconstruction accurately predicted wavefront errors for these systems and confirmed that the tilt errors dominated the system performance. The raytrace models also confirmed that the sine condition had been correctly satisfied, that the image plane tilts matched those predicted, and that the on-axis focal points overlapped. The model was carried out in Optima, a proprietary code provided by Lockheed-Martin. The code uses nonsequential raytracing to produce an interferometrically combined image plane.

The specifications for the five arms of the system were set to the values given in Table 8.4. The tertiaries were initially set to the toric values given. Then, Zernike terms were placed on the tertiaries so that the system performance was perfect at

zero field angle. The conic values in x and y on the tertiaries were also changed. The on-axis performance of all the flats was dominated by the Zernike term (3,1), which is related to third order coma, W_{131}. Small amounts of astigmatism and spherical were also corrected for. The flats to the right and left of center were slightly rotated about the z-axis, and so had a small amount of coma in the x-direction which was corrected with the Zernike term (3,2).

Figure 8.16 shows an Optima plot of the five-flat system discussed above. The scale in the z-direction has been compressed so that details in the y-direction are visible.

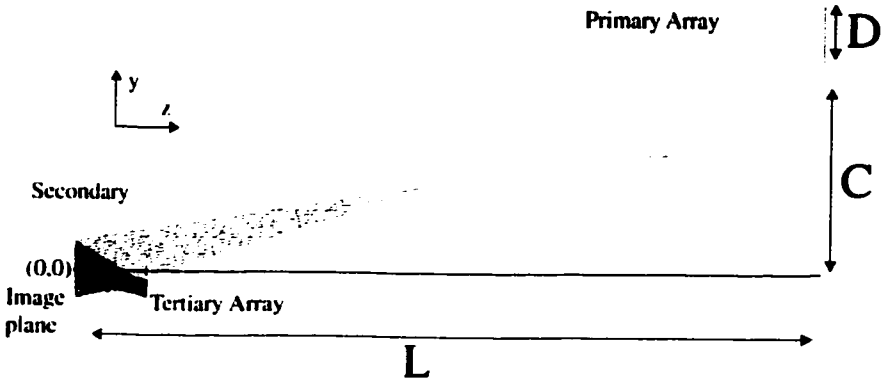

FIGURE 8.16. *A raytrace of the five-flat system, produced by Optima.*

Figure 8.17 shows wave fans in the y-z plane for increasing field angles. Tilt is the dominant aberration, indicating that the wavefront reconstruction method will be very accurate in predicting the systems' RMS wavefront errors. These wave fans were calculated for a system where $L = 1000$ meters, $C = 15$ meters, $M = 0.05$, and $D = 1$ meter.

Figure 8.18 shows the three-dimensional OPD in the exit pupil of the same five flat system, at a field angle of 0.25 arcminutes.

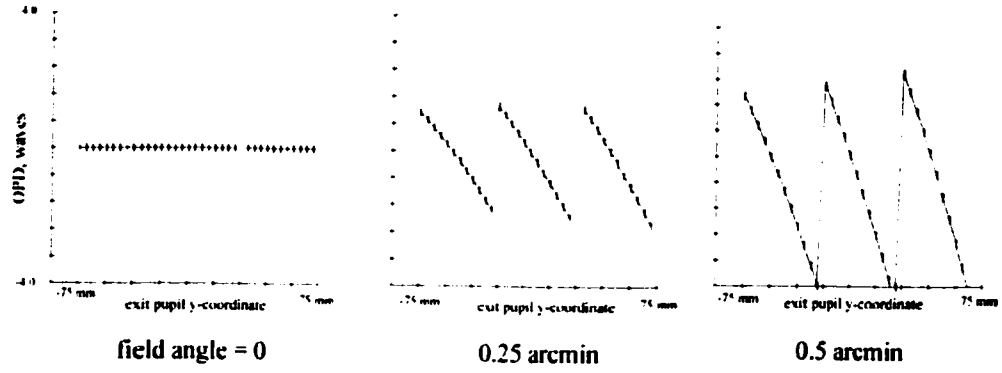

FIGURE 8.17. *Wave fans showing tilt errors that are linear as a function of field.*

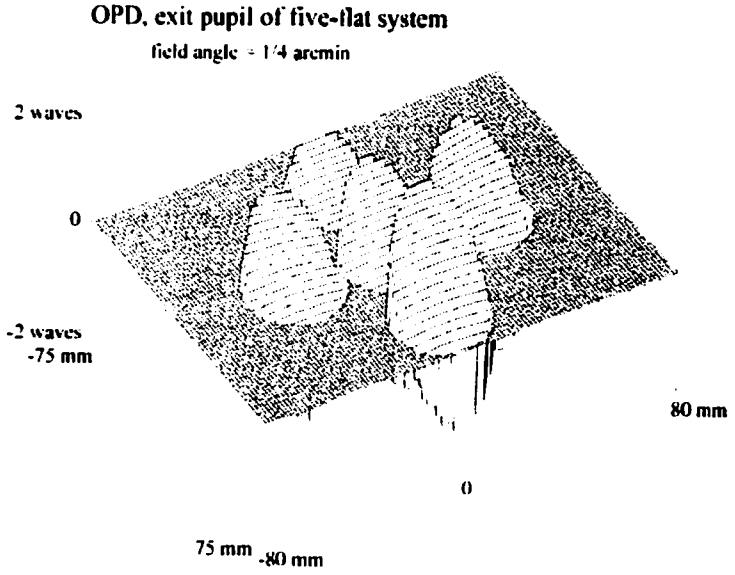

FIGURE 8.18. *The OPD in the exit pupil of a five-flat system, at a field angle of 0.25 arcminutes. L=1000, C=15, M=0.05, and D=1.*

Figure 8.19 confirms that the sine condition for the system has been satisfied. Measuring the OPD of the axial ray as a function of field angle gives a quadratic curve that is horizontal at the center, indicating that the linear component of the piston error has been removed.

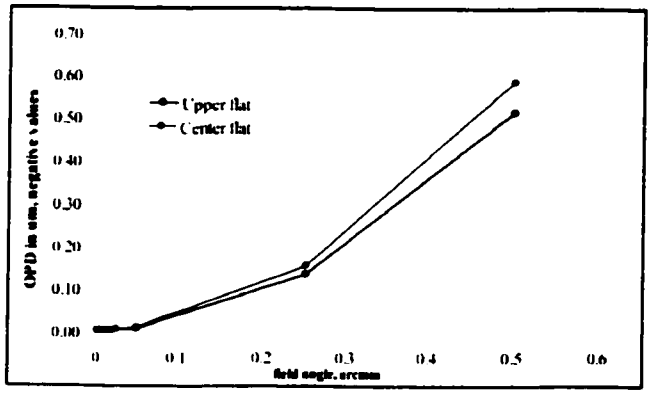

FIGURE 8.19. *A plot of the OPD for the axial rays in the system, with repect to the axial OPL for an on-axis branch. The values shown are negative OPDs; as the primary flat moves off axis, the OPL through the system gets shorter.*

Figure 8.20 shows comparisons of the RMS values from the raytrace model and the RMS values predicted by the wavefront reconstruction process described above. The agreement is very good, as it was for the other systems checked in this way.

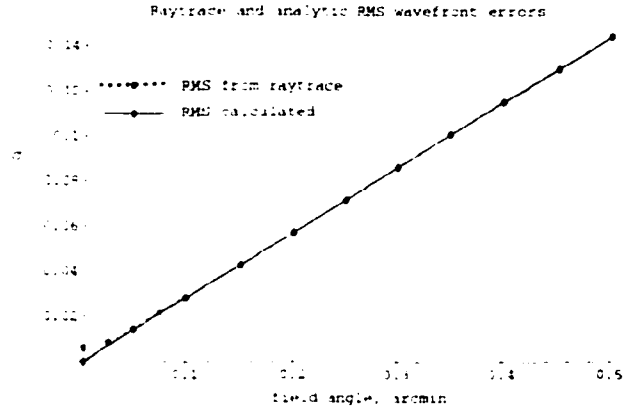

FIGURE 8.20. *RMS values from the raytrace model and calculated analytically, for the example case of* $L = 1000$, $M = 0.05$, $C = 15$, *and* $D = 1$ *meter.*

8.8 A note on the tertiary powers

Since the wave fans shown in Figure 8.17 are dominated by tilt, which is separation of the individual images in the image plane, it is tempting to think that the images can be forced to stay together as a function of field. In fact, this is the case, but it does not lead to better system performance.

The tertiary powers in the systems described above were chosen so that the vertices of all the focal planes overlapped, as shown in Figure 8.10. Alternatively, the focal lengths of the tertiaries could be chosen to force the images to overlap. This would result in the image planes being offset from one another in z, as shown in Figure 8.21. That is equivalent to a constant defocus error being introduced into the system, in exchange for eliminating the linear tilt errors.

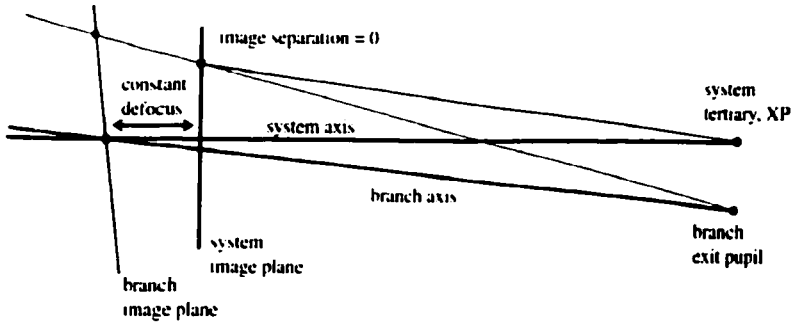

FIGURE 8.21. *The tertiary power can be chosen to force the image planes to overlap. But this introduces constant defocus errors.*

The tertiary powers necessary to force the images to overlap were calculated for the case of $L = 1000$ meters, $M = 0.1$, $C = 15$ meters, and $D = 1$ meter. For this case, the tertiary focal lengths that were required were 4.5, 8.4, and 12.2 meters, for the upper, center, and lower tertiaries of the five flat systems. For the focal plane vertices to overlap, on the other hand, the required tertiary focal lengths were 8.33, 8.39, and 8.56 meters. This indicates that the constant defocus introduced will be on the order of meters, which was confirmed to be the case. The defocus errors were

so large that the system performance was poor even at zero field angle.

This is a logical result. Since the tertiaries are very close to the exit pupils in the system, the axial and chief rays will have nearly zero height at the tertiary mirror. Adjusting the power, then, has little effect on the output angle of the chief ray.

8.9 Exploring design space

The analytic calculation of the RMS wavefront errors is an easy way to estimate the fields of view for a large number of systems. The FOV is calculated by choosing a maximum acceptable RMS wavefront error and solving for the field angle that corresponds to that RMS. In this case, an RMS of 0.1 will be chosen as the maximum tolerable wavefront error.

There are four parameters in the system: the height of the primary flat, C, the length of the system, L, the demagnification of the primary to the secondary, M, and the diameter of the primary flats, D. Sampling three values of each parameter gives a total of 81 data points in the design space. The values for each parameter that were explored are:

D	primary flat diameter	1 m	2 m	5 m
M	magnification of the secondary	0.2	0.1	0.05
L	length of the system	1000 m	750 m	500 m
C	height of center flat	15 m	30 m	50 m

TABLE 8.7. *Parameter values used to explore the design space of the five-flat gossamer systems.*

The flat diameters are limited by the tertiary diameters, as well as fabrication techniques and rocket shroud sizes. The tertiary mirrors are traditional glass mirrors and must be small and easy to handle. Assuming that the largest acceptable tertiary would be 1 meter in diameter, this limits the flat diameters to 5 meters or less for the magnifications chosen. Longer system lengths mean weaker primary arrays and

thus better performance, and 1 km seems to be the largest system we can conceive of controlling at this time. The maximum off-axis distance for the center primary, C, was set at 50 meters, since this would mean a 100 meter baseline if more branches were added to the system. It is also probably the largest baseline that could be supported with enough rigidity on a single mechanical structure.

The systems with the best performance, then, will have the parameter values shown in the first column of Table 8.7 - the smallest flat diameters, largest magnification, longest length, and shortest distance off-axis. The worst performance will be the fastest system, with parameters all taken from the last column of Table 8.7

The fields of view at $\lambda = 500$ nm are shown in Figure 8.22. As expected, the largest field of view is for the system with $(D = 1, M = 0.2, L = 1000, C = 15)$, for a system f/# of 333. The field of view for that system is 0.7 arcminutes. The smallest field of view is for the system with $(D = 5, M = 0.05, L = 500, C = 50)$, for a system f/# of 33.3, and a field of view of 0.0002 arcminutes. This field is obviously too small to be useful.

All of the fields of view shown in Figure 8.22 are plotted as a function of C. The performance decreases for larger values of C because the separation of the individual images increases as the height of the primary flat does. The performance appears to fall off quadratically with C in all cases, but because the parameters are not independent of one another, the speed of the fall-off is determined by the other parameters in the system.

Figure 8.23 shows some of the same data, but plotted as a function of D, the diameters of the primary flats. The fields of view in the five-flat systems should decrease with increasing D because the upper and lower flats move further from the system axis as the flat diameters increase. The parameters C and D are linked in this way in the five-flat systems. In a single arm, though, increasing D would not affect the performance of the system much, since changing D does not change the image separation that dominates the system performance. Again, the fields of view

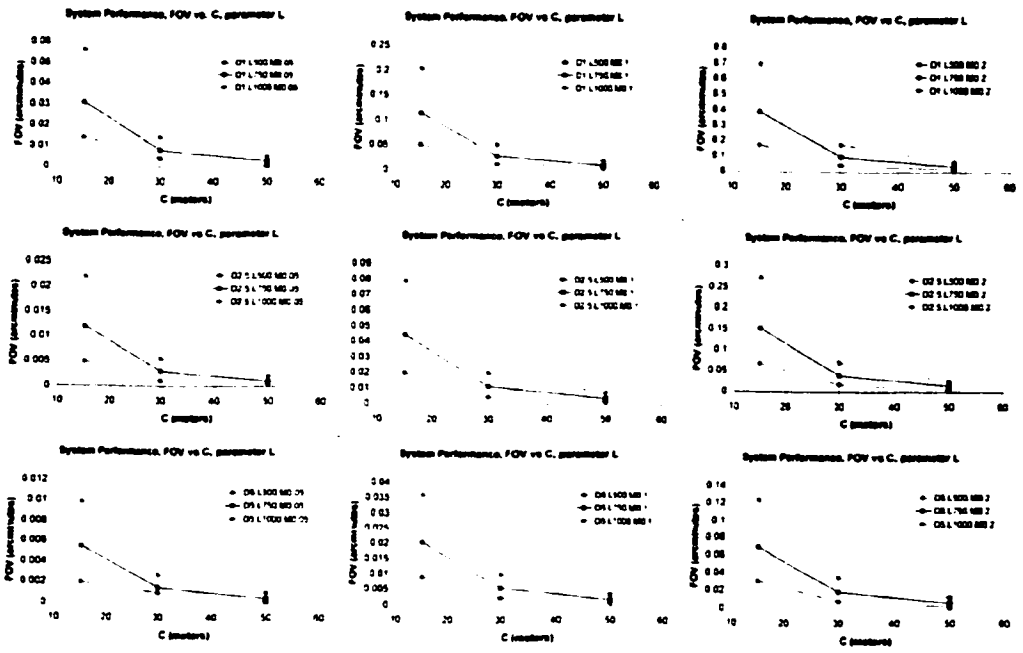

FIGURE 8.22. *Field of view data for the five-flat gossamer systems.*

seem to fall off quadratically with D, as would be expected since performance also falls off quadratically with C.

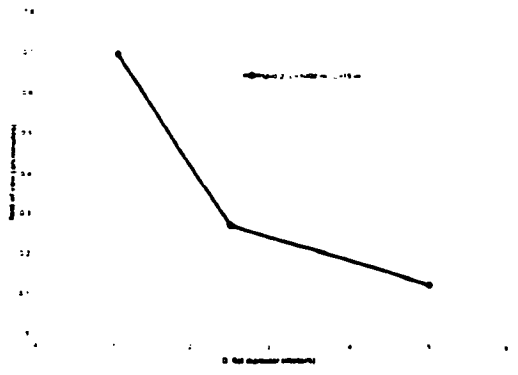

FIGURE 8.23. *Fields of view as a function of flat diameter, for the case where M=0.2, L=1000 m, and C=15 m.*

Figure 8.24 shows fields of view plotted as a function of L. The fields of view

should decrease with decreasing values of L, since longer systems are weaker and therefore have better performance. The figure shows that the performance increases linearly with L.

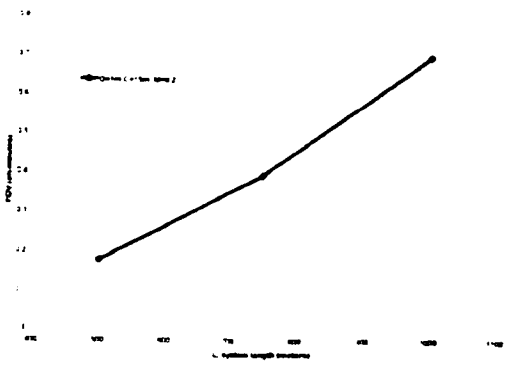

FIGURE 8.24. *Fields of view in a five-flat system, as a function of the system length, L. The system shown has M=0.2, C=15 m, and D=1 m.*

Finally, Figure 8.25 shows some of the fields of view plotted as a function of M, the demagnification between the primary and tertiary arrays. The fields of view should decrease with decreasing values of M. Small values of M correspond to steeply tilted individual image planes. This forces the image separations to be large. The figure shows that the performance increases dramatically as M increases.

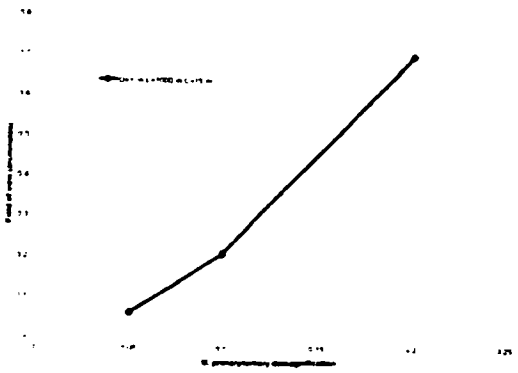

FIGURE 8.25. *Fields of view for a five-flat system, as a function of M. The system shown has L=1000 m, C = 15 m, and D = 1 m.*

8.10 Conclusions

To complement a technology development of flat gossamer mirrors, a space telescope design was investigated that uses an array of flat mirrors in place of a continuous primary. The system would consist of a primary array of flats, a shared secondary mirror, and a tertiary array with one mirror corresponding to each of the primary flats. To ease the tolerances on the primary flats, the secondary images the primary array onto the tertiary array. The tertiary array can then be used to correct for any mispositionings in the primary flat.

Each branch of the system consists of a primary flat, the shared secondary, and a tertiary that brings the beam to the correct image point. The secondary is used at an oblique angle, so the tertiary surface shape must be toric to correct for the astigmatism introduced by the secondary. The constant piston errors are eliminated by placing the tertiary so that the axial pathlengths in all branches are equal. Constant tilt errors are eliminated by choosing the correct orientation of the tertiary mirror. The linear piston errors are satisfied if the primary flats are all located on a spherical surface of radius L, equal to the total length of the telescope system. Constant defocus

errors are eliminated by forcing the focal planes to overlap. The focal lengths of each branch do not match, then, and the linear tilt errors that result dominate the system's performance. Linear defocus errors are present because the individual focal planes are rotated with respect to the system's image plane. The linear defocus errors are much smaller than the dominant tilt errors.

The RMS wavefront error is easily calculated as a function of the system parameters. This allows an efficient method for exploring design space for these systems. The performance of a system of five flats is explored in this way. A few specific five-flat systems were modeled with full interferometric raytraces, and the results show good agreement with the Strehl values predicted by calculation of the RMS wavefront errors.

The five-flat gossamer systems studied here have adequate fields of view for planet imaging, where baselines of 100 meters but only a few arcseconds of field are necessary. The highest FOV for a system of five flats was 0.7 arcminutes, for a system that was 1000 meters long, 15 meters off-axis, with 1 meter flat diameters, and primary-to-tertiary demagnification of 0.2. The sensitivity of this system will be inadequate for planet imaging, though, and designs with many more flats need to be explored.

Chapter 9

CONCLUDING REMARKS

9.1 Summary

Ground-based interferometric telescopes have demonstrated large gains in resolution and sensitivity over single-aperture telescopes. Such gains are imminent in space, as well. Designers for these systems are needed, and this dissertation deals with the optical design of wide-field interferometers. Wide-field interferometers create an image of an object convolved with the PSF of the interferometer. This is unlike Michelson stellar interferometers, which reconstruct the image by measuring visibility as a function of baseline length. The Multiple Mirror Telescope in Tucson, Arizona, was the first telescope to demonstrate wide-field imaging. The Large Binocular Telescope will be the first to routinely operate in wide-field imaging mode.

9.1.1 Basics

The point spread function (PSF) of a multiple aperture system is the sum of an image from each aperture and a set of fringes from each pair of apertures. The fringes cause the PSF to be narrower than the PSF of a single aperture. This leads to better resolution in the system, since the two-point resolution is equal to the width of the central peak in the PSF.

The fill factor for a multiple aperture system compares the collection area to the collection area of a single-aperture telescope of the same diameter. A high fill factor indicates relatively large apertures on short baselines. As the fill factor decreases, the number of fringes in the PSF with significant amplitudes increases. For wide-field imaging, these side-lobes act as background noise, and are not useful.

The polychromatic PSF will have a visibility envelope associated with it. The

visibility envelope is proportional to the Fourier transform of the object's spectrum. If the fill factor of the system is high, though, the diffraction envelope may be so narrow that the visibility loss in the fringes is not observed.

The optical transfer function (OTF) of a multiple aperture system has a peak corresponding to every different baseline in the system. A two-aperture system on a baseline of Δ will have good transmission at three frequencies: $0, -\Delta/(2f\lambda)$, and $+\Delta/(2f\lambda)$. A multiple aperture system will have $(2n+1)$ different baselines, where n is the number of differing baselines in the system. Redundant baselines will increase the height of the corresponding OTF peak, giving better transmission of that spatial frequency.

A high fill factor indicates that the frequencies between the peaks in the OTF will also have good transmission efficiency: the OTF will be "plump".

Sensitivity in a multiple aperture system is proportional to collecting area of the telescope. A calculation of sensitivity accounts for the characteristics and noise sources of the telescope, instrument, and detector used.

9.1.2 Errors

The perfect image is the sum of an image from each aperture and a set of fringes from each pair of apertures. For this image to remain perfect over a wide field of view, three things must happen: the images from each aperture must stay together, the images must combine coherently, and the images from each aperture must be high in quality. Loss of coherent imaging is caused by piston errors in the wave fans. Lateral image separations are caused by tilt errors in the wavefront, and longitudinal image separations are caused by power errors in the wavefront. Aberrations in the individual images always cause deterioration of the combined image, and matching the aberration coefficients in the individual arms does not improve the combined image.

For a two aperture system with large piston errors, the Strehl ratio will fall to 1/2. The images from each aperture overlap but do not combine coherently. For large tilt and defocus errors, though, the Strehl will fall to 1/4. This is the height of a single aperture's image compared to the height of the combined image. For other aberrations in the individual arms, the Strehl can fall to 0.

9.1.3 Preventing the errors

Any of the beam combining errors (piston, tilt, and defocus) can occur as any function of field angle. The constant and linear errors have straightforward geometric explanations.

Constant piston errors occur when the axial pathlengths in each arm at zero field angle are not equal. The mirror positions in each arm can be adjusted to prevent this error. Linear piston errors occur when the Abbe sine condition for the axial rays in the system is violated. In an afocal system, this error is prevented if the exit pupil beam diameters and separations are equal to the beam diameters and separations in the entrance pupil, multiplied by a scaling factor. In other systems, the error can be prevented by satisfying the Abbe sine condition directly.

Constant tilt error is just a pointing error in the associated arm of the telescope. This can be prevented by adjusting the orientation of the optics in the arm. Linear tilt errors occur when the focal lengths of each arm in the system are not equal. The power of each arm can be adjusted to force the focal lengths to be equal.

Constant defocus errors occur if the image plane from a given arm is offset from the system's focal plane. Again, the power of each arm can be adjusted to force the focal planes to overlap. This may conflict with the above requirement that the focal lengths of each arm are equal. Linear defocus errors occur when the branch's focal plane is tilted with respect to the system's image plane. The image plane tilts can be calculated with the Scheimpflug condition. Image plane tilt in a general system

can be corrected with a single off-axis mirror.

9.1.4 Predicting system performance

There may not be enough degrees of freedom in a given design to satisfy all of the above requirements simultaneously. The effect of each error on the system's performance should be calculated so that the worst errors can be corrected first. This can be done using plane-symmetric aberration theory, since the majority of multiple aperture systems use branches with one plane of symmetry.

The wavefront error in the presence of a constant piston error will have the form W_{00000}. Linear piston is $W_{10010}H\cos\phi$. Constant tilt has the form $W_{01001}\rho\cos\theta$, and linear tilt errors are $W_{11100}H\rho\cos\theta$. Constant defocus is $W_{02000}\rho^2$, and linear defocus errors are given by $W_{12010}H\rho^2\cos\phi$. The values of each of these coefficients can be calculated, as shown in Chapter 4. Then, the RMS wavefront error for the system can be calculated and the Strehl ratio of the system predicted. This avoids the difficult task of carrying out a full interferometric raytrace model of the system in the early stages of the design process.

The RMS wavefront error calculation is invalid for piston errors in sparse two-aperture and sparse, nonlinear three-aperture configurations. In these cases, the performance will be good if the piston errors are much less than the coherence length, independent of the RMS wavefront error. For systems with fill factors of up to 0.5 or piston errors on the order of the coherence length in the system, direct calculation of the polychromatic PSF and Strehl of the system is necessary. For all other configurations, the RMS wavefront error calculation is valid.

9.1.5 Higher-order errors

Tilt errors that are quadratic and cubic with field angle can occur in multiple aperture systems. Cubic tilt errors are also known as distortion. Since distortion is

rotationally-symmetric, it may be possible to allow equal amounts of distortion in each arm of a multiple aperture system. The images will still overlap as a function of field angle. However, the sine condition may need to be modified so that the images still combine coherently.

Quadratic tilt errors have no requirement of rotational symmetry. Then, using identical arms with quadratic distortion present will cause image separation. This problem has been called "differential distortion".

Defocus errors that are quadratic as a function of field angle can also occur. This effect appears when the field curvatures in each arm are unequal. Quadratic, cubic, and quartic piston errors also appear in plane-symmetric systems. All of these are errors that may be permissible in certain cases, since a perfect image could be regained through post-processing of the image.

9.1.6 Aberration theory derivation of the design rules

By comparing an off-axis piece of a perfect wavefront to a general plane-symmetric wavefront, design rules for branches of multiple aperture systems were derived. Constraints on the wavefront coefficients in a plane symmetric system were given, and agree well with the low-order design rules discussed in Chapter 4. The constraints also suggest that quadratic piston can be corrected, and that field curvature and distortions in arms of multiple aperture systems may still lead to good beam combining under certain conditions.

9.1.7 Two 100-meter baseline designs

Two systems with 100 meter baselines were compared. Both systems had the same f/#, aperture diameters, and aperture separations.

The first system was a rotationally-symmetric Paul system that was then segmented to make a four-aperture system. The low-order design rules in this system

were shown to be automatically satisfied. This is logical, since the parent system can have no beam combining errors.

The second system was an array of four afocal telescopes that share a three-mirror combining telescope. Fold flats were used in the inner two arms to satisfy the requirement that the axial pathlengths should match. Linear piston errors were eliminated by forcing the beam configuration into the combiner to be a scaled version of the afocal array. The angles of the fold flats were chosen so that there were no pointing errors in the system. The focal lengths of each arm were all equal to the focal length of the combining system, since the collection telescopes have zero power. Because the combining optics are shared, there were no defocus errors due to focal plane offsets or tilts.

The Paul system gave a larger field of view than the afocal array system, and used fewer reflections per arm of the system (which is especially important in the IR regime). The Paul system is also a very large system (200x100m), while the afocal array system is relatively compact (20x100m). The lack of afocal beams anywhere in the Paul system means that pathlength adjustment may be difficult, while the fold mirrors in the afocal system allow straightforward correction of axial pathlength errors. The tolerances on the mirrors in the Paul system were much tighter than the tolerances on the afocal system. Also, the mirrors for the Paul system were off-axis conics, which will be more difficult and expensive to fabricate than the rotationally-symmetric optics in the afocal system.

9.1.8 The Large Binocular Telescope

The Large Binocular Telescope illustrates a design that has only planar symmetry. A coherent image with a wide field of view is achieved with just three reflections, only one of which is powered. This could not have been done by relying on more axially-symmetric designs.

The behavior of the LBT beam combiner illustrates some of the errors expected in a plane-symmetric system. Astigmatism is the limiting aberration, and could be corrected if necessary with a toric surface on one of the fold flats in each arm. Linear defocus errors also appear, but are minimized by bringing the beams to focus as closely together as possible. The constant piston, tilt, and defocus errors are all zero, since the two arms in the system are mirror-images of one another. This leads to differential distortion in the system, though. The sine condition is satisfied so that the linear piston errors are zero. A small amount of quadratic piston remains in the system.

An estimate of the tolerances was calculated by plotting the Strehl ratio at zero field angle for the system in the presence of low order aberrations (piston, tilts, and defocus). Assuming that the errors should initially be equally divided among the mirrors, the tolerances on each mirror's position and power were estimated. The results indicate that active control on one of the mirrors in the beam combiner will be needed.

9.1.9 Gossamer space telescope

To complement a technology development of flat gossamer mirrors, a space telescope design was investigated that uses an array of flat mirrors in place of a continuous primary. The system would consist of a primary array of flats, a shared secondary mirror, and a tertiary array with one mirror corresponding to each of the primary flats. To ease the tolerances on the primary flats, the secondary images the primary array onto the tertiary array. The tertiary array can then be used to correct for any mispositionings in the primary flat.

Each branch of the system consists of a primary flat, the shared secondary, and a tertiary that brings the beam to the correct image point. The secondary is used at an oblique angle, so the tertiary surface shape must be toric to correct for the astigmatism

introduced by the secondary. The constant piston errors are eliminated by placing the tertiary so that the axial pathlengths in all branches are equal. Constant tilt errors are eliminated by choosing the correct orientation of the tertiary mirror. The linear piston errors are satisfied if the primary flats are all located on a spherical surface of radius L, equal to the total length of the telescope system. Constant defocus errors are eliminated by forcing the focal planes to overlap. The focal lengths of each branch do not match, then, and the linear tilt errors that result dominate the system's performance. Linear defocus errors are present because the individual focal planes are rotated with respect to the system's image plane. The linear defocus errors are much smaller than the dominant tilt errors.

The RMS wavefront error is easily calculated as a function of the system parameters. This allows an efficient method for exploring design space for these systems. The performance of a system of five flats is explored in this way. A few specific five-flat systems were modeled with full interferometric raytraces, and the results show good agreement with the Strehl values predicted by calculation of the RMS wavefront errors.

The five-flat gossamer systems studied here attain more than enough field for planet imaging, where baselines of 100 meters but only a few arcseconds of field are needed. The highest FOV for a system of five flats was 0.7 arcminutes, for a system that was 1000 meters long and 15 meters off-axis, with 1 meter flat diameters, and primary-to-tertiary demagnification of 0.2. The sensitivity of this system will be inadequate for planet imaging, though, and designs with many more flats need to be explored.

9.2 Future Work

The physical origin of quadratic piston errors needs to be established, and a simple technique for its correction. There is a Hamiltonian derivation that demonstrates

the correction of errors quadratic in field which may lead to useful results if applied to multiple aperture systems.[42] Further work also needs to be done to find out if there are special cases in which field curvature and distortion errors can be tolerated. In cases where equal amounts of rotationally-symmetric distortion are present, the sine condition needs to be adjusted so that linear piston errors are eliminated at the distorted image locations.

Nonsequential raytrace routines in the current software packages still need some improvement, since bugs exist in several of the packages. Global coordinate entry must be standard. In addition, it should be possible to decompose any wavefront onto the set of plane-symmetric aberrations. Most raytrace programs have routines that do this for rotationally-symmetric systems.

Appendix A

TOOLS AND EXAMPLE PROGRAMS

The work in this dissertation was done with several tools. Mathematica was used for diffraction analysis, calculating images in the Fraunhofer regime assuming that all the optics in the system were perfect or had low-order errors. Mathematica can handle both numeric and symbolic calculations, and proved to be extremely useful. Beam propagation problems were done with IDL.

Raytrace programs handle multiple aperture systems in two possible ways: as a nonsequential raytrace (meaning that the light doesn't always travel from surface 1 to surface 2 to surface 3, etc.), or as a multiple configuration system. In the case of the multiple configurations, each arm of the multiple aperture system is entered as a separate lens system, and the user must tell the program exactly how to carry out the interference. This method is sometimes convenient, but because all the arms in a system are not plotted together, it can be easy to miss vignetting problems and situations where elements run into one another. It is also complicated to move one element with respect to another for tolerancing purposes. With nonsequential modeling, all elements are plotted simultaneously, and the raytrace program calculates the beam paths as a function of where the elements are in space.

Nonsequential raytracing was used almost exclusively for the work in this dissertation. Optima and Zemax were primarily used, and CodeV was used to a lesser extent. ASAP and other programs used for stray-light analysis were tempting because they were designed from the ground up to handle nonsequential systems. They don't include optimization routines at present, though, and thus were only useful for checking systems after the design work had already been done.

All of the standard raytrace programs are capable of nonsequential modeling.

There are some minor differences, but the selection of a program is mostly a matter of personal preference.

Optima is a proprietary program written at Lockheed Martin. Alice Palmer provided the program and support. It has some features that make it convenient for multiple aperture systems. The most important of these features is that it allows entry of lens positions and tilts in global coordinates, which is crucial in complicated mirror systems. The program is free to students, with permission from Lockheed. The on-line manual is good, and the technical support is directly from the programmers. Operation is all command-line, with commands very similar to CodeV. The macro language is obvious and easy to use. Plots are not interactive, but can be scaled differently in x and y, which is very useful for systems with non-standard aspect ratios. There is no default merit function, so it can take some time to create and save a good set of your own. Finally, the program gets confused about the f/# and exit pupil locations for a multiple aperture system, and these have to be entered manually.

Zemax now also has adequate nonsequential capabilities. The GUI in Zemax is the easiest to use of any of the raytrace programs. For multiple aperture systems, though, it still has a few problems. Variables set in the "Nonsequential Components" editor seem to be ignored. There is no global entry for the lens positions, tilts, etc. Worse, the global coordinates of the elements can be listed, but the list doesn't include lenses in a nonsequential region. These two problems make entering a complex lens system more difficult than it needs to be. The manual on nonsequential systems is not good. Tech support has 1 to 2 days' response time. The macro language is cumbersome, since it must be done in C and compiled before use. The optimization routines are easy to create. Not all surface types can be used in nonsequential regions. Zemax is the only one of the three raytrace programs discussed here that is not free to students.

In this chapter, a simple example system will be used to show how to enter a

multiple aperture system into each of the raytrace programs. The perfect image of a two-aperture system will also be demonstrated in Mathematica. These tutorials should decrease the time it takes a student to learn how to model multiple aperture systems.

A.1 Multiple aperture system example in Optima

As an example of how to use Optima (Version 25.04P, 8 March 2000) to model a multiple aperture system, consider the system shown in Figure A.1. Its specifications are given in Table A.1. The system consists of a pair of afocal, two-mirror telescopes. The afocal beams are fed into a single parabolic combiner. All the elements are parabolic mirrors. (The system violates the sine condition horribly, by the way. To satisfy it, flat mirrors would have to be used to bring the afocal beams closer together before they entered the combiner. The ratio of the beam diameters to their separation must be equal to that of the pair of primary mirrors.)

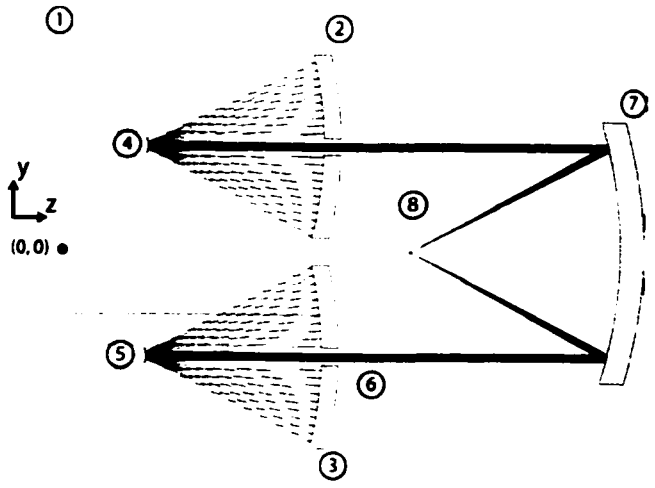

FIGURE A.1. *A simple two-aperture system, that will be used as an example in the raytrace programs.*

After opening Optima, a window titled "Console" will appear. The command

surface	y	z	radius	conic	outer diameter	inner diameter
1	0	0	—	—	7.5	—
2	2	5	-7	-1	3.5	0.3
3	-2	5	-7	-1	3.5	0.3
4	2	1.64	-0.28	-1	0.3	—
5	-2	1.64	-0.28	-1	0.3	—
6	0	5.64	—	—	5.4	0.52
7	0	10.64	-8	-1	5.0	—
8	0	6.64	—	—	0.5	—

TABLE A.1. *Specifications for the two-aperture example system.*

"init$$consol" will open a graphics console. Entering the list of commands below creates a simple two-aperture system. For more details on the commands, use Optima's help file, "Default.htm" in the Help directory of the Optima installation.

The simple two-aperture system shown in Figure A.1 can be entered into Optima with the list of commands shown below. They can be entered exactly as shown and in the order shown. To open a sub-file for data entry, name the lens, set the half-field of view in degrees, and set the lens units to meters:

lens example

li, example lens system

scy fang, 0.0083

units, meters

To enter a name for the object surface, set the distance to the next surface to 1e30 (nearly infinity), and set the surface to a dummy surface that doesn't affect the rays:

id, object

th, 1e30

air

Any command that refers to the material of the surface (such as *air, refl, Schott BK7*) also indicates that the data entry for that surface is completed. The next group of commands creates a dummy surface from which to begin the plots of the

system layout. The command "refs" tells the program that (0,0) of the coordinate system lies at the center of this surface. Also set the name, distance to next surface, semi-diameter, and material:

id, plot begin

th, 5

clap, 3.75

refs

air

Enter the data for the upper primary, including the surface name, radius of curvature, conic constant, clear aperture, and central obscuration:

id, primary A

rd, -7

cc, -1

clap, 1.75

cobs, 0.15

Set the tilts of this primary to zero by using the *dar* command. This also tells the program to return the coordinates to their original state after any tilt or decenter of this surface. Then, decenter the mirror, set the distance to the next surface (the second primary) to zero, and set the material to *refl* to indicate the surface is a mirror:

dar, 0 0 0

dec, 2 0

th, 0

refl

The data for the lower primary is very similar. The thickness describes the distance from primary to secondary, and is negative.

id, primary B

rd, -7

cc, -1

clap, 1.75

cobs, 0.15

dar, 0 0 0

dec, -2 0

th, -3.36

refl

For the upper secondary:

id, secondary A

rd, -0.28

cc, -1

clap, 0.15

dar, 0 0 0

dec, 2 0

th, 0

refl

For the lower secondary:

id, secondary B

rd, -0.28

cc, -1

clap, 0.15

dar, 0 0 0

dec, -2 0

th, 4

refl

Enter a dummy surface after the secondaries, to use to prevent rays from passing through the system without touching any mirrors. This will also act as an exit port for the "nonsequential region" of the mirror system. Everything that follows will be sequential ray tracing.

id, nonseq out

clap, 2.7

cobs, 0.26

th, 5

air

Enter the data for the combining mirror:

id, combiner

rd, -8

cc, -1

clap, 2.5

th, -4

refl

To close the lens data entry subfile:

eos

Go back into the lens subfile to give a name and semi-diameter to the last surface, which the program automatically adds to any lens system, and then close the subfile.

update lens

chg,8

id, image

clap, 0.25

eos

To tell the program which lenses fall in the nonsequential raytracing region, begin with the first primary at surface number 2 and end with the exit port at surface number 6:

nonseq, 1 2 6

The chief ray will by default fall on (0,0) of the reference surface. In a multiple aperture system, that ray may not trace because there are no mirrors in front of it. To change the height of the chief ray to 76% of the height of the reference surface:

pm chief, 0.76

This command gives the mirrors some visual thickness, so that schematics of the system are easier to interpret:

refith

To plot the lens in the graphics window and add some rays:

plot lensyz, 0 0 1

rfp yz, 0 -1 1 51 1 4 -1 -1

The plot should look exactly like that in Figure A.1, without the surface numbers shown. To plot two wave fans and two spot diagrams in the graphics window:

plot mult,4

fob,0

yfan opd, 1 -1 1 -101

plot fan1, 1 6

fob,1

yfan opd, 1 -1 1 -101

plot fan1, 1 6

fob,0

spd, 1000

plot spd

fob, 1

spd, 1000

plot spd

The command *fob* stands for "fractional object point", and refers to the normalized field angle. In this case, *fob = 1* refers to the full half field angle of 0.0083 degrees. The result of these commands is shown in Figure A.2. The sine condition violation is very bad, as mentioned above.

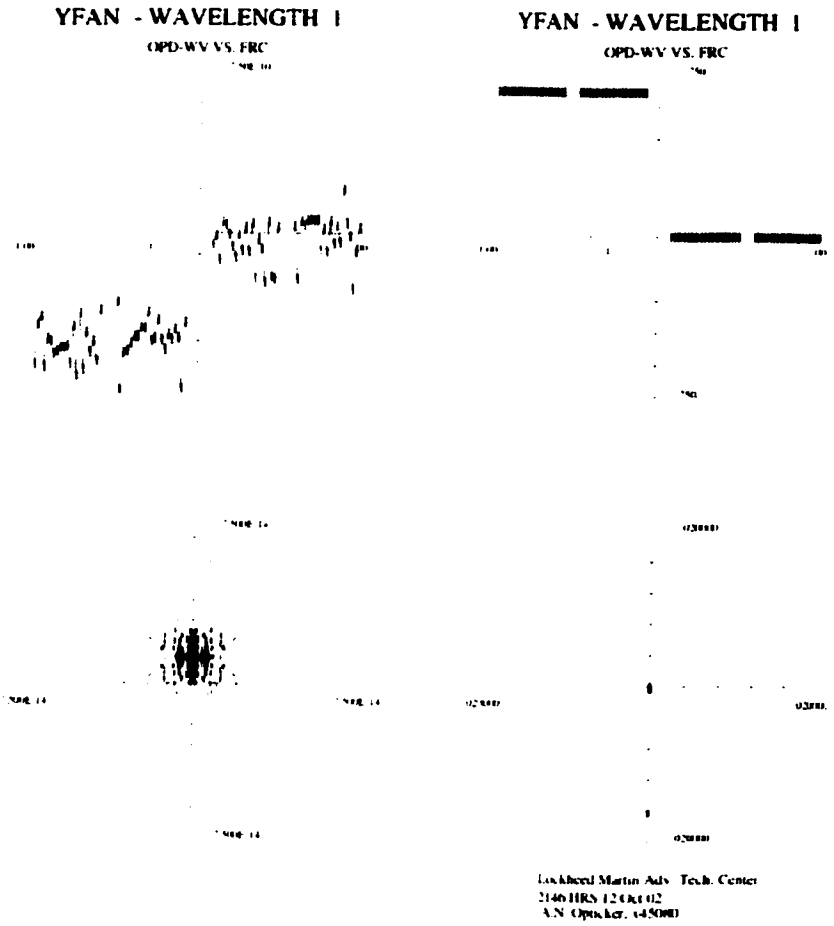

FIGURE A.2. *Optima output of wavefans and spot diagrams from the example system.*

To print all the lens data in the command window:

prtlens

A.2 Multiple aperture system example in Zemax

To model the example system in Zemax (release 9 July 2002), open a new file. The "Lens Data Editor" has three lines in it. Use the "Insert" button on the keyboard to add more lines, for a total of eight.

To set up the basics for the lens system, choose "System \ General \ Aperture." Set the Aperture Type to "Entrance Pupil Diameter" and the Aperture Value to 7.5. Under "System \ General \ Units" set the Lens Units to "meters." The default field angle will be 0, and the default wavelength will be the visible 550 nm. To change those, use "System \ Field" and "System \ Wavelengths." Add a field angle in y of 0.0083 degrees, to match the example system in the other programs.

The tables below show the values in the Lens Data Editor window for the example system. Values not shown should be left at default. The semi-diameters are generated by the program, and should not be entered by hand.

Surface	Type	Comment	Radius	Thickness	Glass
OBJ	Standard	OBJECT	Infinity	Infinity	
STO	Standard	PLOT BEGIN	Infinity	4.5	
2	NonSeqComp	NSQ IN	Inifinity	—	
3	Standard	NSQ OUT	Inifinity	-2.44	—
4	NonSeqComp	NSQ IN	Inifinity	—	
5	Standard	NSQ OUT	Inifinity	9.0	—
6	Standard	COLLECTOR	-8.000	-4.0	MIRROR
7	Standard	IMAGE	Inifinity		

TABLE A.2. *The entries in the first six columns in the Lens Data Editor, for the example system.*

Surface	Semi-Diameter	Conic	Draw Ports	Exit Loc Z	Reverse Rays
OBJ	Infinity	0			
STO	3.750000	0			
2	3.750652	0	1	-0.5	1
3	3.750000 U	0			
4	2.031386	0	1	0.3	1
5	3.562500 U	0			
6	1.962937	-1			
7	0.017227	0			

TABLE A.3. *Entries in the Lens Data Editor, columns to the right of the first six. Values not shown should be left at default.*

Surfaces 2 and 4 are considered nonsequential surfaces. Their details are specified

in the "Nonsequential Component Editor". To open it, choose "Editors \ Nonsequential Components." Insert a line, for a total of two. To move between the nonsequential components of surfaces 2 and 4, use the keystrokes "Ctrl \ Shift \ D." When the window is titled "Nonsequential Component Editor: Component Group on Surface 2," the values shown in the following table should be entered.

	Object Type	**Comment**	**Y Position**	**Z Position**
1	Standard Surface	PRIMARY A	2.000	0.5
2	Standard Surface	PRIMARY B	-2.000	0.5
Material	**Radius**	**Conic**	**Max Aper**	**Min Aper**
MIRROR	-7.000	-1.000	1.750	0.300
MIRROR	-7.000	-1.000	1.750	0.300

TABLE A.4. *Values for the example system, in the window "Nonsequential Component Editor: Component Group on Surface 2."*

For the nonsequential components associated with surface 4, the window will have the title "Nonsequential Component Editor: Component Group on Surface 4." The values for the example system are shown below.

	Object Type	**Comment**	**Y Position**	**Z Position**
1	Standard Surface	SECONDARY A	2.000	-0.2
2	Standard Surface	SECONDARY B	-2.000	-0.2
Material	**Radius**	**Conic**	**Max Aper**	**Min Aper**
MIRROR	0.280	-1.000	0.15	0
MIRROR	0.280	-1.000	0.15	0

TABLE A.5. *Values for the example system, in the window "Nonsequential Component Editor: Component Group on Surface 4."*

The schematic shown in Figure A.3 was generated by choosing "Analysis \ Layout \ 3D Layout" from the menu bar in Zemax's main window. In the menu in the schematic's window, the "Settings" selection was used to change the number of rays to 20, field to 1, and wavelength to 1.

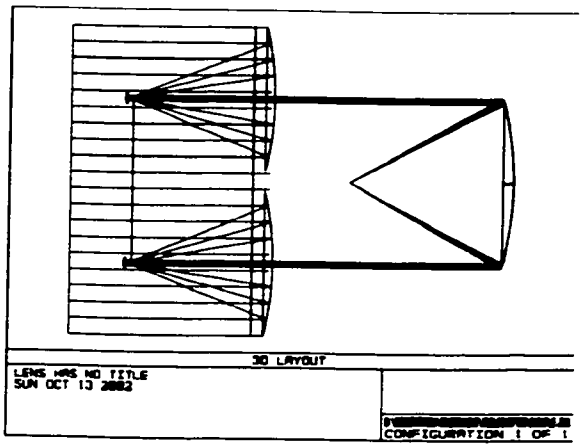

FIGURE A.3. *Layout of the example system, produced by Zemax. The vertical lines show entrance ports for the nonsequential regions.*

The PSF of the system, shown in Figure A.4, was generated by choosing "Analysis \ PSF \ Huygens Point Spread Function." Under "Settings" in the PSF display window: Pupil Sampling = 128x128, Image Sampling = 128x128, and Image Delta = 0.5, with the other values left to their default settings. Wave fans can be produced using "Analysis \ Fans \ Optical Path", and spot diagrams can be displayed using "Analysis \ Spot Diagrams \ Standard." (The output displays from those commands are not shown here.)

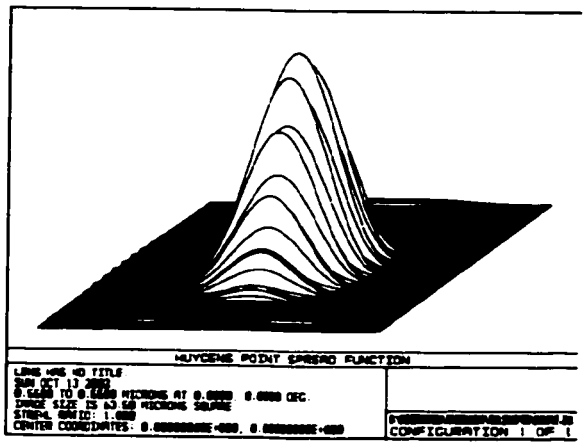

FIGURE A.4. *Point spread function of the example system, produced by Zemax.*

A.3 Diffraction image calculation example in Mathematica

Mathematica (version 4.1.10 for Windows) was used for most of the diffraction calculations in this dissertation. The file that follows calculates the monochromatic image from a two-aperture telescope, with piston errors in the apertures of the telescope. This Fourier transform calculation is in the Fraunhofer regime, and assumes that there are no other aberrations in the optical system.

```
shift = 2.0;   (* distance to shift each aperture from center *)
rad = 1.75;   (* semi-diameter of each of the primaries *)

npix = 512;   (* number of pixels in the FFT *)
Δx = 20.0;    (* total width of one edge of the grid, in real space *)
δx = Δx / npix;   (* width of one of the pixels, in real space *)
δξ = 1 / Δx;   (* width of one of the pixels, after the FFT, in frequency space *)
Δξ = 1 / δx;   (* width of the whole grid, after the FFT, in frequency space *)

cyl[r_] := If[r^2 > rad^2, 0.0, 1.0]; (* defines a cylindrical function *)

XArray = Table[x, {y, -Δx/2 + δx, Δx/2, δx}, {x, -Δx/2 + δx, Δx/2, δx}];
YArray = Table[y, {y, -Δx/2 + δx, Δx/2, δx}, {x, -Δx/2 + δx, Δx/2, δx}];
(* creates two arrays,
 one that holds the x-coordinate of each pixel and one that holds the y *)

Mask1Function = Compile[{x, y}, Evaluate[cyl[Sqrt[(x - shift)^2 + y^2]]]];
Mask1 = MapThread[Mask1Function, {XArray, YArray}, 2];
(* makes a single aperture, shifted to the right,
 by mapping the cylinder function over the x and y coordinates *)
Mask2Function = Compile[{x, y}, Evaluate[cyl[Sqrt[(x + shift)^2 + y^2]]]];
Mask2 = MapThread[Mask2Function, {XArray, YArray}, 2];
(* makes a single aperture, shifted to the left *)

PupilAmp = e^(-I*2*π*0.1) * Mask1 + e^(I*2*π*0.1) * Mask2;

temp1 = Re[PupilAmp];
temp2 = Im[PupilAmp];
ListDensityPlot[temp1, Mesh → False, Frame → False, ImageSize → 140];
ListDensityPlot[temp2, Mesh → False, Frame → False, ImageSize → 140];
(* plots the irradiance and phase in the entrance pupil *)
```

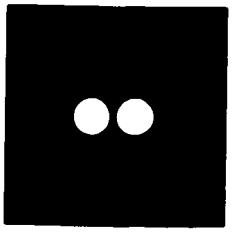

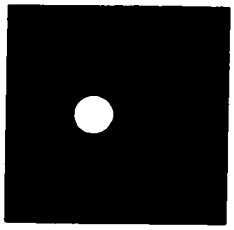

```
Checker = Table[If[EvenQ[i + j], 1.0, -1.0], {i, 1, npix}, {j, 1, npix}];
(* creates a "checkerboard" matrix with alternating values of 1 and -1 *)

ImageAmp = Fourier[Evaluate[PupilAmp * Checker]];
ImageIrr = Chop[ImageAmp * Conjugate[ImageAmp]];
(* calculates the Fourier transform of the pupil amplitude *)

<< LinearAlgebra`MatrixManipulation`
ImageIrrSmall = TakeMatrix[ImageIrr, {220, 220}, {292, 292}];
(* takes a smaller part of the image matrix, for plotting *)

ListDensityPlot[ImageIrrSmall,
  PlotRange → All, Mesh → False, Frame → False, ImageSize → 140];
(* plots the image irradiance *)
```

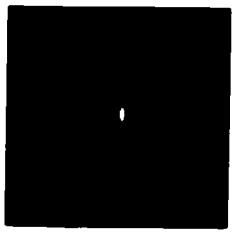

```
ListPlot[ImageIrrSmall[[36]], PlotJoined → True, PlotRange → All];
(* plots a cross-section of the image *)
```

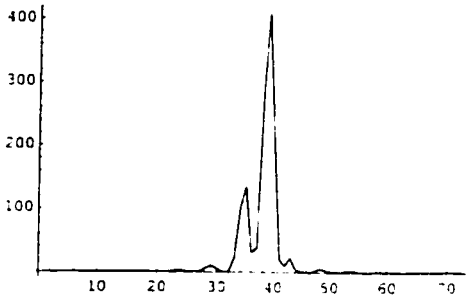

Appendix B

REPRINT, "PHASE THEORY FOR MULTIPLE APERTURE SYSTEMS."

Phase theory for multiple aperture systems

Erin M. Sabatke, MEMBER SPIE
José M. Sasián, FELLOW SPIE
University of Arizona
Optical Sciences Center
1630 East University Boulevard
Tucson, Arizona 85721
E-mail: esabatke@optics.arizona.edu

Abstract. We establish the groundwork for a phase theory applicable to multiple aperture systems. To do this, we define ideal behavior as the phase behavior of an off-axis piece of a system that has rotational symmetry. Then we examine the phase behavior of a more general system that has only a single plane of symmetry. This system represents a branch of a multiple aperture system. Comparison of the two systems leads to conditions for which the plane symmetric system has ideal behavior. As a result of this comparison, design rules that are commonly applied to multiple aperture systems appear naturally, including the well-known requirement that the exit pupil is a scaled copy of the entrance pupil. The phase theory that we present is cohesive, provides useful design guidelines, and can be considered an addition to wave aberration theory.
[DOI: 10.1117/1.1431969]

Subject terms: multiple apertures; aberrations; phased arrays; interference; imaging systems.

Paper 200318 received Aug. 10, 2000; revised manuscript received Sep. 21, 2001; accepted for publication Sep. 21, 2001.

1 Introduction

While studying the literature on multiple aperture systems, we found that some very useful design rules and ideas have been presented. Some of the relevant papers in the literature are those that deal with the diffraction aspects of multiple aperture systems,[1-10] such as the point spread function and modulation transfer function. Others concentrate on the important first-order design aspects,[7-20] including field of view, pupil mapping, and distortion. A few papers discuss several topics in the design process,[21-24] such as fill factors and tolerances. Finally, some references deal with topics such as array distributions and polarization issues.[25-27] However, the design rules discussed in these papers appear not to be part of a cohesive aberration theory on multiple aperture systems.

We present the basis of a phase theory for multiple aperture systems. This theory shows in a natural way how phase effects and design rules arise from a cohesive treatment. The theory uses the wave approach and can be considered an addition to wave aberration theory. We first discuss the phase behavior of a rotationally symmetric system that forms a perfect point image. We define a perfect or ideal image as having only phase terms that do not degrade the point image. These terms are piston, magnification, focus, field curvature, and distortion. This is equivalent to having wavefronts that are spherical, so that points will image to points.

Next, we discuss the behavior of this system when the wavefront is referenced to an off-axis point in the pupil. This is equivalent to masking the pupil, so that only an off-axis aperture within the original pupil is used. The wavefront itself is unchanged under this transformation, so that the geometric image formed is still a point. This analysis reveals the way in which the phase of a rotationally symmetric system behaves, or achieves perfect beam combining. We define this phase behavior as ideal.

Finally, we look at the phase behavior of one branch of a multiple aperture system. Such a branch has only one plane of symmetry, in general. Comparing the phase behavior of the plane symmetric system to the phase behavior of the ideal system gives conditions for which the wavefront will be perfectly combined. Phase terms of the same form occur in the two systems, but the magnitudes of the terms in the plane symmetric system are found to be placed under strict conditions to achieve perfect beam combining. Other terms that are allowed in general plane symmetric systems must be absent for good beam combining in a multiple aperture system.

2 Second-Order Effects

2.1 *Ideal Phase Behavior to Second Order*

In a rotationally symmetric optical system, the geometric wavefront phase can be expressed as:

$$P_{AB'}(\mathbf{H},\rho') = \Sigma_k \Sigma_l \Sigma_m P_{klm} (\mathbf{H}\cdot\mathbf{H})^l (\rho'\cdot\rho')^m (\mathbf{H}\cdot\rho')^n$$
$$k = 2j+m, \quad l = 2n+m, \tag{1}$$

where $\mathbf{H}$ is the normalized field vector from the axis of symmetry to the point of interest in the image plane, and ρ' is the normalized aperture vector from the optical axis to the point of interest in the exit pupil. $\mathbf{H}$ is normalized by the real height of the image, and ρ' is normalized by the real radius of the pupil. θ is the angle between $\mathbf{H}$ and ρ' in a plane perpendicular to the optical axis. The coefficients P_{klm} determine the magnitude of each type of phase term.

In Fig. 1, showing the entrance and exit pupils of a system, Eq. (1) describes the phase between points O and B', or equivalently, between A and B' given that O and A are in phase. The phase expansion $P_{AB'}(\mathbf{H},\rho')$ of Eq. (1) is

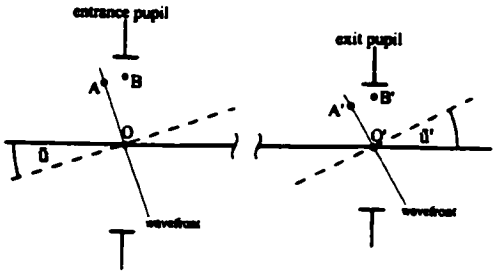

Fig. 1 Geometry showing the pupils of a rotationally symmetric system. O and O' lie at the axis of symmetry at the center of the exit and entrance pupils. A and A' are points in the geometrical wavefront. B and B' denote the points of interest in the pupils.

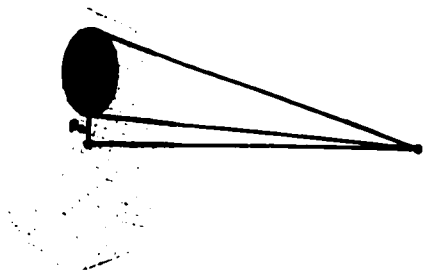

Fig. 2 The phase is described with respect to an off-axis reference point with the vectors ρ_o and ρ. The system has an underlying rotational symmetry.

similar to the wave aberration function $W(\mathbf{H},\rho')$ used to describe aberrations in rotationally symmetric systems. However, in the wave aberration function, some terms are customarily omitted or have different meanings.

As an initial step, we consider terms up to second order in the aperture and field. These terms are:

$$\begin{aligned} P_{AB'}(\mathbf{H},\rho') = {} & P_{000} && \text{uniform piston} \\ & + P_{200}\mathbf{H}\cdot\mathbf{H} && \text{quadratic piston} \\ & + P_{111}\mathbf{H}\cdot\rho' && \text{magnification} \\ & + P_{020}\rho'\cdot\rho' && \text{focus.} \end{aligned} \tag{2}$$

The coefficients, P_{klm}, are specific to the particular system and can be calculated with ray traces of the marginal and chief rays. Specifically,

$$\begin{aligned} P_{000} &= \Sigma n t \\ P_{200} &= 0 \\ P_{111} &= n' D' \tan \bar{u}' = \Phi \\ P_{020} &= n' D' \tan u'/2, \end{aligned} \tag{3}$$

where n is the index of refraction after the surface, t is the thickness to the next surface, u' and $\bar{u}'$ are the marginal and chief ray angles at the exit pupil, D' is the marginal ray height at the exit pupil, and Φ is the Lagrange invariant.

Physically, these coefficients describe the phase's behavior at the exit pupil. P_{000} represents the optical path length along the optical axis. P_{200} is set to zero because the pupils are optically conjugate and, therefore, there are no second-order phase errors. The coefficient P_{111} represents the magnitude of a linear phase change with respect to the aperture, or a tilt of the wavefront that carries the transverse magnification. P_{020} represents the magnitude of a quadratic phase or the sag of the geometrical wavefront, which is focus. These terms define the position of the image point, but do not degrade the image.

We now examine an off-axis segment of a rotationally symmetric system, with a wavefront given by Eq. (2). The wavefront is unchanged, but is now described with respect to an off-axis point. This is equivalent to masking the pupil of a system that is rotationally symmetric about the system axis, as shown in Fig. 2. The phase in an off-axis subaperture at the exit pupil of a rotationally symmetric system can be calculated by decentering the aperture vector, ρ', by a constant distance, ρ_o, as shown in Fig. 3. That is, the vector ρ' becomes $\rho_o + \rho$ where the vector ρ represents the point of interest in the subaperture and the vector ρ_o represents the location of the center of the subaperture. We have changed the origin of our phase description to the center of the subaperture, as quantified by the constant vector ρ_o. The wavefront itself is unchanged, though part of it is masked, so the image must remain perfect. (The vectors ρ and ρ_o are normalized by the original radii of the exit pupil, D', and have ranges less than 0 to 1, unlike standard normalized coordinates.)

Two optical systems are equivalent if their phase function is the same. We need to determine the phase function corresponding to an off-axis section or masked pupil of an axially symmetric system. This will define the ideal phase function. The phase function is defined as the optical path length between the center point B of the entrance pupil and a given point B' in the exit pupil as defined by the vectors $\mathbf{H}$ and ρ.

Referring to Fig. 3, to determine the phase or optical path length between points B and B' at the pupils, rather

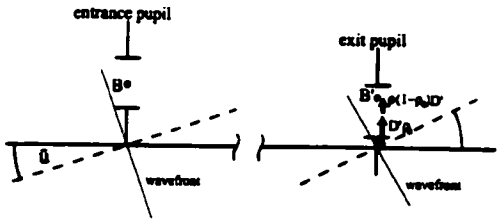

Fig. 3 Geometry showing the pupils of an off-axis section of a rotationally symmetric system. B and B' denote the points of interest in the pupils. B is at the center of the off-axis entrance pupil. B' is at the off-axis exit pupil as specified by the vector ρ. The reference point has been shifted by a distance of $D\rho_o$. The exit pupil has a physical diameter of $D'(1-\rho_o)$.

than A and B', the phase P_{AB} must be subtracted from the phase $P_{AB'}$. That is, $P_{BB'}=P_{AB'}-P_{AB}$.

The phase P_{AB} is given by

$$P_{AB}=nD\sin\bar{u}(\mathbf{H}\cdot\rho_u)+(nD^2/2R)(\rho_u\cdot\rho_u)$$
$$\approx nD\tan\bar{u}(\mathbf{H}\cdot\rho_u)+(nD\tan u/2)(\rho_u\cdot\rho_u). \quad (4)$$

where $\bar{u}$ is the chief ray angle and u is the marginal ray angle at the entrance pupil, D is the radius of the entrance pupil, and R is the radius of curvature of the incoming wavefront. By substituting ρ' for $\rho_u+\rho$ in Eq. (2) and subtracting the phase P_{AB}, the phase $P_{BB'}$ from B to B' to second order of approximation is given by:

$$P_{BB'}(\mathbf{H},\rho)=P_{000}+P_{200}(\mathbf{H}\cdot\mathbf{H})+P_{111}(\mathbf{H}\cdot\rho_u+\mathbf{H}\cdot\rho)$$
$$+P_{020}(\rho_u\cdot\rho_u+2\rho_u\cdot\rho'+\rho'\cdot\rho')$$
$$-nD\tan\bar{u}(\mathbf{H}\cdot\rho_u)-(nD\tan u/2)(\rho_u\cdot\rho_u). \quad (5)$$

By inserting the coefficients P_{klm} of Eq. (3) and using the identity

$$n'D'\tan u'-nD\tan u=-nn'DD'/nf', \quad (6)$$

the phase $P_{BB'}$ becomes:

$$P_{BB'}(\mathbf{H},\rho)=\Sigma nt-(nn'DD'/2nf')(\rho_u\cdot\rho_u)$$
$$+(n'D'\tan\bar{u}'-nD\tan\bar{u})(\mathbf{H}\cdot\rho_u)$$
$$+n'D'\tan\bar{u}'(\mathbf{H}\cdot\rho)+n'D'\tan\bar{u}'(\rho_u\cdot\rho)$$
$$+n'D'\tan u'/2(\rho\cdot\rho)+P^+. \quad (7)$$

where f' is the rear focal length of the system under consideration and P^+ represents phase terms higher than second order.

It is clear that new phase terms have appeared due to the shifting of the pupil center. Magnification, $(\mathbf{H}\cdot\rho')$, leads to a new linear piston term, $(\mathbf{H}\cdot\rho_u)$. Focus, $(\rho'\cdot\rho')$, contributes two new terms ($\rho_u\cdot\rho_u$ and $\rho_u\cdot\rho$). Notice that the magnitudes of these new terms depend on the magnitudes of their parent coefficients. This is a result of the inherent rotational symmetry of the wavefront. In total, there are six types of phase terms in Eq. (7): piston, linear piston, quadratic piston, tilt, magnification, and focus.

The linear piston term, $(n'D'\tan\bar{u}'-nD\tan\bar{u})(\mathbf{H}\cdot\rho_u)$, is a second-order statement of the sine condition applied to the pupils, or Meinel's condition.[13] This states that for linear phase effects to be absent in a multiple aperture system, the demagnification of the beam sizes must be equivalent to the demagnification of beam separation.

In an axially symmetric system, the Lagrange invariant Φ is equal to $\Phi=n'D'\tan\bar{u}'=nD\tan\bar{u}$. Therefore,

$$n'D'\tan\bar{u}'-nD\tan\bar{u}=0, \quad (8)$$

which implies that to the second order of approximation there are no linear phase $(\mathbf{H}\cdot\rho_u)$ effects. Thus Eq. (7) becomes,

$$P_{BB'}(\mathbf{H},\rho)=\Sigma nt-(nn'DD'/2nf')(\rho_u\cdot\rho_u)$$
$$+n'D'\tan\bar{u}'(\mathbf{H}\cdot\rho)+n'D'\tan u'(\rho_u\cdot\rho)$$
$$+n'D'\tan u'/2(\rho\cdot\rho)+P^+. \quad (9)$$

We note that the radii d and d' of the entrance and exit pupils of the branch system are given respectively by,

$$d=(1-\rho_u)D \text{ and } d'=(1-\rho_u)D'. \quad (10)$$

In summary, we have described the phase (or optical path length) between two points in the entrance and exit pupils of a system with rotational symmetry about the system axis. Specific formulas for the phase coefficients are given. When this phase is described with respect to an off-axis point, additional terms appear in the description of the wavefront at the exit pupil. Equations (2) and (9) describe the same wavefront, but with respect to different reference points. Equation (9) is the phase function that defines ideal behavior of a branch of a multiple aperture system. Two or more systems with phase behavior given by Eq. (9) would display perfect beam combining, to second order, if used as branches of a multiple aperture system. The analysis presented here applies not only to afocal telescopes but also to a wider range of multiple aperture systems. We are not omitting terms in our phase expansion that could represent focal systems.

2.2 *Phase Behavior in a Branch That Has Plane Symmetry to Second Order*

In the previous sections, we established the ideal phase behavior in a branch of a multiple aperture system. In this section, we describe the phase behavior of a branch in a multiple aperture system, which is assumed to have only a single plane of symmetry. Plane symmetry encompasses the case of rotational symmetry and includes almost all multiple aperture systems.

The phase in a plane symmetric system can be described with a generalized expansion that reflects plane symmetry with respect to a fixed vector $\mathbf{i}$.[28] The expansion is:

$$P(\mathbf{H},\rho')=\Sigma_{k,m,n,p,q}P_{2k+n+p,2m+n+q,n,p,q}(\mathbf{H}\cdot\mathbf{H})^k$$
$$\times(\rho'\cdot\rho')^m(\mathbf{H}\cdot\rho')^n(\mathbf{i}\cdot\mathbf{H})^p(\mathbf{i}\cdot\rho')^q, \quad (11)$$

where $P_{2k+n+p,2m+n+q,n,p,q}$ represents a particular coefficient defined by the integers k, m, n, p, and q.

With reference to Fig. 4, the phase $P_{CC'}$ to second order is described by the terms:

$$P_{CC'}(\mathbf{H},\rho')=P_{0000}+P_{10010}(\mathbf{i}\cdot\mathbf{H})+P_{01001}(\mathbf{i}\cdot\rho')$$
$$+P_{02000}(\rho'\cdot\rho')+P_{11100}(\mathbf{H}\cdot\rho')$$
$$+P_{20000}(\mathbf{H}\cdot\mathbf{H})+P^+. \quad (12)$$

There are six types of terms: piston, linear piston, quadratic piston, magnification, focus, and tilt. In this plane symmetric system, the coefficients of the phase terms can be independent of each other, and their magnitudes will depend on the particular construction of the branch system.

We now calculate the phase of the branch system, between C and C', with respect to the reference points in the

Fig. 4 Geometry showing the pupils of a plane symmetric system. C and C' denote the points of interest in the pupils. C is at the center of the entrance pupil. C' is at the exit pupil as specified by the vector ρ'.

ideal system, B and B'. To do this, we superimpose the actual plane symmetric branch on top of the ideal system, as shown in Fig. 5. The pupil points B and B' of the ideal system and the pupil points C and C' of the plane symmetrical branch are allowed to be offset by z, z', y, and y'. We have neglected mispositionings in x (into and out of the page).

The phase $P_{BB'}$ of the plane symmetric branch, with respect to the reference points B and B', is given by:

$$P_{BB'}=P_{CC'}+P_{BC}-P_{B'C'}. \tag{13}$$

where $P_{CC'}$ is the phase corresponding to a plane symmetric system given by Eq. (12). P_{BC} is the phase between points B and C, and $P_{B'C'}$ is the phase between B' and C'. P_{BC} and $P_{B'C'}$ arise because of possible errors in the pupil locations: z, z', y, and y'. With reference to Fig. 5, we have

$$P_{BC}=ny\sin\bar{u}+nz\cos\bar{u}$$

$$P_{B'C'}=n'y'\sin\bar{u}'+n'z'\cos\bar{u}'. \tag{14}$$

The difference of the sine terms in these equations is:

$$ny\sin\bar{u}-n'y'\sin\bar{u}'\approx(ny\tan\bar{u}-n'y'\tan\bar{u}')+(ny\tan^3\bar{u}-n'y'\tan^3\bar{u}')/2. \tag{15}$$

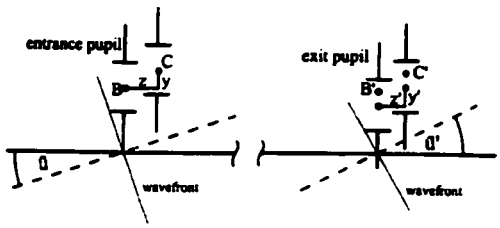

Fig. 5 A superposition of the ideal system and the plane symmetric system. The centers of the pupils are allowed to be offset from those of the ideal system by the amounts y and z.

The difference of the cosine terms is:

$$nz\cos\bar{u}-n'z'\cos\bar{u}'=(nz-n'z')-(nz\sin^2\bar{u}/2-n'z'\sin^2\bar{u}'/2). \tag{16}$$

Thus, the phase $\underline{P}_{BB'}$ to second-order is

$$\begin{aligned}\underline{P}_{BB'}(\mathbf{H},\rho')=&[(nz-n'z')+P_{00000}]+P_{01001}(\mathbf{i}\cdot\rho')\\&+P_{02000}(\rho'\cdot\rho')+P_{11100}(\mathbf{H}\cdot\rho')\\&+[ny\tan\bar{u}-n'y\tan\bar{u}'+P_{10010}](\mathbf{i}\cdot\mathbf{H})\\&+[-(nz\sin^{-2}\bar{u}/2-n'z\sin^2\bar{u}/2)+P_{20000}]\\&\times(\mathbf{H}\cdot\mathbf{H})+P^*.\end{aligned} \tag{17}$$

The phase $\underline{P}_{BB'}(\mathbf{H},\rho')$ in Eq. (17) describes the phase of a branch that is plane symmetric in a multiple aperture system, with respect to the pupil locations of the ideal system. The expression consists of the phase between the pupils of the plane symmetric system and the phase contributed by an offset or error in the position of the pupils. The terms contributed by the error in the position of the pupils are: a constant phase term $(nz-n'z')$, a linear piston term $(ny\tan\bar{u}-n'y'\tan\bar{u})(\mathbf{i}\cdot\mathbf{H})$, and a quadratic piston term, $[-(nz\sin^2\bar{u}/2-n'z'\sin^2\bar{u}'/2)+P_{20000}](\mathbf{H}\cdot\mathbf{H})$.

The linear phase term represents Meinel's condition as applied to the lateral pupil error. The quadratic piston term involves Herschel's condition as applied to the longitudinal error. Both of these terms, the linear phase and the quadratic, can be used to establish positional tolerances.[17]

2.3 *Comparison of the Ideal and Plane Symmetric Systems to Second Order*

In the previous sections, we calculated the phase $P_{BB'}(\mathbf{H},\rho)$ associated with an ideal multiple system and the phase $\underline{P}_{BB'}(\mathbf{H},\rho')$ associated with a plane symmetric branch that may have some positional errors with respect to the ideal system. The phase expressions for the ideal and plane symmetric systems are given in Eqs. (9) and (17), and are repeated below:

$$\begin{aligned}P_{BB'}(\mathbf{H},\rho)=&\Sigma nt-(nn'DD'/2nf')(\rho_a\cdot\rho_a)\\&+n'D'\tan\bar{u}(\mathbf{H}\cdot\rho)+n'D'\tan u'(\rho_a\cdot\rho)\\&+n'D'\tan u'/2(\rho\cdot\rho)+P^*\end{aligned} \tag{9}$$

$$\begin{aligned}\underline{P}_{BB'}(\mathbf{H},\rho)=&[(nz-n'z')+P_{00000}]+P_{01001}(\mathbf{i}\cdot\rho')\\&+P_{02000}(\rho'\cdot\rho')+P_{11100}(\mathbf{H}\cdot\rho')+[ny\tan\bar{u}\\&-n'y'\tan\bar{u}'+P_{10010}](\mathbf{i}\cdot\mathbf{H})+[-(nz\sin^2\bar{u}/2\\&-n'z'\sin^2\bar{u}'/2)+P_{20000}](\mathbf{H}\cdot\mathbf{H})+P^*.\end{aligned} \tag{17}$$

A comparison of these two expressions leads to the conditions under which a plane symmetric branch displays ideal behavior. Gathering coefficients of terms with the same functional dependencies gives:

$$(nz-n'z')+P_{00000}=P_{000}-(nn'DD'/2nf')\rho_a^2 \tag{18}$$

$$P_{01001}=n'D'\tan u'(1-\rho_a)\rho_a \tag{19}$$

$$P_{02000}=(n'D'\tan u'/2)(1-\rho_a)^2 \tag{20}$$

$$P_{11100}=n'D'\tan\bar{u}'(1-\rho_a) \tag{21}$$

$$(ny\tan\bar{u}-n'y'\tan\bar{u}')+P_{10010}$$
$$=(n'D'\tan\bar{u}'-nD\tan\bar{u})=0 \tag{22}$$

$$-(nz\sin^2\bar{u}/2-n'z'\sin^2\bar{u}'/2)+P_{20000}=0. \tag{23}$$

The factor $(1-\rho_a)$ in Eqs. (19) to (21) has been included to account for the difference in magnitude of the vectors ρ and ρ' in Eqs. (9) and (17), respectively. The phase behavior required from the plane symmetric system, through Eqs. (18) to (23), is equivalent to what is known as "the golden rule of separated telescopes." [11] The rule states that "as viewed from a point in the focal plane, beams from separated telescopes must be recombined so that they appear to be coming directly from a single large telescope which has been masked so as to reproduce exactly the ensemble of collecting telescopes." The ideal system displays exactly this behavior, and we have required that the plane symmetric system behave ideally, to second order.

Equation (18) deals with constant phase terms. These describe the optical path length between the entrance pupil and exit pupil. This rule requires that the optical path along the axis in the plane symmetric branch be equal to that in the ideal system. The path length in the ideal system comprises the optical path along the axis and a term that depends on the focal length and the offset of the pupil as shown by the ρ_a dependence. The equation shows that a mismatch in the system's axial optical path can be compensated by longitudinal adjustments of the pupil positions, z and z'. This would also affect Eq. (23), however.

Equation (19) requires that the optical axis ray in the ideal and the plane symmetric branch system have the same orientation. The focal property of the system and the pupil offset from the system axis in the ideal system changes the direction of the optical axis ray. Equation (20) is similar, in that it requires that the longitudinal location of the image point should be equal in both systems. Thus Eqs. (19) and (20) establish that the images in both systems have the same orientation and location.

Equation (21) requires the image in both systems to have the same size. This is equivalent to requiring that the magnifications of the two systems are equal. In a telescope objective, where the magnification is zero, Eq. (21) requires that the focal lengths of the ideal and plane symmetric branch be equal.

Equation (22) shows that a transverse mislocation of the pupils leads to a linear piston error, as predicted by Meinel's condition. Since such an error is not allowed in the ideal system, the pupil mislocation is not allowed. In theory, it would be possible to compensate for the presence of the P_{10010} term for the center field point by a pupil adjustment. This would probably be preferable to no compensation. To second order, this would not disturb the rest of the system.

Equation (23) shows that longitudinal errors in the pupil positions lead to quadratic piston errors, as well as the constant piston terms that appeared in Eq. (18). Adjusting the pupil locations to compensate for the presence of a P_{20000} term could cause (23) to be satisfied, but would simultaneously change Eq. (18), which also contains z and z' terms.

In summary, to exhibit ideal behavior to second order, a branch of a multiple aperture system should satisfy Meinel's condition (no linear phase terms), and its focal length and the location of the image should match those of the associated ideal system. Equations (18) to (23) set these conditions.

3 Fourth-Order Effects

3.1 *Ideal Phase Behavior to Fourth Order*

In this section, we discuss phase effects to fourth order in the aperture and field. We follow a similar treatment to that used in finding the second-order effects. First we find the behavior of the ideal system. The fourth-order phase terms in a rotationally symmetric system are:

$$P_{AB'}(\mathbf{H},\rho')=P_{040}(\rho'\cdot\rho')^2+P_{131}(\mathbf{H}\cdot\rho')(\rho'\cdot\rho')$$
$$+P_{222}(\mathbf{H}\cdot\rho')^2+P_{220}(\mathbf{H}\cdot\mathbf{H})(\rho'\cdot\rho')$$
$$+P_{311}(\mathbf{H}\cdot\mathbf{H})(\mathbf{H}\cdot\rho')+P_{400}(\mathbf{H}\cdot\mathbf{H})^2. \tag{24}$$

The terms in Eq. (24) represent spherical aberration, coma, astigmatism, field curvature, distortion, and quartic piston. The coefficient P_{220} corresponding to field curvature has a different meaning than the coefficient W_{220} of field curvature in standard aberration theory. In this case, P_{220} gives the change in focus with respect to P_{020}, while W_{220} gives the change of focus with respect to the Gaussian image plane.

Since we require perfect point imaging in our ideal system, phase terms that degrade the point image must be excluded. This is equivalent to requiring a spherical wavefront and therefore spherical aberration, coma, and astigmatism coefficients must be zero.

$$P_{040}=P_{131}=P_{222}=0. \tag{25}$$

The phase description of Eq. (24) simplifies to:

$$P_{AB'}(\mathbf{H},\rho')=P_{220}(\mathbf{H}\cdot\mathbf{H})(\rho'\cdot\rho')+P_{311}(\mathbf{H}\cdot\mathbf{H})(\mathbf{H}\cdot\rho')$$
$$+P_{400}(\mathbf{H}\cdot\mathbf{H})^2. \tag{26}$$

The only remaining terms are field curvature, distortion, and quartic piston.

Now we change the pupil to an off-axis reference point located at ρ_a by substituting $\rho'\rightarrow\rho_a+\rho$ into Eq. (26). This leads to

$$P_{AB'}(\mathbf{H},\rho)=P_{220}(\mathbf{H}\cdot\mathbf{H})(\rho_a\cdot\rho_a) \quad \text{quadratic piston}$$
$$+2P_{220}(\mathbf{H}\cdot\mathbf{H})(\rho_a\cdot\rho) \quad \text{quadratic distortion}$$
$$+P_{220}(\mathbf{H}\cdot\mathbf{H})(\rho\cdot\rho) \quad \text{field curvature}$$
$$+P_{311}(\mathbf{H}\cdot\mathbf{H})(\mathbf{H}\cdot\rho_a) \quad \text{cubic piston}$$
$$+P_{311}(\mathbf{H}\cdot\mathbf{H})(\mathbf{H}\cdot\rho) \quad \text{cubic distortion}$$
$$+P_{400}(\mathbf{H}\cdot\mathbf{H})^2 \quad \text{quartic piston.} \tag{27}$$

Under this expansion, the presence of distortion in the ideal system leads to a cubic piston term. The presence of field curvature leads to a piston term that is quadratic with the field vector and also contributes a quadratic distortion term. The quartic piston term is unchanged and does not generate additional terms.

With reference to Fig. 1, the fourth order terms of the phase P_{AB} and $P_{A'B'}$ must be subtracted and added, respectively, from Eq. (27). The fourth order term of concern here is obtained by expanding the sine function one more order. P_{AB} and $P_{A'B'}$ are given, respectively, by

$$\begin{aligned} P_{AB} &= nD \sin\bar{u}(\mathbf{H}\cdot\boldsymbol{\rho}_u) + (nD^2/2R)(\boldsymbol{\rho}_u\cdot\boldsymbol{\rho}_u) \\ &\approx nD\tan\bar{u}(\mathbf{H}\cdot\boldsymbol{\rho}_u) + (nD\tan u/2)(\boldsymbol{\rho}_u\cdot\boldsymbol{\rho}_u) \\ &\quad -(nD\tan^3\bar{u}/2)(\mathbf{H}\cdot\mathbf{H})(\mathbf{H}\cdot\boldsymbol{\rho}_u), \end{aligned} \tag{28}$$

$$\begin{aligned} P_{A'B'} &= n'D'\sin\bar{u}'(\mathbf{H}\cdot\boldsymbol{\rho}) + (n'D'^2/2R')(\boldsymbol{\rho}_u\cdot\boldsymbol{\rho}_u) \\ &\approx n'D'\tan\bar{u}'(\mathbf{H}\cdot\boldsymbol{\rho}_u) + (n'D'\tan u'/2)(\boldsymbol{\rho}_u\cdot\boldsymbol{\rho}_u) \\ &\quad -(n'D'\tan^3\bar{u}'/2)(\mathbf{H}\cdot\mathbf{H})(\mathbf{H}\cdot\boldsymbol{\rho}_u). \end{aligned} \tag{29}$$

Using only the fourth-order terms which depend on $(\mathbf{H}\cdot\mathbf{H})(\mathbf{H}\cdot\boldsymbol{\rho}_u)$, the phase description at the exit pupil can be written as,

$$\begin{aligned} P_{BB'} &= P_{220}(\mathbf{H}\cdot\mathbf{H})(\boldsymbol{\rho}_u\cdot\boldsymbol{\rho}_u) + 2P_{220}(\mathbf{H}\cdot\mathbf{H})(\boldsymbol{\rho}_u\cdot\boldsymbol{\rho}) \\ &\quad + P_{220}(\mathbf{H}\cdot\mathbf{H})(\boldsymbol{\rho}\cdot\boldsymbol{\rho}) + [P_{331} + nD\tan^3\bar{u}/2 \\ &\quad - n'D'\tan^3\bar{u}'/2](\mathbf{H}\cdot\mathbf{H})(\mathbf{H}\cdot\boldsymbol{\rho}_u) + P_{331}(\mathbf{H}\cdot\mathbf{H})(\mathbf{H}\cdot\boldsymbol{\rho}) \\ &\quad + P_{400}. \end{aligned} \tag{30}$$

3.2 *Phase Behavior in a Branch That Has Plane Symmetry to Fourth Order*

In a branch that has plane symmetry, there are 15 phase terms to consider.[28] The fourth order description of the phase between points C and C' in the pupils of a plane symmetric systems is

$$\begin{aligned} P_{CC'}(\mathbf{H},\boldsymbol{\rho}') &= P_{02002}(\mathbf{i}\cdot\boldsymbol{\rho}')^2 + P_{11011}(\mathbf{i}\cdot\mathbf{H})(\mathbf{i}\cdot\boldsymbol{\rho}') \\ &\quad + P_{10010}(\mathbf{i}\cdot\mathbf{H})^2 + P_{03001}(\mathbf{i}\cdot\boldsymbol{\rho}')(\boldsymbol{\rho}'\cdot\boldsymbol{\rho}') \\ &\quad + P_{12101}(\mathbf{i}\cdot\boldsymbol{\rho}')(\mathbf{H}\cdot\boldsymbol{\rho}) - P_{12010}(\mathbf{i}\cdot\mathbf{H})(\mathbf{H}\cdot\boldsymbol{\rho}') \\ &\quad + P_{21001}(\mathbf{i}\cdot\boldsymbol{\rho}')(\mathbf{H}\cdot\mathbf{H}) + P_{21110}(\mathbf{i}\cdot\mathbf{H})(\mathbf{H}\cdot\boldsymbol{\rho}') \\ &\quad + P_{30010}(\mathbf{i}\cdot\mathbf{H})(\mathbf{H}\cdot\mathbf{H}) + P_{04000}(\boldsymbol{\rho}'\cdot\boldsymbol{\rho}')^2 \\ &\quad + P_{13100}(\mathbf{H}\cdot\boldsymbol{\rho}')(\boldsymbol{\rho}'\cdot\boldsymbol{\rho}') + P_{22200}(\mathbf{H}\cdot\boldsymbol{\rho}')^2 \\ &\quad + P_{22000}(\mathbf{H}\cdot\mathbf{H})(\boldsymbol{\rho}'\cdot\boldsymbol{\rho}') + P_{31100}(\mathbf{H}\cdot\mathbf{H}) \\ &\quad \times(\mathbf{H}\cdot\boldsymbol{\rho}') + P_{40000}(\mathbf{H}\cdot\mathbf{H})^2. \end{aligned} \tag{31}$$

The terms in Eq. (31) are constant astigmatism, anamorphism, quadratic piston, constant coma, linear astigmatism, field tilt, quadratic distortion 1, quadratic distortion 2, cubic piston, and the last six terms are the standard rotationally symmetric fourth order terms.

3.3 *Comparison of the Ideal and Plane Symmetric Branch Systems to Fourth Order*

A comparison of the phase terms in the ideal and plane symmetric systems leads to a set of design rules to obtain the same phase behavior from both systems. These design rules are:

$$P_{02002} - P_{11011} = P_{10010} = P_{03001} = P_{12101} = 0 \tag{32}$$

$$P_{12010} = P_{21110} = P_{04000} = P_{13100} = P_{22200} = 0 \tag{33}$$

$$P_{30010} = [P_{311} + nD\tan^3\bar{u}/2 - n'D'\tan^3\bar{u}'/2]\boldsymbol{\rho}_u \quad \text{cubic piston} \tag{34}$$

$$P_{21001} = 2P_{220}(1-\boldsymbol{\rho}_u)\boldsymbol{\rho}_u \quad \text{quadratic distortion 1} \tag{35}$$

$$P_{22000} = P_{220}(1-\boldsymbol{\rho}_u)^2 \quad \text{field curvature} \tag{36}$$

$$P_{31100} = P_{311}(1-\boldsymbol{\rho}_u) \quad \text{distortion} \tag{37}$$

$$P_{40000} = P_{400} \quad \text{quartic piston.} \tag{38}$$

The factor $(1-\boldsymbol{\rho}_u)$ in Eqs. (35), (36), and (37) has been included to account for the difference in magnitude of the vectors $\boldsymbol{\rho}$ and $\boldsymbol{\rho}'$ in Eqs. (30) and (31), respectively. Design rules (32) and (33) state that a branch that has plane symmetry may not have constant astigmatism, anamorphism, quadratic piston, constant coma, linear astigmatism, field tilt, quadratic distortion 2, spherical aberration, coma, or astigmatism. The only phase terms that it can have are quadratic distortion 1, cubic piston, field curvature, cubic distortion, and quartic piston. The magnitude of these phase terms must be such that design rules (36) through (38) are satisfied.

The presence of field curvature contributes a quadratic piston term that modifies the second order design rule (23). The design rule to second order is

$$-(nz\sin^2\bar{u}/2 - n'z'\sin^2\bar{u}'/2) + P_{20000} = P_{200}, \tag{39}$$

and the presence of field curvature modifies this to

$$-(nz\sin^2\bar{u}/2 - n'z'\sin^2\bar{u}'/2) + P_{20000} = P_{200} + P_{220}\boldsymbol{\rho}_u^2. \tag{40}$$

Thus, to fourth order, there are several phase terms that a plane symmetric branch cannot contribute, so that phasing with other branches can occur. There are, however, some phase terms that can be present and that must have specific magnitudes as specified by design rules (34) through (38) and (40).

3.4 *Distortion and Field Curvature Requirements When a Branch Has Rotational Symmetry*

In the particular case of a branch of a reflective multiple aperture telescope that has rotational symmetry about the branch axis, it would be impossible to generate cubic piston and quadratic distortion 1. Equation (34) states that the ideal system should have a distortion[20] behavior, in P_{311}, so that $[P_{311} + nD\tan^3\bar{u}/2 - n'D'\tan^3\bar{u}'/2]$ is zero. Since

to third order of approximation $\tan^3\bar{u}' \equiv [nD/n'D'\tan\bar{u}]^3$, the phase distortion required by Eq. (34) is

$$P_{311} = -nD\tan^3\bar{u}[1-(nD/n'D')^2]/2. \tag{41}$$

This phase distortion has the same meaning as distortion in standard wave aberration theory. It represents departures from Gaussian imaging. From wave theory we have the relation $n'D'\tan\bar{u}' = nD\tan\bar{u} + P_{311}$. That is, the output phase tilt is a constant times the input phase tilt plus the amount contributed by distortion. The relation $[P_{311} + nD\tan^3\bar{u}/2 - n'D'\tan^3\bar{u}'/2]$ becomes

$$n'D'(\tan\bar{u}' - \tan^3\bar{u}'/2) - nD(\tan\bar{u} - \tan^3\bar{u}/2) \equiv n'D'\sin(\bar{u}') - nD\sin(\bar{u}), \tag{42}$$

which implies that an axially symmetric system satisfying the sine condition as applied to the pupils must produce distortion as given by Eq. (41). Such a system will not generate cubic piston terms $[(\mathbf{H}\cdot\mathbf{H})(\mathbf{H}\cdot\rho_u)]$.

Equation (34) can be rewritten as

$$P_{30010} = [n'D'\sin(\bar{u}') - nD\sin(\bar{u})]\rho_u. \tag{43}$$

With reference to Fig. 1 the phase difference between segments P_{AB} and $P_{A'B'}$ is given by

$$n'D'\sin(\bar{u}') - nD\sin(\bar{u}) = \bar{P}_{131}, \tag{44}$$

where $\bar{P}_{131}$ is the coma of the pupils.[29] Equation (44) is satisfied to first order in the chief angle $\bar{u}$ by Meinel's condition, to third order by fourth order pupil coma, and to higher order by higher orders of coma.

Using Eq. (44) we can rewrite Eq. (34) as

$$P_{30010} = \bar{P}_{131}\rho_u. \tag{45}$$

This states that in the presence of pupil coma there are cubic piston contributions.

Since an axially symmetric branch cannot contribute quadratic distortion 1, Eq. (35) leads to the conclusion that there can be no field curvature P_{220} allowed in the ideal system. Residual field curvature can lead to a quadratic dephasing [Eq. (40)] and to image separation.[14] The image separation is a result of missing the appropriate amount of quadratic distortion 1 as specified by Eq. (35).

Unlike standard field curvature W_{220} that measures defocus with respect to the Gaussian image plane, we note that P_{220} is a phase change with respect to phase focus P_{020}. The phase P_{220} is given by

$$P_{220} = \tfrac{1}{4}\Phi[\tan u'\tan\bar{u}' - \tan\bar{u}\tan\bar{u}] - \tfrac{1}{4}\Phi^2\Sigma(1/n' - 1/n)/r + \tfrac{1}{2}P_{222}, \tag{46}$$

where r is the radius of curvature of a given surface and Σ denotes summation over all surfaces. In Eq. (46) the terms $\frac{1}{4}\Phi^2\Sigma(1/n' - 1/n)/r$ and $\frac{1}{2}P_{222}$ account for the defocus introduced by Petzval field curvature and by astigmatism. The term $\frac{1}{4}\Phi[\tan u'\tan\bar{u}' - \tan u\tan\bar{u}]$ accounts by the defocus corresponding to the curved object and image surfaces as measured from the Gaussian planes. The curved object and image surfaces are concentric to the pupils, and their radii of curvature are the distances from the entrance and exit pupil to the object and image location, respectively.

From pupil aberration theory,[30] we have

$$\tfrac{1}{2}\Phi[\tan u'\tan\bar{u}' - \tan u\tan\bar{u}] = \bar{P}_{222} - P_{222},$$

where $\bar{P}_{222}$ and P_{222} are the pupil and image astigmatism, respectively. Equation (46) can be rewritten as

$$P_{220} = \tfrac{1}{2}\bar{P}_{222} - \tfrac{1}{4}\Phi^2\Sigma(1/n' - 1/n)/r. \tag{47}$$

Thus, to have no field defocus, P_{220}, the pupil field curvature induced by pupil astigmatism should cancel pupil Petzval field curvature, or both should be zero. This is equivalent to requiring that the sagittal astigmatic curve at the exit pupil be flat.[31]

In summary, when a multiple aperture telescope is made from axially symmetric branches to fourth order, there will be quadratic piston, cubic piston, and quadratic distortion dephasing effects. To avoid cubic piston effects, the axially symmetric branch system should satisfy the sine condition of the pupils, or equivalently there should be no pupil coma. To avoid quadratic piston and distortion, the branch system should not have field dependent defocus. These conditions lead to the axially symmetric branch to have distortion as specified by[20]

$$P_{31100} = -\tfrac{1}{2}D\tan^3\bar{u}[1-(nD/n'D')^2](1-\rho_u), \tag{48}$$

and to have no quadratic defocus

$$P_{22000} = 0, \tag{49}$$

which implies a flat sagittal image plane at the entrance and exit pupils. In addition, the branch is required to have no spherical aberration, coma, or astigmatism.

3.5 *Design Complexity in a Multiple Aperture System*

A multiple aperture system can be constructed in three ways. The first of these is constructing a system that is segmented and rotationally symmetric, such as one of the Keck telescopes. In this case all the design rules are automatically satisfied.

The second method is constructing branches composed of on-axis mirrors (rotational symmetry about the branch axis). The six-mirror MMT is an example of this, using on-axis mirrors and only flats for beam combining. In this case, satisfying the fourth order rules requires an increased system complexity, since some of the plane symmetric coefficients now appear in the design rules, and must be independently satisfied. In the case of a reflective telescope, this would represent a branch system free of field defocus and that satisfies the sine condition of the pupils. This would require more than two mirrors per branch, and the benefits of using on-axis mirrors may not be significant when compared to a segmented system that uses fewer off-axis mirrors.

The third method uses completely general, plane symmetric systems as branches. The large binocular telescope is an example of this case, with beams from the on-axis primaries being combined with other powered optics. In this case, satisfying the fourth order design rules can be a design challenge. One way to ease the design of such systems is by use of aberration theory of plane symmetric systems.[28] According to this theory, a confocal reflective system that provides perfect imaging along the optical axis ray, element after element, only has linear astigmatism, quadratic distortion, field tilt, cubic piston, and the Seidel aberrations. Linear astigmatism is proportional in such confocal systems to field tilt. Therefore, if a confocal system is designed with no linear astigmatism (one mirror tilt can nullify linear astigmatism) and is free of Seidel spherical aberration, coma, and astigmatism, then it will have only the phase terms that the ideal system can have. This observation provides a methodology to design a branch of a multiple aperture reflective telescope from a plane symmetric system.

4 Conclusions

We examine the phase behavior of an off-axis section of a rotationally symmetric system, and have used it to define ideal behavior for a branch of a multiple aperture system. According to this theory, an optical system that follows such ideal phase behavior can be phased perfectly. The phase behavior of a plane symmetric system that represents a branch of a multiple aperture system has also been found. We have recognized the nature of the phase terms that can exist in a multiple aperture system to the second and fourth orders of approximation in the field and aperture.

To second order, there are six phase terms: uniform piston, tilt, focus, magnification, linear piston, and quadratic piston. To fourth order there are 15 phase terms and only six are allowed: quadratic distortion 1, quadratic piston, cubic piston, field curvature, distortion, and quartic piston.

The phase coefficients in the ideal systems depend on one another due to the inherent rotational symmetry. The phase coefficients in the plane symmetric system can be independent of each other. Design rules have resulted from requiring the plane symmetric system to have the phase behavior of the ideal system.

The second order design rules establish optical path equality along the chief ray (18), conditions in the location and size of the image [(19) through (21)], Meinel's condition (22), and the effects of postional errors in the pupils (22) and (23).

To fourth order, the presence of field defocus, distortion, and quartic piston in the ideal system requires similar phase terms (36) to (38), quadratic piston (40), cubic piston (34), and quadratic distortion 1 (35) to be present in the plane symmetric system. This may signify more complexity in the design of a plane symmetric branch to be used in a multiple aperture system.

We have established that for an axially symmetric branch to be phased properly to fourth order, it must satisfy the sine condition of the pupils and have a flat sagittal field at the exit pupil. Although the design rules presented require a branch system to have a specific phase behavior, in practice some departure from those rules can be tolerated. This departure will depend on the coherence length of the source and on the image quality required.

By following a wave approach, we have constructed a phase theory for multiple aperture systems. The treatment presented is cohesive and phasing effects described elsewhere evolve in a natural way. By revealing the phase terms that can exist and their implications, the theory provides insight into practical design work. In addition, the phase theory presented makes connections with pupil theory in rotationally symmetric systems and with the theory of plane symmetric systems. In this way the phase theory for multiple aperture systems is a new addition to wave aberration theory.

Acknowledgments

This work was supported in part by Naval Research Labs as part of the Revolutionary Imaging Technologies Program. This work was also performed in part under contract with the Jet Propulsion Laboratory (JPL) through the Michelson Fellowship Program, funded by NASA as an element of the Space Interferometry Mission. JPL is managed for NASA by the California Institute of Technology.

We would like to thank Roland Shack for the information and insights that he shared with us.

References

1. V. N. Mahajan, "Strehl ratio for primary aberrations: some analytical results for circular and annular pupils," *J. Opt. Soc. Am. A* **72**(9), 1258–1266 (1982).
2. V. N. Mahajan, "Strehl ratio for primary aberrations in terms of their aberration variance," *J. Opt. Soc. Am. A* **73**, 860–861 (1982).
3. J. E. Harvey and R. A. Rockwell, "Performance characteristics of phased array and thinned-aperture optical telescopes," *Opt. Eng.* **27**(9), 762–768 (1988).
4. R. R. Butts, S. J. Cusumano, J. S. Fender, and C. R. DeHainaut, "Phasing concept for an array of mutually coherent laser transmitters," *Opt. Eng.* **26**(6), 553–558 (1987).
5. R. R. Butts, "Effects of piston and tilt errors on the performance of multiple mirror telescopes," *Proc. SPIE* **293**, 85–89 (1981).
6. R. V. Shack, J. D. Rancourt, and H. Morrow, "Effects of dilution on a six-element synthetic aperture," *Appl. Opt.* **10**(2), 257–259 (1971).
7. J. S. Fender, "Synthetic apertures: an overview," *Proc. SPIE* **440**, 2–7 (1981).
8. J. E. Harvey, A. B. Wissinger, and A. N. Bunner, "A parametric study of various synthetic aperture telescope configurations for coherent imaging applications," *Proc. SPIE* **643**, 194–207 (1986).
9. J. E. Harvey, M. J. MacFarlane, and J. L. Forgham, "Design and performance of ranging telescopes: monolithic vs. synthetic aperture," *Proc. SPIE* **440**, 56–67 (1983).
10. G. E. Palma and S. S. Townsend, "Performance and phasing of multiline synthetic apertures" *Proc. SPIE* **440**, 68–76 (1983).
11. W. A. Traub, "Combining beams from separated telescopes," *Appl. Opt.* **25**(4), 528–532 (1986).
12. R. V. Shack, "Aberration limitations on optical array telescopes," *J. Opt. Soc. Am. A* **68**, 1361 (1978).
13. A. B. Meinel, "Aperture synthesis using independent telescopes," *Appl. Opt.* **9**(11), 2501–2504 (1970).
14. J. E. Harvey and C. Ftaclas, "Field of view limitations of phased telescope arrays," *Appl. Opt.* **34**(25), 5787–5798 (1995).
15. J. E. Harvey and C. Ftaclas, "Fundamental limitations on off-axis performance of phased telescope arrays," *Proc. SPIE* **1236**, 390–405 (1990).
16. J. M. Beckers, "Field of view considerations for telescope arrays," *Proc. SPIE* **628**, 255–289 (1986).
17. L. D. Weaver, J. S. Fender, and C. R. DeHainaut, "Design considerations for multiple telescope imaging arrays," *Opt. Eng.* **27**(9), 730–735 (1988).
18. C. M. Lampkin, G. W. Flint, and M. J. MacFarlane, "Optical and mechanical design aspects of a four-telescope array for combined imaging," *Opt. Eng.* **27**(9), 749–754 (1988).
19. J. M. Beckers, "The VLT interferometer: Factors affecting wide field-of-view operation," *Proc. SPIE* **1236**, 379–389 (1990).
20. R. L. Lucke, "Influence of Seidel distortion on combining beams from a phased telescope array," *Appl. Opt.* **38**(22), 4776–4783 (1999).

21. T. W. Stuhlinger, "All-reflective phased-array imaging telescopes," *Proc. SPIE* **1354**, 438–446 (1990).
22. K. Shu and S. Eisenberg, "Planning the national new technology telescope optical designs," *Proc. SPIE* **628**, 66–79 (1986).
23. J. S. Fender, "Phased-array optical systems," *Proc. SPIE* **643**, 122–128 (1986).
24. P. W. Scott, "Some design considerations for a synthetic aperture optical telescope array," *Proc. SPIE* **445**, 126–129 (1983).
25. J. M. Geary, D. Duneman, J. Londono, and C. E. Moeller, "Experimental investigation of polarization effects in Young systems," *Opt. Eng.* **25**(12), 1284–1286 (1986).
26. M. J. E. Golay, "Point arrays having compact, nonredundant autocorrelations," *J. Opt. Soc. Am.* **61**, 272–273 (1971).
27. B. D. O-Neil, C. R. De Hamaut, P. Menicucci, and C. Hines, "Four telescope phased-array optical simulation," *Proc. SPIE* **1236**, 406–423 (1990).
28. J. M. Sasian, "How to approach the design of a bilateral symmetric optical system," *Opt. Eng.* **33**(6), 2045–2060 (1994).
29. H. H. Hopkins, "The Sine condition and Herschel's condition," Chap 3 in *Wave Aberration Theory*, pp. 35–47, Oxford University Press, London (1950).
30. C. G. Wynne, "Primary aberrations and conjugate change," *Proc. Phys. Soc. London* **65b**, 429–437 (1952).
31. W. T. Welford, "Primary monochromatic aberrations," Appendix 3 in *Aberrations of Optical Systems*, p. 265, Adam Hilger, Bristol (1989).

Erin M. Sabatke is studying the design and modeling issues of multiple aperture systems for imaging. She is also interested in diffractive beam propagator and polarization issues in these systems, as well as astronomical instruments in general. She was awarded a Michelson Interferometry Graduate Fellowship from JPL and NASA in 1999. She completed her undergraduate degrees in physics and astrophysics at the University of Minnesota in Minneapolis in 1997. She is currently finishing the PhD program in the Optical Sciences Center at the University of Arizona.

José M. Sasián received his PhD and MS degrees from the University of Arizona in 1988 and 1987, respectively, and a BS degree from the University of Mexico. He has been involved in the design, fabrication and testing of optical instruments for astronomical research. He has participated in both the professional and amateur telescope making communities, designing innovative telescopes. He was a Member of the Technical Staff at AT&T Bell Laboratories from 1990 to 1995, where he developed optical and optomechanical systems for photonic switching systems. He is currently a professor at the University of Arizona's Optical Sciences Center. His professional interests include teaching, microlithography, optical instrumentation, telescope technology, optomechanics, lens design, illumination optics, and light propagation.

Errata:

Equation 32 should read: $P_{02002} = P_{11011} = P_{10010} = P_{03001} = P_{12101} = 0.$

Equation 46 should read:

$$P_{220} = \frac{1}{4}\Phi\,[\tan u' \tan \bar{u}' - \tan u \tan \bar{u}\,] - \frac{1}{4}\Phi^2 \Sigma\,(1/n'-1/n)/r + \frac{1}{4}P_{222}\ .$$

REFERENCES

[1] E. Wilson and R. Mah, "Online fringe tracking and prediction at iota," in *18th Congress of the International Commission for Optics*, 1999, vol. 3749 of *Proceedings of SPIE*, pp. 691–692.

[2] P. Salinari, "The large binocular telescope," in *18th Congress of the International Commission for Optics*, 1999, vol. 3749 of *Proceedings of SPIE*, pp. 60–71.

[3] E. Hege, J. Christou, S. Jefferies, and M. Cheselka, "Technique for combining incoherent interferometric images," *Journal of the Optical Society of America A*, vol. 16, no. 7, pp. 1745–1750, 1999.

[4] Max Born and Emil Wolf, *Principles of Optics*, Cambridge University Press, 6 edition, 1980.

[5] Daniel J. Schroeder, *Astronomical Optics*, Academic Press, 1987, Pages 224-230.

[6] J. E. Harvey and R. A. Rockwell, "Performance characteristics of phased array and thinned-aperture optical telescopes," *Optical Engineering*, vol. 27, no. 9, pp. 762–768, 1988.

[7] R. V. Shack, J. D. Rancout, and H. Morrow, "Effects of dilution on a six-element synthetic aperture," *Applied Optics*, vol. 10, no. 2, pp. 257–259, 1971.

[8] M. J. E. Golay, "Point arrays having compact, nonredundant autocorrelations," *Journal of the Optical Society of America*, vol. 62, pp. 272–273, 1971.

[9] T. J. Cornwell, "A novel principle for optimization of the instantaneous fourier plane coverage of correlation arrays," *IEEE Transactions on Antennas and Propagation*, vol. 36, no. 8, pp. 1165–1167, 1988.

[10] V. N. Mahajan, "Strehl ratio for primary aberrations: some analytical results for circular and annular pupils," *Journal of the Optical Society of America*, vol. 72, no. 9, pp. 1258–1266, 1982.

[11] V. N. Mahajan, "Strehl ratio for primary aberrations in terms of their aberration variance," *Journal of the Optical Society of America*, vol. 73, pp. 860–861, 1982.

[12] R. R. Butts, "Effects of piston and tilt errors on the performance of multiple mirror telescopes," in *Wavefront Distortions in Power Optics*, C. A. Klein, Ed., 1981, vol. 293 of *Proceedings of SPIE*, pp. 85–89.

[13] R. V. Shack, "Aberration limitations on optical array telescopes," *Journal of the Optical Society of America*, vol. 68, pp. 1361, 1978.

[14] J. M. Geary, D. Duneman, J. Londono, and C. E. Moeller, "Experimental investigation of polarization effects in young systems," *Optical Engineering*, vol. 25, no. 12, pp. 1284–1286, 1986.

[15] J. S. Fender, "Synthetic apertures: an overview," in *Synthetic Aperture Systems*, 1981, vol. 440 of *Proceedings of SPIE*, pp. 2–7.

[16] J. E. Harvey, A. B. Wissinger, and A. N. Bunner, "A parametric study of various synthetic aperture telescope configurations for coherent imaging applications," in *Infrared, Adaptive, and Synthetic Aperture Optical Systems*, R. B. Johnson, Ed., 1986, vol. 643 of *Proceedings of SPIE*, pp. 194–207.

[17] J. E. Harvey and C. Ftaclas, "Field of view limitations of phased telescope arrays," *Applied Optics*, vol. 34, no. 25, pp. 5787–5798, 1995.

[18] L. D. Weaver, J. S. Fender, and C. R. DeHainaut, "Design considerations for multiple telescope imaging arrays," *Optical Engineering*, vol. 27, no. 9, pp. 730–735, 1988.

[19] J. S. Fender, "Phased array optical systems," in *Infrared, Adaptive, and Synthetic Aperture Optical Systems*, R. B. Johnson, Ed., 1986, vol. 643 of *Proceedings of SPIE*, pp. 122–128.

[20] N. V. Ryabova and D. N. Eskov, "Multiaperture synthesis telescope systems with direct image formation," *Soviet journal of optical technology*, vol. 60, no. 8, pp. 507–521, 1993.

[21] A. B. Meinel, "Aperture synthesis using independent telescopes," *Applied Optics*, vol. 9, no. 11, pp. 2501–2504, 1970.

[22] W. A. Traub, "Combining beams from separated telescopes," *Applied Optics*, vol. 25, no. 4, pp. 528–532, 1986.

[23] R. L. Lucke, "Influence of seidel distortion on combining beams from a phased telescope array," *Applied Optics*, vol. 38, no. 22, pp. 4776–4783, 1999.

[24] R. D. Sigler and A. L. Palmer, "Increasing the phased field of view of large distributed aperture telescope arrays," in *Current Developments in Lens Design and Optical Engineering II*, 2001, vol. 4441 of *Proceedings of SPIE*, pp. 60–71.

[25] E. Hege, J. Beckers, P. Strittmatter, and D. McCarthy, "Multiple mirror telescope as a phased array telescope," *Applied Optics*, vol. 24, no. 16, pp. 2565–2576, 1985.

[26] T. M. Herbst and H. W. Rix, "Star formation and extrasolar planet studies with near-infrared interferometry on the lbt," *Astronomical Society of the Pacific Conference Series*, vol. 188, pp. 341–350, 1999.

[27] Joseph W. Goodman, "Frequency analysis of optical imaging systems," in *Introduction to Fourier Optics*, chapter 6. McGraw-Hill, 1998.

[28] Jack Gaskill, *Linear Systems, Fourier Transforms, and Optics*, John Wiley and Sons, 1978.

[29] Max Born and Emil Wolf, "Interference and diffraction with partially coherent light," in *Principles of Optics*, chapter 10. Cambridge University Press, 6 edition, 1980.

[30] Arvind S. Marathay, *Elements of Optical Coherence Theory*, John Wiley and Sons, 1982.

[31] J. M. Sasian, "How to approach the design of a bilateral symmetric optical system," *Optical Engineering*, vol. 33, no. 6, pp. 2045–2060, 1994.

[32] Rudolf Kingslake, *Lens Design Fundamentals*, Academic Press, 1978, Pages 158-166.

[33] J. C. Wyant and K. Creath, "Basic wavefront aberration theory for optical metrology," in *Applied OPtics and Optical Engineering*, R. R. Shannon and J. C. Wyant, Eds., vol. 11, chapter 1, pp. 9–12. Academic Press, 1992.

[34] H. M. Merklinger, "Scheimpflug's patent," *Photo Techniques*, Nov/Dec 1996.

[35] Rudolf Kingslake, *Lens Design Fundamentals*, Academic Press, 1978, Pages 185-188.

[36] W. T. Welford, *Aberrations of Optical Systems*, Adam Hilger, 1 edition, 1997.

[37] D. Korsch, *Reflective Optics*, Academic Press, 1 edition, 1991.

[38] D. McCarthy, E. Sabatke, P. Hinz, R. Sarlot, and J. H. Burge, "Cryogenic beam combiner for very low background, 2-20 um interferometry on the 22.8 m large binocular telescope," in *Interferometry in Optical Astronomy*, P. J. Lena and A. Quirrenbach, Eds., 2000, vol. 4006 of *Proceedings of SPIE*, pp. 659–672.

[39] J. M. Hill, "Requirements for the lbt combined focus," Tech. Rep. UA-93-07, Steward Observatory, University of Arizona, 1993.

[40] B. Stamper, R. Angel, J. Burge, T. Connors, B. Duffy, and N. Woolf, "Stretched membrane with electrostatic curvature (smec) mirrors for extremely large space telescopes," in *Opticsl Manufacturing and Testing IV*, 2001, vol. 4451 of *Proceedings of SPIE*, pp. 105–113.

[41] R. N. Wilson, *Reflecting Telescope Optics I, Basic Design Theory and its Historical Development*, Springer-Verlag, 1996.

[42] C. Zhao and J. H. Burge, "Conditions for correction of linear and quadratic field-dependent aberrations in plane-symmetric optical systems," *Journal of the Optical Society of America A*, vol. 19, no. 12, pp. 2467–2472, 2002.